RICE UNIVERSITY

Microwave Transitions and Synthetic Dimensions in Rydberg Atoms

by

Yi Lu

A Thesis Submitted
in Partial Fulfillment of the
Requirements for the Degree

Doctor of Philosophy

Approved, Thesis Committee:

Thomas Killian, Chair
Dean of the Wiess School of Natural Sciences
Professor, Physics and Astronomy

Randall Hulet
Fayez Sarofim Professor, Physics and Astronomy

Hanyu Zhu
Assistant Professor, Materials Science and NanoEngineering
William Marsh Rice Chair

Houston, Texas

February, 2025

ABSTRACT

Microwave Transitions and Synthetic Dimensions in Rydberg Atoms

by

Yi Lu

The marriage between Rydberg physics and ultracold atomic systems have hatched so many fascinating achievements. The exaggerated properties of Rydberg states, combined with the pristine environments provided by the ultracold atoms, can lead to realizations of exotic physical systems. One particularly innovative direction that emerged recently is to use microwave-frequency transitions between Rydberg levels to simulate the dynamics of a particle hopping between lattice sites. Such approach, referred to as Rydberg synthetic dimensions, falls under the broad scheme of quantum simulations. Here we present description of the infrastructure used for Rydberg excitation and coherent microwave transitions, which are essential to the realization of Rydberg synthetic dimensions. We will also present experimental results on simulating the Su-Schireffer-Heeger Hamiltonian, a canonical model with paradigmatic importance in topological physics.

Contents

Illustrations

Tables

Acknowledgements

It is incredible how time flies, as it feels just like yesterday that I accepted the PhD offer from Rice and contacted Prof. Thomas Killian about the opportunity of doing some informal summer research before the official enrollment. While I simply could not wait to start learning more about cold atoms, Tom, to my surprise, offered to pay me for the summer as an official graduate researcher. Thereby I left for Houston, still adapting to the luxury of getting paid doing something I am fascinated with and excited about. Fortunately, to this day, I still hold my deep enthusiasm for these little atoms, and I am ready to venture into my next journey with them. Tom, I hope you think those summer stipend you offered me has paid off for you, as I certainly feel that I have learned and gotten much more support from you that I have ever helped in realizing your scientific vision.

My gratefulness should be extended especially to Dr. Barry Dunning. I believe I can say this on behalf of everyone in the Killian group that your presence as a co-advisor figure has been absolutely invaluable for all of us, and your infectious passion on science and instrumentation has guided me on so many aspects from circuit soldering to paper editing. I feel incredibly lucky to have had amazing colleagues in the lab. My scientific exploration has been mostly a smooth drive as I travel on roads paved by Roger, Joe and Soumya, who have greatly inspired me with their work-spirit, enthusiasm and composure when it comes to physics. I am also thankful for having a wonderful co-driver, Chuanyu, who, for so long and so many times, provided crucial support without which I would not be able to accomplished lots of the exciting results. Of course, it has been encouraging seeing the success and achievements of other members of the lab: Josh, Grant, MacKenzie, Brent. I wish the best for the

next generation of Killian lab: Nina, Ang and Brandon and cannot wait to see the future of the lab in your able hands.

I would like to thank the wonderful group of faculties and staffs at the P&A Department. They cleared out most of the logistical difficulties, allowing me to focus on my coursework and research. Special thanks to Dr. Randy Hulet and Dr. Andrea Isella, along with Tom, for being on my PhD committee, watching me mature into, dare I say, a physicist as I am today. Of course, also for having mercy on my candidacy exam and thesis defense, with Dr. Matthew Foster and Dr. Hanyu Zhu.

Graduate life at Rice has treated me well with the heartwarming presence of my friends and family. Thanks to my parents for their unwavering support that has carried me through the journey of undergrad and now PhD. While I would not try to name every friends met on tennis courts, in rec center and on hotpot stove, I would like to thank particularly Kexin, who, with her love and support, has made me able to enjoy many more aspects of life and helped me get through the physically and mentally draining last few months of my PhD.

Chapter 1

Introduction

This document presents our efforts and results on driving and characterizing microwave transitions between Rydberg states in strontium atoms and using these transitions to construct synthetic dimension experiments. I will begin by introducing the basic properties of strontium Rydberg atoms and motivating it as a platform to realize synthetic dimensions. The second chapter covers our experimental apparatus, which was adapted to drive microwave Rydberg transitions in ultracold strontium atoms. A particular focus will be placed on the generation of the microwave tones and the narrow-linewidth Rydberg excitation laser sources. The third chapter discusses different spectroscopic methods we use to characterize the microwave Rydberg transitions, which form the basis for the synthetic-dimension experiments presented afterwards. The experimental results revolve around two publications that observed the topologically protected edge state in the Su-Schrieffer-Heeger model and probed its topological phase transition. The thesis will finish on a teaser of some possible future work with strontium synthetic dimensions, particularly when combined with a under-construction optical tweezer array apparatus.

1.1 Rydberg atoms

A Rydberg atom is an atom that has one (or more) electron(s) in a highly excited orbital characterized by the principal quantum number n. It is named after the Swedish

physicist Johannes Rydberg who formulated [10] a generalization of the Balmer series, which empirically describes the spectral line emission from the hydrogen atom. The Rydberg formula inspired speculations about the internal structure of the atoms and eventually led to the Bohr model which states that the energy of orbital levels, as characterized by the quantum number n, within a hydrogenic atom is given by

$$E_n = -\frac{Z^2 R_H}{n^2} \tag{1.1}$$

where Z is the number of protons, and the Rydberg constant $R_H \approx 13.6$ eV is corrected by the reduced mass of the electron and nucleus. Note that the energy expression is negative as it is referenced to unbound electron and nucleus.

The applicability of the Rydberg formula is not limited to hydrogenic atoms. For multi-electron atoms, the effect of Coulomb screening caused by inner shells as experienced by the valence electron can be complex to analyze in simple universal fashion. Physicists have adopted a quantitative correction method known as quantum defect [11], which are sets of empirical numbers used to correct the values of n in each element. The effective quantum number is given by

$$n^* = n - \delta_l \tag{1.2}$$

where the quantum defect δ_l is also l-dependent since orbitals with different angular momenta have different probability density near the core. Therefore, δ_l is expected to be the largest for s-orbitals while diminishing for high-l states.

The quantum defect treatment is the most effective in hydrogen-like species such as the alkali metal and alkaline earth atoms, and their properties are well parameterized by the effective quantum number n^* with a set of scaling behaviors [11] as shown in Table 1.1. At high n, these scaling behaviors lead to exaggerated properties that have made Rydberg states extremely powerful for modern atomic physics experiments.

Most noticeably, the $(n^*)^7$ scaling of the polarizability leads to long-range dipole-

Property	n^* Scaling	Sr $(5s38s)^3S_1$
Binding Energy	$(n^*)^{-2}$	1200 cm^{-1}
Radius	$(n^*)^2$	60 nm
Energy Spacing	$(n^*)^{-3}$	154 GHz
Lifetime	$(n^*)^3$	21 μs
Ionization Field	$(n^*)^{-4}$	225 V cm^{-1}
Polarizability	$(n^*)^7$	7 MHz cm^2 V^{-2}

Table 1.1 : Scaling laws of Rydberg atom properties and corresponding typical values of the $(5s38s)^3S_1$ state in strontium.

dipole interactions between Rydberg atoms. Its tunability via changing quantum number n has allowed engineering of the interaction Hamiltonian to simulate many-body systems such as the quantum Ising model [12, 13, 14]. The interaction also gives rise to the Rydberg blockcade effect [15] where the presence of one Rydberg atom shifts the energy of the state such that a second excitation is precluded in its vicinity. The Rydberg blockade has been used to generate entanglement between neutral atom qubits and realize quantum gate operations [16], which constitute promising building blocks for quantum information processing [17, 18]. Besides these, Rydberg states offer much more versatility with other notable applications including spin squeezing with Rydberg dressing [19, 20], quantum sensing of small fields [21, 22] and probing of non-local spatial correlations with Rydberg molecules [23, 24].

1.1.1 Rydberg series in Strontium

Strontium (Sr) is one of the alkaline earth metal elements located in Group II on the periodic table. As any other alkaline earth metal, strontium has a completely filled inner shell and two valence electrons. The divalent structure gives rise to two separate series of atomic levels corresponding to the electron spins being in the aligned (triplet) or anti-aligned (singlet) configurations. Because of the vanishing overlap on the electron-spin part of the wave function, matrix elements between singlet and triplet states are generally small, leading to naturally weak transitions between them. These spin-forbidden inter-combination lines are the defining feature of alkaline earth metals in cold atom experiment. They enable laser cooling with lower Doppler limited temperatures [25, 26] compared to typical alkali atoms. In strontium particularly, the $(5s^2)\,{}^1S_0 - (5s5p)\,{}^3P_1$ principal transition can be used to laser cool atoms down to as low as 1μK thanks to its natural linewidth of 7.5kHz. The narrow linewidth also make them ideal candidates for making optical atomic clocks, such as the record-holding one at JILA with $\lesssim 10^{-18}$ fractional uncertainty operating on the doubly forbidden $(5s^2)\,{}^1S_0 - (5s5p)\,{}^3P_0$ transition with ~ 1 mHz linewidth [27].

The singlet and triplet series also continue into the Rydberg levels ($n \gtrsim 20$). In the work presented in this thesis, we are mostly concerned with states where only one of the electrons is excited to a low-angular-momentum ($l \leq 3$) Rydberg orbital, i.e. $5snl$ with $l = s, p, d, f$. However, doubly excited Rydberg states are also of rich physics and experimental possibilities. For alkaline earth metal particularly, the ionic core still has one valence electron, allowing excitation in the visible range. In the case of low-l Rydberg states, excitation of the second valence electron can lead to collisions where one of the electrons acquires enough energy to get into the continuum, thereby ionizing the atom. This process is called auto-ionization, and it can be used

as an alternative way of detection Rydberg population [11, 28]. Recently, circular Rydberg states with maximum angular momentum (i.e. $|m| = n - 1$) have been drawing attention for their long natural lifetime due to the lack of decay channels [29]. Combined with coherent manipulation with resonant microwave transitions, this makes them good candidates for constructing qubits for quantum computing application with long coherence time and high gate fidelity. The divalent structure of alkaline earth atoms bring added potential in that the optically active core enables further manipulations such as dipole trapping and cooling of the circular Rydberg atoms [30, 31].

Rydberg states	δ_0	δ_2	δ_4
$^1S_0$	3.2688559	-0.0879	-3.36
$^1P_1$	2.7314851	-5.1501	-140.1
$^1D_2$	2.3821857	-40.5009	-878.6
$^1F_3$	0.0873868	-1.5446	7.56
$^3S_1$	3.371	0.5	-10
$^3P_0$	2.8866	0.44	-1.9
$^3P_1$	2.8824	0.407	-1.3
$^3P_2$	2.8719	0.446	-1.9

Table 1.2 : First-order term of the quantum defect values of selected Rydberg series in strontium. Data for singlet and triplet states are from Ref.[7] and Ref.[8] respectively.

As introduced earlier, the energy of Rydberg states can be calculated from the quantum defect δ_l. The values of δ_l for the states involved in our experiments, as obtained from previous studies [8, 9], are listed in Table 1.2, and they are used to predict the laser (or microwave) frequencies for transitions to (or between) Rydberg

levels. As will be discussed in Chapter 3, our microwave spectroscopy results gave more accurate updates to some of the singlet Rydberg states [7].

1.2 Synthetic dimensions

A synthetic dimension is a collection of quantum states that can be engineered so that the Hamiltonian of a system can be engineered, usually with applied external fields, such that it mimics the Hamiltonian of a particle moving in a real-space dimension. This definition also provides the recipe for creating a synthetic dimension: selecting a set of states as the coordinates and defining the rules that dictate the transitions between those coordinate states [32].

The innate flexibility in the process of constructing the synthetic dimensions (i.e. how one chooses to define the coordinates and transitions) grants it potential to engineer the equation of motion almost arbitrarily. This aligns closely with the long-standing idea of quantum simulation, which, put forward originally by Feynman [33], is where the concept of synthetic dimension has stemmed from. The computation power needed to simulate any quantum systems grows exponentially with system size, and it quickly gets into a regime beyond reach with classical computing for any non-trivial number of particles. While a general-purpose quantum computer still appears far from achieving an impactful scalability [34], the idea naturally emerges to engineer an experimental mock-up that is tailor made to mimic the Hamiltonian of particular physical systems of interest[35].

Similar to quantum computing, quantum simulation demands excellent coherence properties of the experimental system. As a result, realizations of analog quantum simulators have been mainly contributed by low-temperature platforms, such as superconducting circuits [36, 37, 38], ultracold atoms and molecules [39, 40, 41], trapped

ions [42, 43] and photonic systems [44]. Among them, ultracold atoms, thanks to the advancement in laser cooling as well as more advanced trapping and manipulation techniques such as optical lattices [45], have seen numerous successes in realizing paradigmatic condensed-matter systems including the Bose- and Fermi-Hubbard models [46, 47, 48, 49, 50, 51, 52] and spin models [53, 14, 54]. Combined with Feshbach resonances for interaction tuning [55], quantum gas microscopes [56] and optical tweezer arrays [57] for individual-atom imaging and addressing and other techniques, prominent phenomena have been demonstrated in these systems, including the superfluid to Mott insulator transition [58] and BEC-BCS crossover [59, 60].

Most of aforementioned analog quantum simulation results use platforms where the experimental systems share conceptual similarities with the physical model being simulated. For example, the magnetic hyperfine sublevels of an atom in optical lattice sites may be used to simulate the spin of an electron under anti-ferromagnetic ordering. The synthetic dimension however, as a distinctive approach to quantum simulation, essentially maps any set of internal (or external) states in the experimental system directly to a set of sites in a real spatial system. While being less intuitive, this approach offers unique flexibility with which suitable internal (or external) degrees of freedom may be chosen to map particular spatial geometries difficult to realize using conventional approaches (i.e. direct spatial assembling). Such physical systems include higher-dimensional systems [61, 62], lattice models with non-trivial geometries (e.g. Kagome lattice) [63, 64] and artificial gauge fields [65, 66]. Many of these systems have been or been proposed to be realized with synthetic dimension platforms, a large part of which has centered on topological systems.

The mathematical discipline of topology, loosely stated, inspects the independence of certain properties of objects from continuous deformations of their geometric shape.

While being a long-standing branch of mathematics with fascinating manifestation such as the famous Möbius strip, topology did not have a significant impact on physics until it was being used to gain insight for the integer quantum Hall effect [67, 68]. The quantized electronic conductance, as it turned out, is protected by the topological order present in the 2D electron gas, [69], much like how the hole in the middle of a donut persists so long as the torus topology of the donut is preserved. Since then, the scope of topological physics has expanded to include a wider range of materials with distinct symmetries [70, 71, 72]. These systems are often dubbed topological insulators, referring to the typical situation where they may have insulating band structure in the bulk part while possessing topologically protected boundary states that conduct current [73, 74].

Quantum simulations of topological insulators have seen promising progress with synthetic dimension platforms in recent years. For example, atomic spin states and quantized motional states in a 1D optical lattice have been coupled to form a 2D grid with controllable artificial flux, leading to experimental visualization of the quantum Hall edge modes [75, 76]. Microwave coupled rotational levels within polar molecules, when they are individually trapped in 1D (2D) optical tweezer arrays, have the potential to realize novel phases such as quantum strings (membranes) [77, 78]. Momentum states of an optical lattice have also seen success in mapping the paradigmatic 1D Su-Schrieffer-Heeger (SSH) model and its variants, the SSH4 model [79, 80, 81]. The topologically protected edge states [79] as well as disorder-induced Anderson localization [80] were observed, including the ability to measure the chiral winding number [81]. The main work of this thesis also focuses on the realization and characterizations of the SSH model.

It is also worth noting that the concept of topological insulators is recently find-

ing novel applications in other fields. The robust protection against perturbations that respects symmetries associated with edge states makes them suitable candidates for quantum information processing, which is benefited by the enhanced coherence properties as a result of the topological protection [82, 83, 84]. Fabrications of photonic nano-cavities, which allow precise engineering of photonic lattice systems, have brought topological order to quantum optics and led to creation of topological light sources such as robust single-mode lasers and frequency combs [85, 86, 87].

1.2.1 Synthetic dimensions with Rydberg states

Rydberg atoms have been a significant contributor in ultracold-atom based quantum simulation, primarily because of the dipole-dipole interactions between Rydberg atoms. This interaction allows arrays of Rydberg atoms to mimic the behaviors of interacting spin$-\frac{1}{2}$ particles, leading to successes in studying quantum magnetic ordering [13, 14]. For synthetic-dimension-type experiments, the motivation of using Rydberg atoms arises from the n^{-3} scaling of the energy spacing between adjacent levels. A result of this scaling is that, in proper range of principal quantum number ($n \approx 40 - 70$), transition frequencies between adjacent levels lie conveniently in the microwave part of the spectrum ($\sim 10 - 100$ GHz). Leveraging the well established microwave technologies that are commercially readily available, large numbers of Rydberg levels within a single atom may be resonantly coupled by microwave sources whose amplitudes, frequencies and phases can all be coherently controlled. This synthetic lattice of Rydberg levels can be mapped to real-space lattice-type models with careful engineering of the microwave parameters as illustrated in Figure 1.1. This scheme was proposed in [88] and first realized here at Rice [4] in an experiment observing the topological edge states in the Su-Schrieffer-Heeger model via steady state

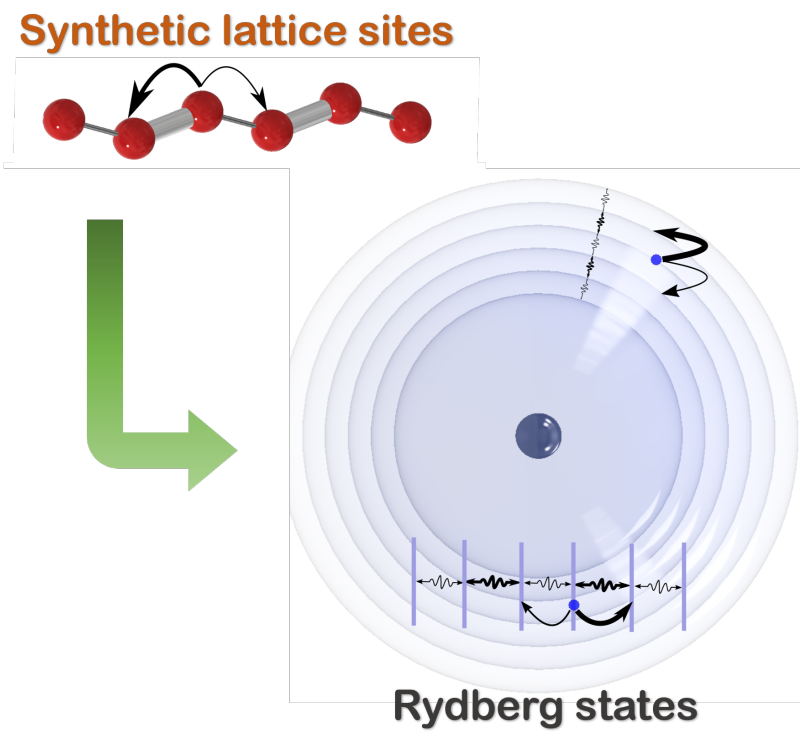

Figure 1.1 : Illustration of Rydberg levels coupled by microwave frequency transitions as synthetic lattice sites.

measurements. Subsequently, works from other groups have also demonstrated versatility of Rydberg synthetic dimensions, including realization of topological Thouless pumping in Rice-Mele model [89]. The main result presented in this thesis can be partially considered a continuation and improvement based on the original work in [4] in that we incorporated full state-resolving detection and measured population distribution in the synthetic space dynamically [5], which lead to quantitatively probing the topological-trivial phase transition in the SSH chain [90].

The more exciting aspect of Rydberg synthetic dimensions, however, becomes apparent when individual atoms with microwave coupled Rydberg levels are brought close together, e.g. in adjacent sites within optical tweezer arrays. The internal syn-

thetic space is combined with the aforementioned dipole-dipole interaction between Rydberg atoms to study exotic many-particle physics with the real-synthetic composite space. Such systems have seen promising results in the Gadway and Covey group, where potassium Rydberg atoms are prepared in closely spaced tweezer traps to observe correlated quantum walks and to realize artificial gauge fields using a phase-coherent loop geometry in the synthetic space [91, 92]. Effort at Rice relies on completing construction of a new optical tweezer apparatus and will include exploring collisional interactions in the synthetic space, studying thermalization processes and correlated many-body states such as quantum strings and membranes.

Chapter 2

Experimental Apparatus

Most of the exciting results from ultracold atomic physics highlighted in Chapter 1 would not have been possible without the invention of and advances in the laser cooling. Extremely low temperatures near absolute zero combined with tight spatial confinement brought about by various trapping techniques result in high phase-space density of the atomic assembles, leading to the emergence of their coherent quantum properties. Thanks to the simple hydrogen-like level structures, ultracold atomic systems have predominantly been experimentally realized with alkali-metal and alkaline-earth like species, among which strontium has been one of the star elements with which Bose-Einstein condensation [93, 94, 95] and degenerate Fermi gas [96, 97] have both been experimentally observed. Past research of Killian lab include pioneering work on achieving said quantum degeneracy and studying collisional behaviors of different isotopes via photo-association spectroscopy [98, 99].

The Rydberg apparatus at Killian lab was originally designed and constructed for the Rydberg molecule project, which revolves around probing non-local spatial correlations in quantum gases using photo-association spectroscopy of ultralong-range Rydberg molecules [23, 24, 100]. The microwave setup was incorporated into the apparatus at a later time for the newer synthetic dimension experiments, which constitute the theme of this thesis. Hence, there are aspects of the apparatus, especially in the vicinity around the science chamber, that are not ideally suited for good access and efficient propagation of microwave radiations. More detailed consequence of this

will be discussed in this chapter along with an outlook of an improved apparatus under construction teased in Chapter 5.

In this chapter, an overview of the Rydberg apparatus will be given with a description of our strontium laser cooling and trapping procedures and the Rydberg state detection system. A focus of this chapter will be put on the generation and frequency stabilization of the Rydberg excitation lasers and the microwave setup, both of which are critical for the synthetic dimension experiments.

2.1 Laser Cooling and Trapping of Sr

For the creation of ultracold strontium atoms, we follow standard protocols, which have been discussed in great detail in previous works [2, 9]. Here we will briefly describe the laser cooling and trapping process leading up to the final cold sample on which all our microwave measurements and synthetic dimension experiments are conducted on.

The initial stages of the sample preparation revolves around the principal transition $(5s^2)^1S_0 - (5s5p)^1P_1$ (at 461nm) which has a large natural linewidth of 30.5MHz, resulting in strong scattering forces. This is employed to first form a two-dimensional transverse optical molasses to collimate a hot beam of strontium emitted from a solid sample heated around 400°C. The atomic beam then passes through a Zeeman slower tube during which they are decelerated longitudinally by a counter-propagating red-detuned 461nm beam such that their final velocity gets low enough to be captured by the broad-band blue magneto-optical trap (MOT) operating on the same transition. During the cooling cycle, there exists an alternative decay path via $(5s4d)^1D_2$ state as shown in Figure 2.1. The $(5s4d)^1D_2$ can partially (with branching ratio of $1 : 2 \times 10^4$) decay into the $(5s5p)^3P_2$ metastable state, which is magnetically trapped

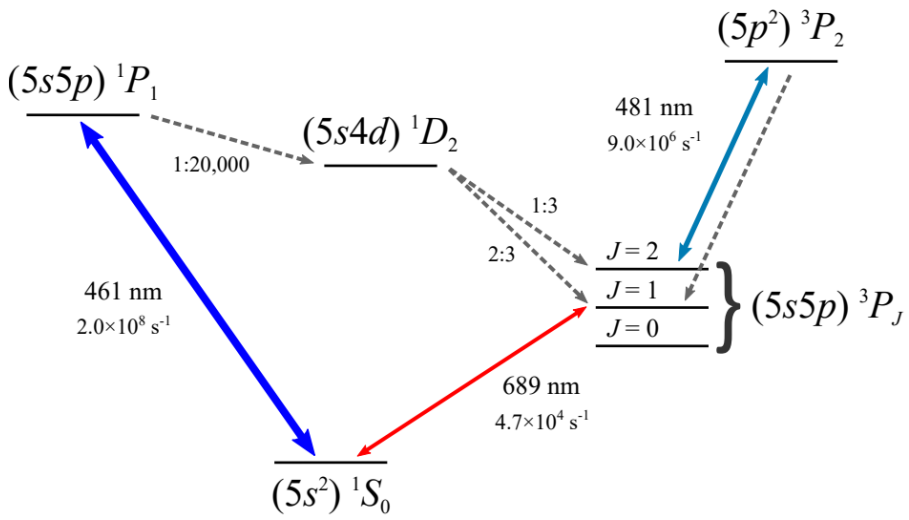

Figure 2.1 : Atomic levels involved in the laser cooling and trapping stages before loading the optical dipole trap (ODT). Wavelength and natural lifetimes are shown for each transition. Here solid and dashed lines indicate driven and spontaneous decay respectively.

by the quadruple field generated by the MOT coils, thereby results in a leakage of population from the cooling cycle. Therefore, towards the end of the blue MOT, we shine a 481nm laser on the atoms to excite the metastable $(5s5p)^3P_2$ state to the $(5p^2)^3P_2$, which can then decay to the $(5s5p)^3P_1$, and subsequently back to the ground state. This 481nm laser is hence referred to as the "repumper".

The blue MOT typically cools the strontium atoms down to $\sim 1mK$, which is low enough for the next stage of laser cooling that takes place in a narrow-band red MOT operating on the $(5s^2)^1S_0 - (5s5p)^3P_1$ intercombination line at 689nm with a natural linewidth of $\sim$ 7.5kHz. Because of the small linewidth compared to the Doppler linewidth of the atoms immediately after the blue MOT, the 689nm laser is artificially broadened by a combination of frequency dithering and power broadening. The extent of this broadening is gradually decreased until it becomes single-frequency, at which point the atomic cloud is typical at a temperature of $\sim 1-3\mu$K. Detailed

techniques of the narrow line cooling is well established and discussed else where [101, 9].

	Isotope Shift (MHz)		
Isotope	$(5s^2)^1S_0 - (5s5p)^1P_1$	$(5s^2)^1S_0 - (5s5p)^3P_1$	Abundance
^{84}Sr	-270.8	-351.49	0.56%
^{86}Sr	-124.8	-163.81	9.86%
^{87}Sr	-46.5	-62.15	7%
^{88}Sr	0	0	82.6%

Table 2.1 : Isotope shifts of the two laser cooling transitions. All the values are referenced to that of the most abundant isotope ^{88}Sr. Natural abundance of the four stable isotopes are also shown.

In order to selectively prepare ultracold samples of different isotopes, frequencies of the 461nm and 689nm lasers need to be adjusted according to the isotope shifts of the two transitions as listed in Table 2.1. For the 461nm laser, it is frequency stabilized using an error signal generated from saturated absorption spectroscopy on the $(5s^2)^1S_0 - (5s5p)^1P_1$ transition in ^{88}Sr in a hot strontium vapor cell. A bias magnetic field is applied to Zeeman shift the magnetic sublevel inspected such that when the 461nm laser is locked to the transition resonance, laser frequency can be tuned by adjusting the bias field. Details on this setup can be found in Ref.[9]. The 689nm laser, however, has a master frequency stabilized to a fixed-length external reference cavity, at +82MHz above the resonance frequency of $(5s^2)^1S_0 - (5s5p)^3P_1$ in ^{88}Sr. This master light is used to injection-lock several slave laser diodes each of which is frequency shifted using acousto-optic modulators (AOM) to hit the resonances in each isotope. Details about the frequency stabilization with the external cavity and

positioning with respect to the atomic transition is discussed in later section.

For the only Fermionic isotope ^{87}Sr, which is not used in the work of this thesis, the red MOT cooling involves an additional "stir" beam to redistribute population among magnetic sublevels to avoid anti-trapping arising from the hyperfine structure of ^{87}Sr. Details of trapping ^{87}Sr can be found in Ref [9].

2.1.1 Optical dipole trap

Following the narrow line red MOT, the cold ($\sim 1-3\mu$K) atoms are transferred into the final stage of atomic sample preparation: an optical dipole trap (ODT) formed by tightly focused laser intensity. The ODT is a well established trapping technique based on AC Stark shift on a two-level atom caused by an off-resonant laser field. When the laser is red-detuned with respect to the primary transitions of the atom, the off-resonant scattering shifts the ground state towards lower energy by an amount proportional to the laser intensity. This results in an effective potential $U \propto -I(\mathbf{r})$, i.e. the atoms seek for low intensity region. One can therefore create and engineer a trapping potential by shaping the intensity profile of the laser beam.

In the current apparatus, the ODT is realized using 1064nm beams, which is far red-detuned from any transitions connecting the $(5s^2)^1S_0$ ground state. The beams are derived from a 50W fiber amplifier (YLR-50-1064-LP from IPG). The power is split into two fiber coupled paths each of which emits a highly elliptically shaped beam with the major axes along the horizontal plane, and they are hence referred to as sheet beams. The two sheet beams enter the science chamber both horizontally at a 90° angle. At their intersection, the intensity profiles are superposed and form a combined potential of a pancake shape, which roughly resembles the atom distribution at the end of the red MOT stage.

Previous measurements have shown that the two sheet beams have Gaussian waists of $w_h = 231\mu$m, $w_v = 26\mu$m and $w_h = 117\mu$m, $w_v = 38\mu$m respectively. The tight waists w_v along the z-direction result in a vertical confinement strong enough to hold the atoms against gravity. The power in each beams can be varied in the range of $0 - 4$W, meaning maximum harmonic trap frequencies of $(\omega_x, \omega_y, \omega_z) \approx (200\text{Hz}, 40\text{Hz}, 20\text{Hz})$. For most experiments presented in this thesis, the trap frequency is typically around $(200\text{Hz}, 40\text{Hz}, 20\text{Hz})$. For atom number of ~ 1 million and a temperature of 1μK, this corresponds to a peak atomic density of $\sim 5 \times 10^{10}\text{cm}^{-3}$. For principal quantum number $n \sim 50 - 70$, this is in the low-density regime, where loss of Rydberg atoms by collisions with background atoms are negligible [102].

When confined in the ODT, atoms undergo collisions which, at this ultracold temperature, can be described by low-energy scattering theory. The strength of their collisional interaction is well captured by the s-wave scattering length shown in Table 2.2 for each isotopes and their mixtures. Among them, ^{84}Sr have a moderate scattering length at $a_s \approx 123a_0$, which is low enough to suppress three-body recombination that leads to rapid atom loss, but also high enough that the cloud thermalizes quickly

Isotope	^{84}Sr	^{86}Sr	^{87}Sr	^{88}Sr
^{84}Sr	123	21	-56	1800
^{86}Sr		811	164	98
^{87}Sr			97	44
^{88}Sr				-3

Table 2.2 : Low energy (s-wave) scattering length of between pairs of strontium isotopes in units of the Bohr radius a_0 [9].

for efficient forced evaporation process when even lower temperature (or quantum de-

generacy) is desired. These make ^{84}Sr the favorable isotope for our experiments on microwave transitions and Rydberg synthetic dimensions.

2.2 Selective field ionization

Detection of Rydberg atoms is vital to the experiments in this thesis. For that we apply ramped electric fields to ionize the Rydberg atoms in a state-selective sensitive way and detect the out-coming liberated electrons. This setup has been detailed in previous theses [6, 1], and here we will provide a brief description of the system.

The core components are the electrodes, centered at the position of the atomic cloud as shown in Figure 2.2, on which high voltages are applied to create the electric fields. Negative (V_-) and positive (V_+) voltages of typically up to 2.5kV can be applied

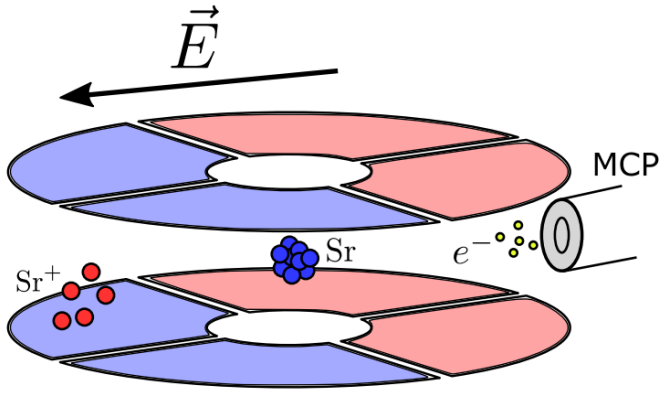

Figure 2.2 : A diagram depicting the positioning of the field ionization electrode plates. In typical Rydberg detection process, negative and positive voltages are applied to the blue and red sets of plates to create the electric field ionizing the Rydberg atoms and guiding the liberated electrons to the micro-channel plate (MCP) detector. The Sr^+ ions are also created in the process but is repelled by the electric field away from the MCP and are therefore not detected. Figure from Ref.[1]

to the blue (back) and red (front) sets of electrode respectively in Figure 2.2 such that the atoms feel a strong electric field towards the back electrodes. These voltages are

sourced by two Glassman HV supplies and pulsed on using two Berkeley Nucleonics pulse generators (PVS series) when Rydberg detection is needed. High-power resistors ($\sim$10kΩ) are connected to the pulse generator outputs to make a low-pass filter when combined with the natural capacitance of the cables and the electrode plates. These result in electric field pulses with an exponential time constant τ that can be adjusted by changing the resistance. In the current setup, we have $\tau \approx 5\mu$s, which results in charging up to 98% of supplied voltage (or discharging to zero volt) within a pulse time of 20μs.

For Rydberg orbitals with low angular momentum ($l \leq 1$), the threshold field for adiabatic ionization is given by $E_{th} = 1/16(n-\delta)^4$ in atomic units. The n-dependence here leads to different Rydberg levels getting ionized at different electric field strength and hence at different time during the exponential field ramp. After the ionization, the liberated electrons are guided in the direction opposite to the E-field towards the micro-channel plate (MCP) whose front and back plates are set at +350V and $+2800V$ respectively for enhancing the detection efficiency. The MCP converts the impact of electrons into current pulses which are then amplified and counted by multi-channel scaler (MCS) at computer interface. The MCS has a time resolution of 100ns, imposing a fundamental limit on how fast the electric field may be ramped while maintain the state selective detection.

At low quantum numbers ($n \lesssim 60$), we generally run with the configuration of $|V_-| \approx |V_+|$ (with $|V_-|$ typically slightly higher) in order to have a larger electric field at the atomic position. This results in a strong enough electric field for us to have ionized and detected Rydberg levels as low as $5s28s$ with $|V_-|, |V_+| \approx 2.2$kV. At all these quantum numbers, the detection efficiency, # of counts per actual Rydberg atom, is generally around ~ 0.3. At higher quantum numbers ($n \gtrsim 60$), the negative

plates alone can supply the needed electric field for ionization, and we may apply small DC voltages on the positive plates to create trim fields which cancels the stray electric fields that can cause significant Stark shifts on Rydberg levels due to the exaggerated polarizability $\alpha \propto n^7$.

2.3 Rydberg excitation lasers

As mentioned in Section 1.1.1, both the singlet $(5sns)\,{}^1S_0$ and the triplet $(5sns)\,{}^3S_1$ series of Rydberg levels are involved in the experimental results in this thesis. Two-

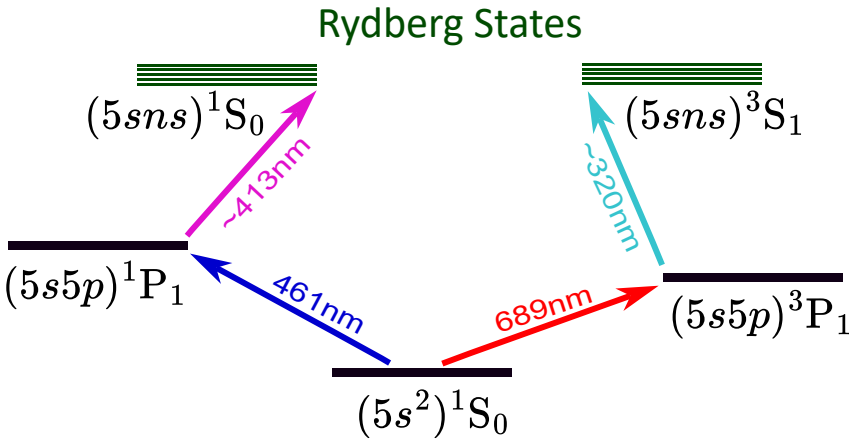

Figure 2.3 : Diagram showing the two-photon excitation paths from the $(5sns)\,{}^1S_0$ ground state to the singlet and triplet Rydberg series.

photon transition scheme illustrated in Figure 2.3 is used to excite strontium atoms to the Rydberg states, and the generation of these excitation photons is therefore a vital part of the experimental setup. This section describes both the singlet and the triplet Rydberg laser systems with a particular detailed focus on the tuning and stabilization of the frequencies of the triplet lasers.

Figure 2.4 shows the laser systems sourcing the two triplet photons. The original 689nm master light is generated from a Toptica DL pro tunable diode laser. It is then

fiber coupled onto the main optics table to injection lock three diode slaves, which provide all the 689nm light needed for the red MOT and the Rydberg excitation. The 320nm UV photon, however, has a more convoluted generation scheme. In

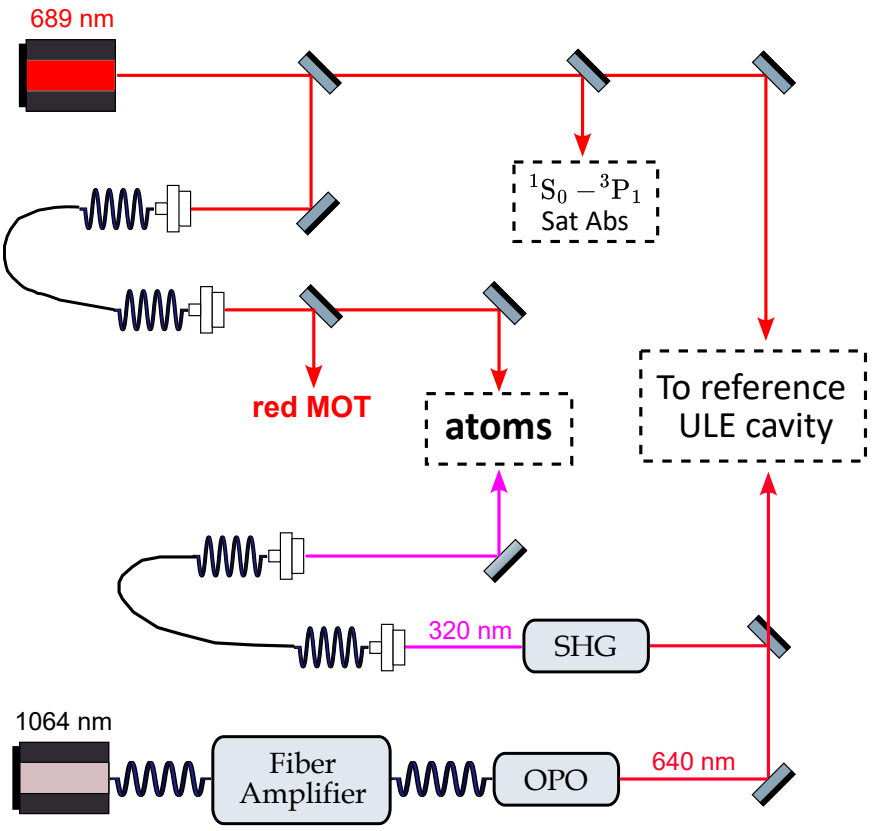

Figure 2.4 : Schematic diagram showing the system generating the two photons for triplet Rydberg excitation. OPO: optical parametric oscillator, SHG: second harmonic generation, Sat Abs: saturated absorption spectroscopy setup.

this case, the master light is generated by a tunable 1064nm fiber laser (Rock, NP Photonics), which gets amplified to 8.5W by an IPG fiber amplifier. This high-power 1064nm light pumps an Aculight Argos Model 2400 CW optical parametric oscillator (OPO), outputting roughly 1.4W of 640nm light, most of which is frequency doubled via second-harmonic-generation (SHG) in a Toptica SHG pro module. This process results in a final 320nm of UV power typically up to 100mW, which is solely used for

Rydberg excitation.

Both the 689nm (red) and 320nm, (UV) light are fiber coupled to be directed at the strontium atoms for Rydberg excitation. For the synthetic dimension related experiments, a beam of $\sim 2\,\mathrm{mm}$ in diameter with typical power of $100-200\,\mu\mathrm{W}$ of red power counter-propagates with a $\sim 500\,\mu\mathrm{m}$ UV beam of $\sim 1-10\mathrm{mW}$. The red and UV

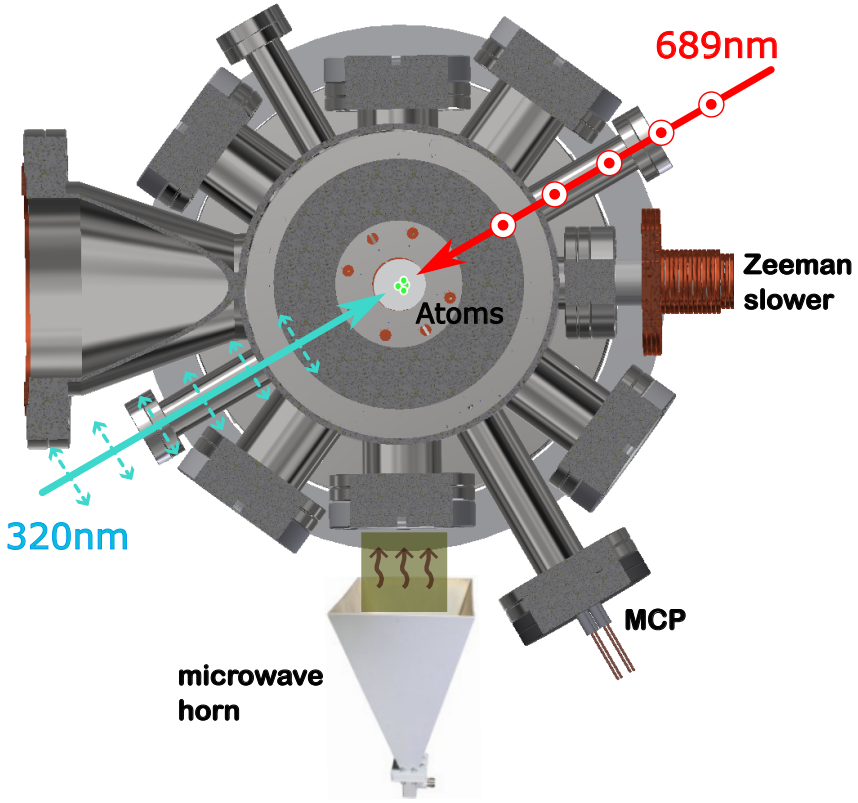

Figure 2.5 : Propagation and polarization configuration of the excitation lasers viewed from top. The 689nm and 320nm beams counter-propagate with a vertical and horizontal polarization respectively. The singlet (461nm+413nm) excitation beams (not drawn) share the same counter-propagating path but both with horizontal polarization.The position of the microwave horn is also shown.

beams are vertically and horizontally polarized respectively in reference to the optics table as shown in Figure 2.5. In the triplet case, this cross-linear configuration results in transitions to both the $m_J = \pm 1$ sub-levels of the $(5sns)\,^3S_1$ Rydberg states being

allowed. A DC bias magnetic field of up to ∼6 Gauss is usually applied perpendicular to the beam propagation direction to lift the m_J degeneracy so that we can selectively excite only the $m_J = +1$ sub-level for most of experiments in this thesis. The beam polarization shown in Figure 2.5 allows for the excitation path of $^1S_0$ $(m_J = 0) \rightarrow$ $^3P_1$ $(m_J = +1) \rightarrow$ $^3S_1$ $(m_J = +1)$.

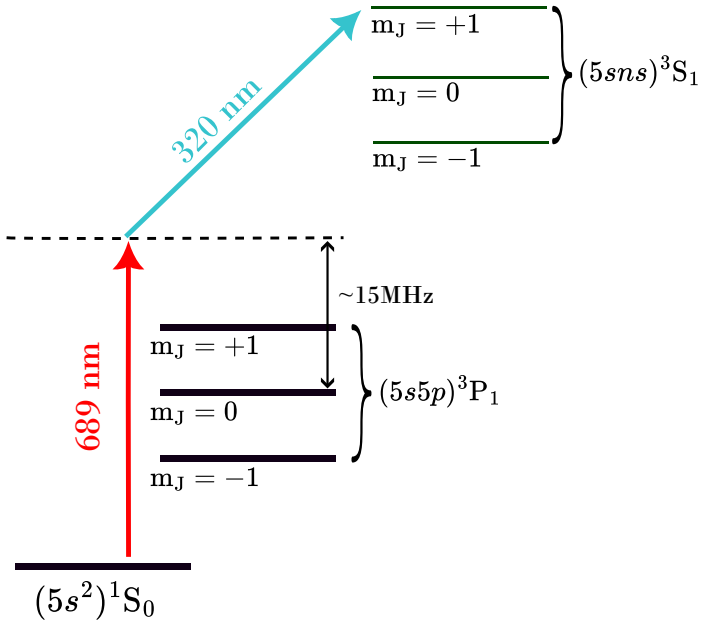

Figure 2.6 : Two-photon excitation path for the $(5sns)\,^3S_1$ triplet Rydberg states. The Zeeman shifts of the $m_J = \pm 1$ sublevels can be calculated from the known Landé g-factor to be about 2.1MHz/G and 2.8MHz/G for $(5sns)\,^3P_1$ and $(5sns)\,^3S_1$ respectively.

In the two-photon excitation path, the 689nm red photon is detuned by ∼15 MHz from the intermediate $(5s5p)\,^3P_1$ state with zero B-field as shown in Figure 2.6. For the $m_J = +1$ sublevel, this intermediate detuning becomes ∼ 3MHz at a B-field of ∼6 Gauss, which is still much greater than the natural linewidth (around 7.5 kHz) of the $(5s^2)\,^1S_0 - (5s5p)\,^3P_1$ transition such that off-resonant scattering is suppressed. The detuning is set to the blue side to avoid formation of molecular bound states on

the $(5s^2)\,^1S_0 + (5s5p)\,^3P_1$ potential [103, 104]. These numbers typically result in final two-photon Rydberg excitation Rabi frequency of $\lesssim 1\,\mathrm{Hz}$ ($\lesssim 1$ excitation over $1\,\mu$s out of 1 million atoms). A similar two-photon excitation scheme is used for the singlet Rydberg series using 461 nm and 413 nm lasers, where a much larger (~ 18 GHz) intermediate state detuning is chosen due to the strong $(5s^2)\,^1S_0 - (5s5p)\,^1P_1$ dipole matrix element [7, 100].

As introduced in Section 1.1, Rydberg states are relatively long-lived with radiative lifetime of $20-200\,\mu$s depending on the principle quantum number n. This translates to a natural linewidth of $5-50$ kHz on the Rydberg transition, which puts a demand on the laser linewidth for efficient excitation. This motivates high-performance frequency stabilization for the Rydberg excitation lasers. In addition, having a narrow laser linewidth also provides the resolution needed to spectrally access finer structures such as vibrational and rotational states of ultralong-range Rydberg molecules [24, 105] and, as will be discussed in Chapter 4, eigen-states of synthetic dimension systems when the tunneling rate is limited [90].

2.3.1 The PDH technique

Frequency stabilization of a laser typically involves an external reference such as an optical cavity mode or an atomic resonance. Generally speaking, a method is then required to extract an error signal which quantitatively assesses the real-time frequency difference between the laser and the selected frequency reference, and this error signal can then be fed back to the laser input to realize closed-loop control of its frequency. Based on this principle, such methods include side-of-fringe locking and frequency modulation spectroscopy [106], etc. We have adapted the Pound-Drever-Hall (PDH) method [107], which minimizes the influence of intensity noise of the light

and is widely used for high-bandwidth laser feedback.

The PDH method uses an external Fabry-Perot cavity as the frequency reference. While the full mathematical details of the PDH can be found in [108] and will not be covered in depth here, I will briefly describe the working principle of the technique. Analysis of the interference of multiple reflections inside a Fabry-Perot cavity with mirror reflectivity r (assumed same on both sides) yields a complex reflection coefficient for light at the input of the cavity of [109]

$$\mathcal{F} = \frac{E_{ref}}{E_{inc}} = \frac{r(e^{i\phi} - 1)}{1 - r^2 e^{i\phi}} \tag{2.1}$$

where $\phi = \omega/\Delta\nu_{cav}$ is the phase accumulated by the laser light over one round trip in the cavity, and ω and $\Delta\nu_{cav}$ are the optical frequency and the cavity free spectral range (FSR). When ω is near a cavity resonant mode ($\omega = 2\pi N \cdot \Delta\nu_{cav}$), the reflected light undergoes a frequency dependent phase shift, and the PDH technique essentially indirectly measures this phase shift. If the incident light is phase modulated at a fixed RF frequency Ω with modulation depth β, which generates sidebands at $\omega \pm \Omega$, the reflected light $E_{ref} = \mathcal{F}(\omega)E_{inc}$ contains the three components as shown in Equ. 2.2

$$\begin{aligned} E_{inc} &= E_0 \cdot e^{i\omega t + \beta \sin(\Omega t)} \\ &= E_0 \cdot [J_0(\beta)e^{i\omega t} + J_1(\beta)e^{i(\omega+\Omega)t} - J_1(\beta)e^{i(\omega-\Omega)t}] \end{aligned} \tag{2.2}$$

where J_0 and J_1 are the 0th and 1st order of Bessel functions of first kind. Upon detection (squaring the amplitude into intensity), the two sidebands act as stable phase references which form a beat note with the optical carrier field at frequency Ω and indirectly measures its phase shift. The amplitude of the beat note, after demodulation, yields the well known form of the PDH error signal given by

$$\epsilon \approx -2\sqrt{P_c P_s}\ \mathrm{Im}\left[\mathcal{F}(\omega)\mathcal{F}^*(\omega+\Omega) - \mathcal{F}^*(\omega)\mathcal{F}(\omega-\Omega)\right] \tag{2.3}$$

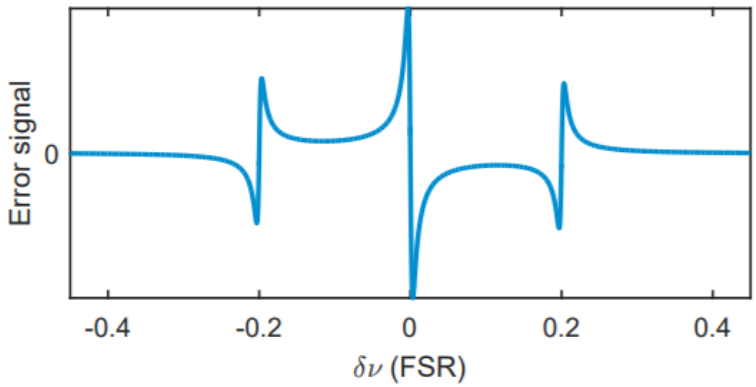

Figure 2.7 : The PDH error signal with modulation frequency of $\Omega = 0.2$ FSR. Laser detuning $\delta\nu$ with respect to the cavity resonance is plotted in units of cavity FSR. The steep slope near resonance is fed back into the laser controllers for frequency locking.

Figure 2.7 plots the shape of the error signal Eqn. 2.3 as a function of the laser frequency being scanned across the cavity mode resonance. It can be noted that ϵ is linear in the small region near resonance with $\epsilon = 0$ exactly on resonance ($\delta\nu = 0$). This allows using standard linear-systems control theory to lock the laser frequency at the cavity resonance by feeding ϵ back to the laser input, which minimizes ϵ until it vanishes.

It is worth noting that, the slope of error signal near resonance is proportional to $\sqrt{P_c P_s}$ where P_c and P_s are the carrier and sidebands power respectively. Therefore, for an optimized signal-to-noise ratio, a steep error signal is ideal. In other words, $\sqrt{P_c P_s}$ needs be maximized. Since all the sidebands power are determined by the Bessel functions, the optimum modulation depth is easily calculated to be

$$\frac{P_s}{P_c} = 0.42 \Longrightarrow \beta = 1.08 \tag{2.4}$$

The PDH technique is normally accompanied by a way to tune the laser frequency while it is locked to the cavity for typical experimental applications. This may be

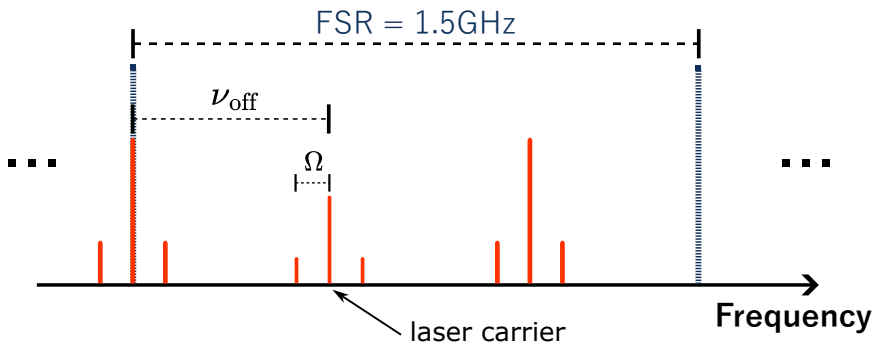

Figure 2.8 : Illustration of the relation between different sidebands. The PDH sidebands (at Ω) are used to generate PDH error signal shown in Equation 2.3. When the laser is locked to the cavity, the offset sidebands (at ν_{off}) determines the laser carrier frequency by setting its position relative to the selected cavity resonance.

realized by changing the cavity resonance frequency, e.g. by changing the mirror spacing of a Fabry-Perot cavity, in an adiabatic way such that the laser frequency feedback is undisturbed. In our case of fixed-length cavity, however, we apply another tunable phase modulation to the lasers in addition to the one used for PDH error signal generation. This results in another set of sidebands which we call offset sidebands. One of these offset sidebands is locked to the cavity resonance, so that the actual laser carrier frequency can be tuned by simply changing the offset sidebands' frequency. An illustration of this sidebands configuration is shown in Figure 2.8.

2.3.2 ULE cavity

The ULE cavity (part#: 6010-4) and the vacuum housing (part#: VH6010-4) are bought from Stable Laser System (SLS). The cavity has a plano-concave configuration with the radius of curvature of the concave mirror being 50 cm. See Appendix A.1 for more detailed specifications of the cavity mirror surfaces. The transverse modes associated with this configuration is discussed in later sections. The cavity is 10 cm long, which indicates a FSR of $c/2L = 1.5$ GHz. Based on the transmission data

provided (see appendix), neglecting absorption, the cavity finesse and linewidth can be roughly calculated as shown in Table 2.3

Wavelength (nm)	Transmission	Round trip loss	Finesse	FWHM (kHz)
640	0.00483%	0.00966%	65000	23.06
689	0.003472%	0.006944%	90480	16.58
698	0.0034054%	0.0068107%	92255	16.26

Table 2.3 : The ULE cavity finesse and linewidth at different relevant wavelength. The transmission data of the cavity mirrors is measured and provided by Stable Laser Systems (see Appendix A.1). All other parameters are calculated from the transmission data. Currently, the ULE cavity is only used for frequency stabilizing 640nm and 689nm; however, the mirrors are also coated to have high reflectivity at 698nm for potential inclusion of a 698nm laser in the future for the $(5s^2)\ ^1S_0 - (5s5p)\ ^3P_0$ clock transition.

Because of the high cavity finesse, it leads to a large resonant build up of optical power inside the cavity. Such high power could potentially damage the coatings on the cavity mirrors. Consulting with Stable Laser System reveals that the damaging threshold of the intra-cavity power is above 200kW. Considering that our input beams, for both wavelengths, typically has power below 1mW (including all sidebands), even after multiplying by the finesse, we are far from having to worry about optical damage.

2.3.3 Vacuum housing

As mentioned, the vacuum housing (part#: VH6010-4) is also designed and built by SLS to accommodate the particular cavity. As shown in Figure 2.9, the housing consists of an inner vacuum chamber being thermally insulated and radiation shielded and sitting inside an outer container chamber. Note that, in Figure 2.9(A), the cavity is not tightly confined on the mounting block (neither is the mounting block on the

two groves), so we can only say that the cavity sits roughly at the middle of the housing. This uncertainty on the exact position will be relevant for mode matching. While Figure 2.9(B) shows the same side of the housing as in A, the other side of the vacuum chamber is indium sealed and never opened.

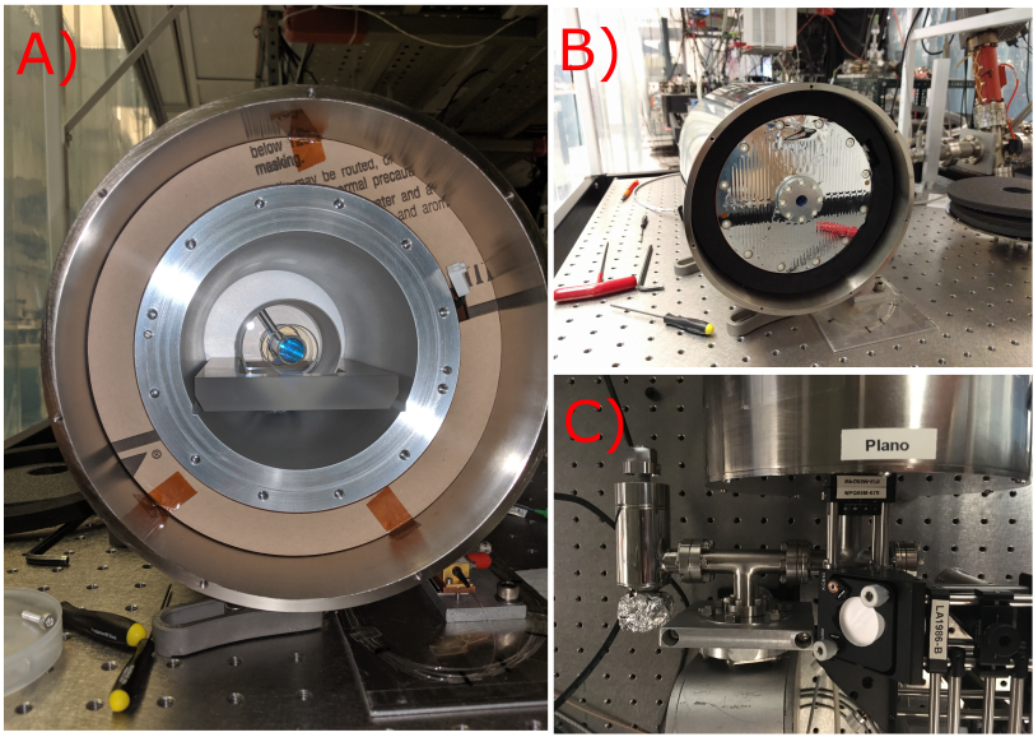

Figure 2.9 : **A)** The vacuum housing opened up during loading the cavity. The vent hole on the cavity substrate can be seen. The heater coils and radiation shield are blocked by the cardboard. **B)** The inner vacuum chamber was sealed after the cavity has been loaded. **C)** The other side of the housing viewed from top with all the connections in place.

As shown in Figure 2.9(C), a 1.33" conflat tee reaches out of the container chamber on this side for attachment to turbo and ion pumps. The first stage of the pumping was done with the oil-free turbo pump through an open all-metal valve (connection is made with the flange wrapped in aluminum foil). The valve was then closed and the ion pump took over after the pressure was down to its operation range. A Varian

ion pump controller is used to at 4800V output. Within weeks after that the pressure (as measured by the ion pump controller with default current-pressure calibration of $P_{100nA} = 1.8 \times 10^{-9}$ Torr) was roughly 5.3×10^{-9} Torr and has since been stabilized there.

Despite being ultra-low-expansion (ULE), the expansion of the ULE glass is still temperature dependent, and one can minimize the fluctuation of the expansion, thus of the cavity length, by stabilizing the temperature at the zero crossing point, which is the local minimum of the expansion-temperature curve. The measurement of the zero-cross temperature is shown in Figure 2.10 as done by SLS. They have used the standard method of locking a laser to the cavity at different temperatures and then beating it with a known stable reference laser for the frequency difference. The

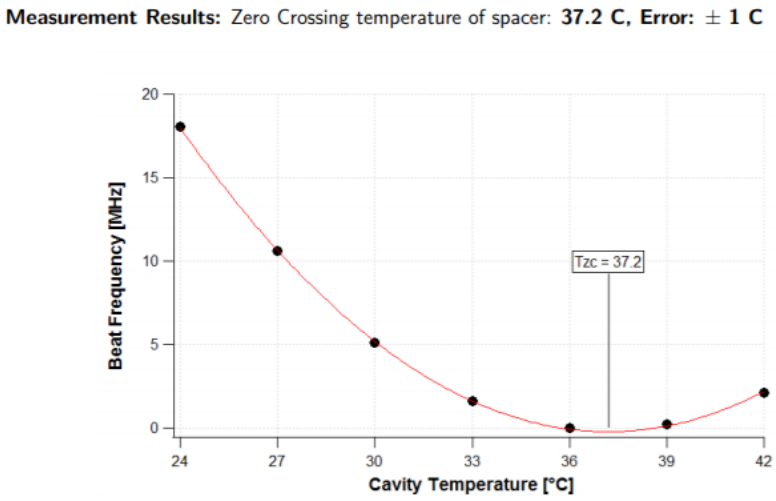

Figure 2.10 : Zero-crossing temperature measurement of the ULE cavity. Data shared by Stable Laser System, Inc.

measurement shows a zero-crossing temperature of 37.2°C, and this is where the temperature has been stabilized at.

A LFI3751 temperature controller is used as recommended by SLS. Since vacuum

housing only has a heater (no cooler), the current limit of the temperature controller output should be 1-directional (namely, setting one of the current limit to 0A). For specific relevant settings, we have adopted that suggested by SLS: positive and negative current limits at 0.00A and -1.50A respectively with the PID values set to P=85, I=1.5, D=0.

2.3.4 The PDH locking

The working principle of the PDH technique has been introduced above, here we briefly describe the optical and electronic setups for its realization. Specific discussion will be given for the 689nm system for necessary demonstrations.

Optical setup

Figure 2.11 shows the essential optical layout for the PDH setup. The 689nm and 640nm light are injected into the ULE cavity from opposite sides and have similar configuration. As a standard technique, a combination of polarizing beam splitter (PBS) and quarter-wave plate (QWP) is used to separate the reflected beams (dashed lines) from the incident beams. For both lasers, an electro-optic modulator (EOM) is used to generated the sidebands at frequency Ω as in Eqn. 2.2. This optical setup is primarily mounted in a cage system attached to the vacuum housing, and a photo of the actual setup is shown in Figure 2.12

In addition to being frequency selective, resonating modes inside a Fabry-Perot cavity also have well defined transverse spatial profile that can be calculated given cavity geometry. In order to inject the laser power efficiently into the cavity mode, the spatial profile of the incident beam must match that of the cavity mode. This is achieved by a single mode-matching lens for each of the 689nm and 640nm beams.

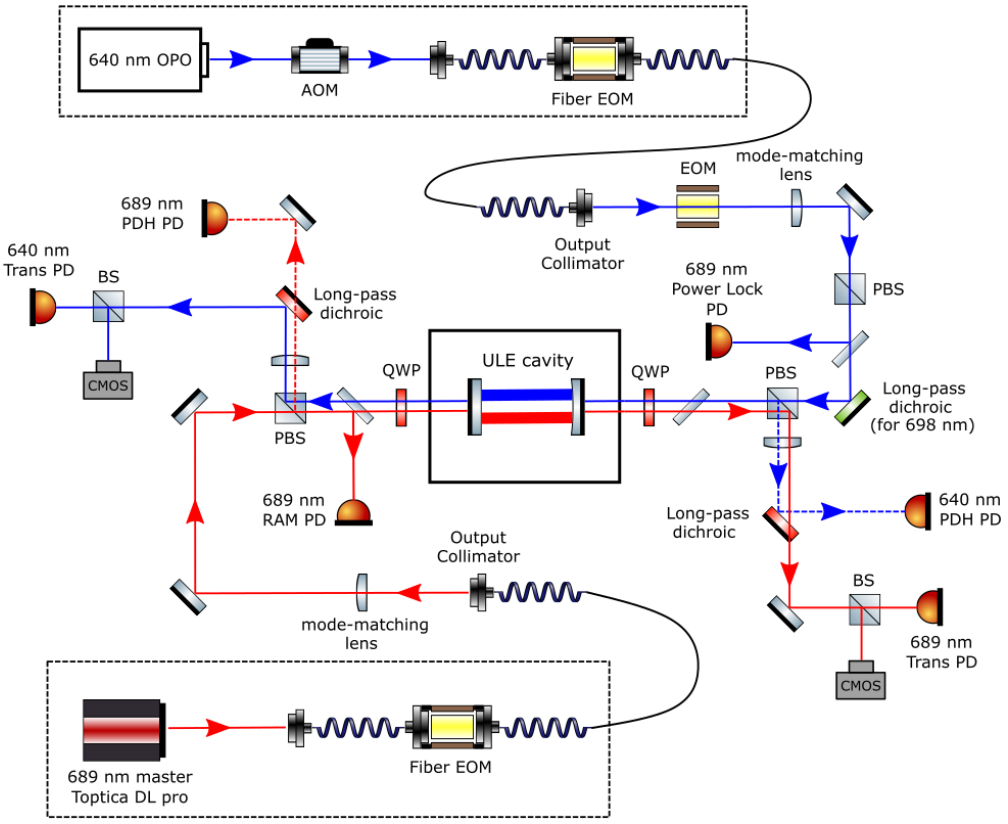

Figure 2.11 : The optical layout of the ULE cavity system. This diagram is abstract and does not represent the actual geometry of the setup. The 689 nm and 640 nm beams are drawn with red and blue color respectively, and the reflected light from the cavity is represented by dashed lines. PD: photodiode, QWP: quarter-wave plate, PBS: polarizing beam-splitter, BS: (non-polarizing) beam-splitter, RAM: residual amplitude modulation.

Detailed calculations of the mode profile of our ULE cavity and the measured laser beam profiles before and after mode-matching process is shown in Appendix A.2.

With the input beam profile matched to that of the cavity, misalignment of the beam may still cause the beam to overlap with and therefore couple efficiently into higher-order modes, examples of which are shown in Figure 2.13. In principle, any spatial mode can be used for the purpose of PDH locking, however, we choose to work with the TEM_{00} mode, as is typically chosen, for its circularly symmetric Gaussian

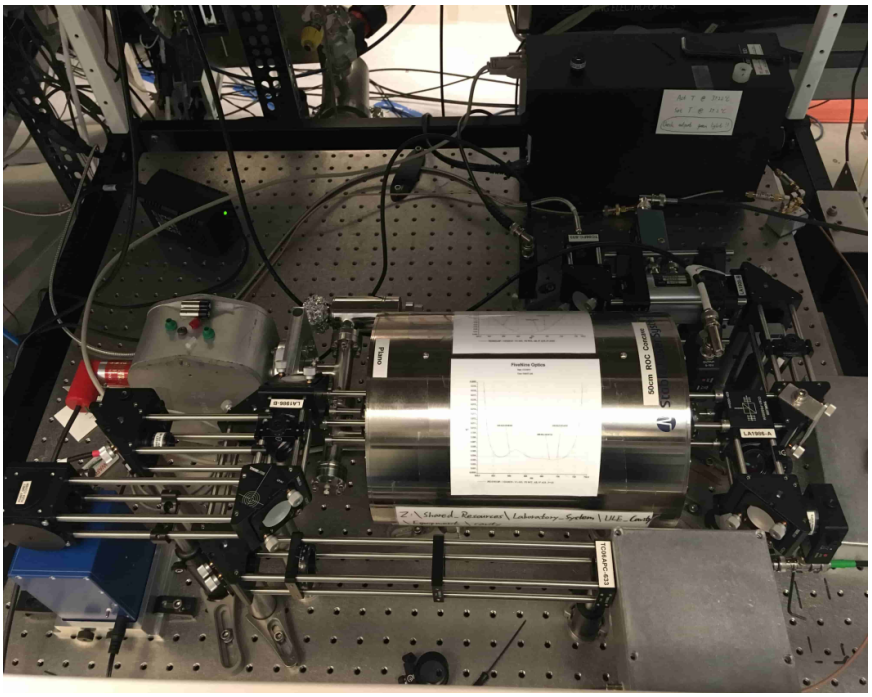

Figure 2.12 : Photo the ULE cavity optical setup taken in March 2020. The 689nm and 640nm lasers are brought to the table via fibers, and the rest of the entire optical setup shown in Figure 2.11 is mounted in the cage system in picture.

profile which is easy to shape the incident beam into. Moreover, higher-order TEM_{nm} modes are typically degenerate, which leads to near-overlapping error signals that can complicate the locking process. It should be noted that the transverse mode spacing can be calculated by

$$\Delta\nu = \frac{\cos^{-1}\left(\pm\sqrt{g_1 g_2}\right)}{\pi}\nu_{FSR} \tag{2.5}$$

where the g-factors of the two mirrors are $g_i = 1 - L/R_i$, and the plus (minus) sign is used if g_1 and g_2 have same (opposite) signs. For our cavity,

$$\begin{aligned} g_1 &= 1 - \frac{10\text{cm}}{\infty} = 1 \\ g_2 &= 1 - \frac{10\text{cm}}{50\text{cm}} = 0.8 \\ \Delta\nu &= 230\ \text{MHz} \end{aligned} \tag{2.6}$$

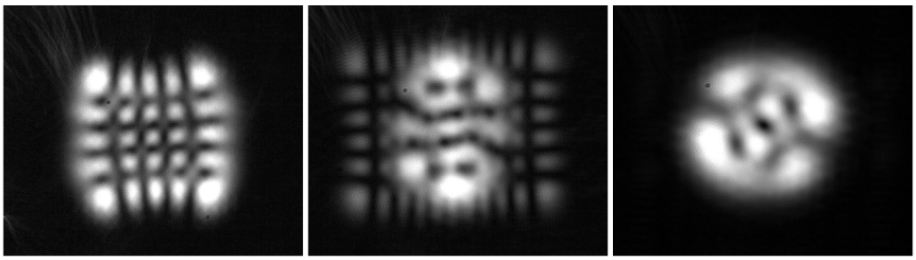

Figure 2.13 : Examples of several higher-order spatial modes. Pictures are taken with CCD cameras directly imaging the transmitted beam.

This gives the frequency spacing between adjacent ($\Delta[n+m] = 1$ for TEM_{nm}) transverse modes.

We have chosen a general figure of merit for the coupling efficiency into the TEM_{00} mode to be the relative height of its peak compared to that of other modes on the cavity transmission spectrum obtained by uniformly scanning the incident laser frequency. Figure 2.14 shows the oscilloscope trace of such a transmission spectrum with the offset sidebands frequency being scanned over a range covering more than an entire FSR. Peaks of transmission are observed corresponding to resonating modes with their transverse profile imaged with CCD camera shown in correspondence. On this transmission spectrum, the TEM_{00} peak is observed to more than ~ 10 times higher than the $\mathrm{TEM}_{01/10}$ peaks, while the other even higher-order modes are negligibly small on the shown scale.

RF setup

As explained above, the ideal modulation depth for the PDH sidebands is $\beta = 1.08$ for maximum slope of the error signal. The inherent modulation strength of an EOM is characterized by a quantity called V_π, which is the voltage required to be applied to the EOM to achieve a phase shift of π. The Jenoptik EOM used for modulating

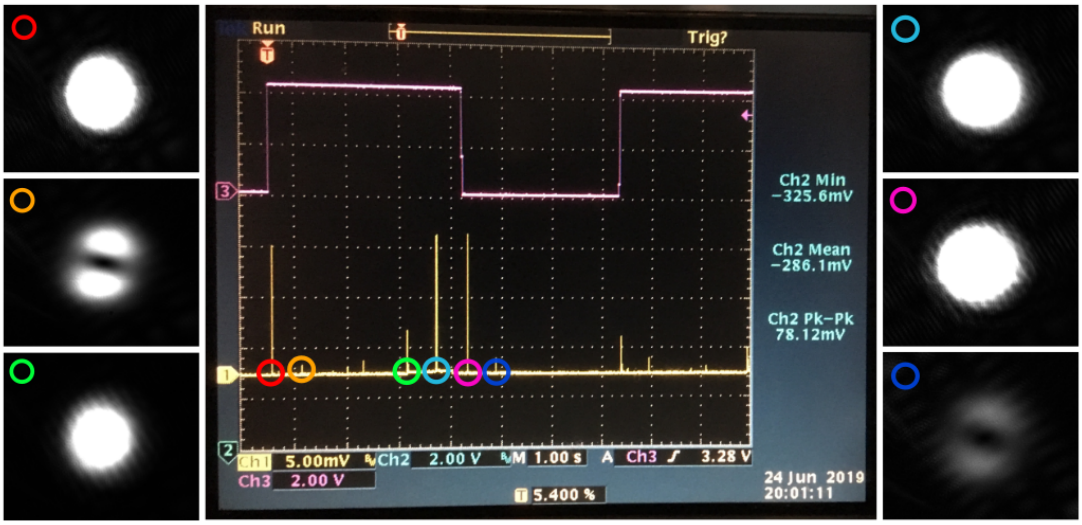

Figure 2.14 : Transmission spectrum of the ULE cavity covering a full free spectral range. Multiple repetitions of TEM_{00} are seen from different sidebands and FSRs. It can be confirmed however, by comparing the frequency spacing with $\Delta\nu$, the TEM_{00} peak circled in red and the $TEM_{01/10}$ peaks circled in yellow belong to the same sideban

the 689nm light has a manufacturer specified V_π of 3 V, which leads to an optimal RF power of approximately 10 dBm (or a peak-to-peak voltage of 2 V). For 689nm light, the offset sideband is created by the same EOM, and its modulation depth is set to maximize the fraction of power distributed in the first order sidebands. The power of different orders are given by the square of the corresponding Bessel functions. The first three orders are plotted as a function of the modulation depth in Figure 2.15. To achieve the peak at $\beta = 1.84$ shown in the graph, similar calculations indicates a RF power of 15 dBm (or 1.75 V peak-to-peak)

The diagram of the actual RF setup for generating the PDH error signal for 689nm laser is shown in Figure 2.16. A integrated PDH unit (enclosed in dashed rectangle) is purchased from SLS to generate a 20MHz local oscillator (LO) signal for the PDH sidebands. The PDH unit also includes a photo-detector measuring the

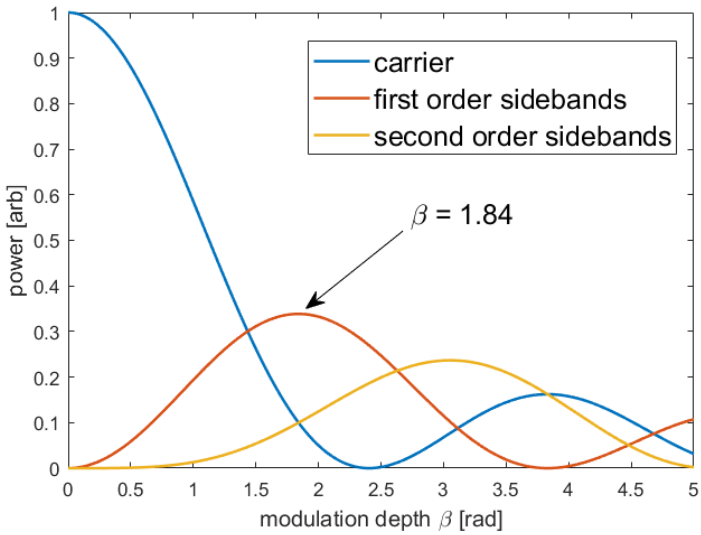

Figure 2.15 : Power distributed in the first three orders of sidebands calculated from the Bessel functions. The power in the first order is maximized at $\beta = 1.84$, which is the optimal condition for the offset sidebands.

cavity reflected intensity, which is then mixed with the LO signal to generate the error signal. A Novatech 409B synthesizer sources the offset sidebands frequency ν_{off} which is combined with Ω by the RF combiner before both getting amplified and applied to the fiber-coupled EOM. The Novatech 409B synthesizer is phase continuous, meaning that the output power and frequency undergoes no abrupt changes during the process of re-synthesizing new frequencies. This enables changing offset side-band frequency ν_{off} without disturbing the laser frequency stabilization.

Appropriate RF attenuators (Mini-Circuits VAT-XX+) and amplifier (Mini-Circuits ZX60-100VH+) are chosen to adjust the power in each set of sidebands such that the desired modulation depths β are achieved. A controllable phase delay can be added to the LO signal to optimize the phase matching in the mixing process, and this results in a standard-looking error signal shown in Figure 2.17.

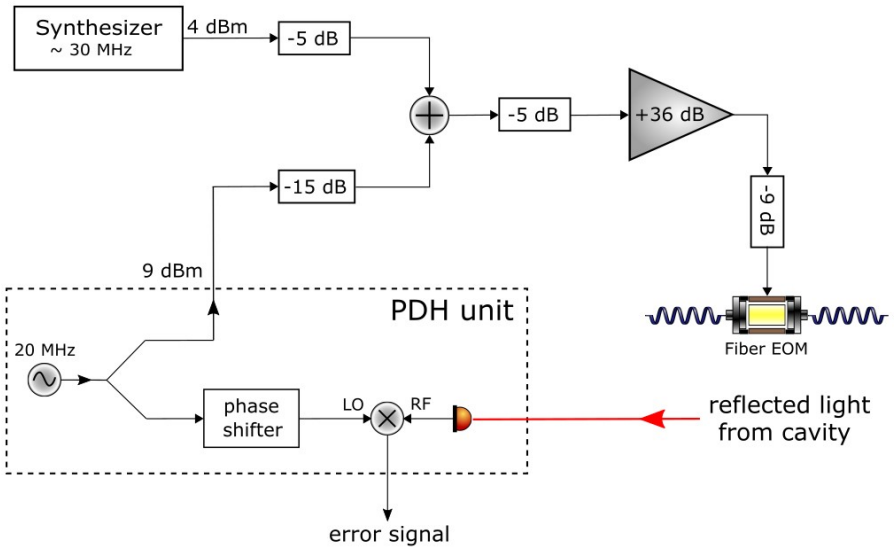

Figure 2.16 : The RF diagram of the 689 nm PDH system. The dashed rectangle encloses components inside the PDH signal unit, which is responsible for generating the sidebands frequency $\Omega = 20$MHz and mixing it with the cavity reflected intensity for error signal generation.

Laser frequency stabilization

The error signals such as shown in Figure 2.17 can be sent back to the laser inputs to realize feedback control of the laser frequency. In the case of PDH techniques with high-finesse reference cavities often consist of two signal paths, each of which is a standard PID controller.

For the 689nm system, for example, the error signal is sent through an fast analog controller (Toptica FALC110) for PID processing, where the signal is split into two frequency regimes. The lower-frequency (DC-10kHz) part is sent to the laser piezo input voltage, which has a lower open-loop bandwidth ($\sim$ 10kHz), to cancel slow drift of the laser frequency, keeping it in close vicinity of the cavity resonance. At the same time, the higher-frequency ($\sim$10kHz-10MHz) part of the error signal is fed back

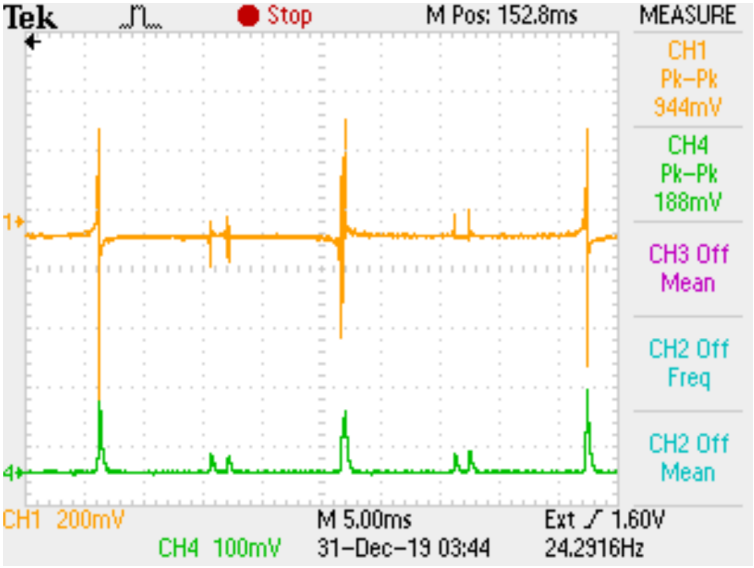

Figure 2.17 : Typical scope traces showing the PDH error signal (CH1) when an offset sideband of 689nm is scanned across an ULE cavity resonance. The corresponding cavity transmission trace is shown in CH4.

to the laser current control, which has a faster response (bandwidth around several ∼MHz), to suppress higher-frequency components of the laser frequency noise. This results in an effective total bandwidth of ∼ 1MHz for the feedback control of 689nm frequency. Figure 2.18 shows a typical noise spectrum of the PDH error signal when the feedback is engaged. As the servo (feedback) gain is increased from normal value (red), a servo bump appears around ∼ 1MHz. The appearance of the servo bump is the onset of oscillations of the control circuit, indicating that the gain is too high.

The absolute linewidth of the 689nm laser resulting from the frequency feedback control is not accurately characterized, and we estimate it to be less than ∼ 30kHz, which is the narrowest linewidth ever observed by doing shelving spectroscopy on the $(5s^2)^1S_0 - (5s5p)^3P_1$ transition with cold strontium atoms. The 640nm laser system has a similar frequency feedback setup, where the actuators of the slow and fast signal paths are the piezo control voltage of the original 1064nm fiber seed and an

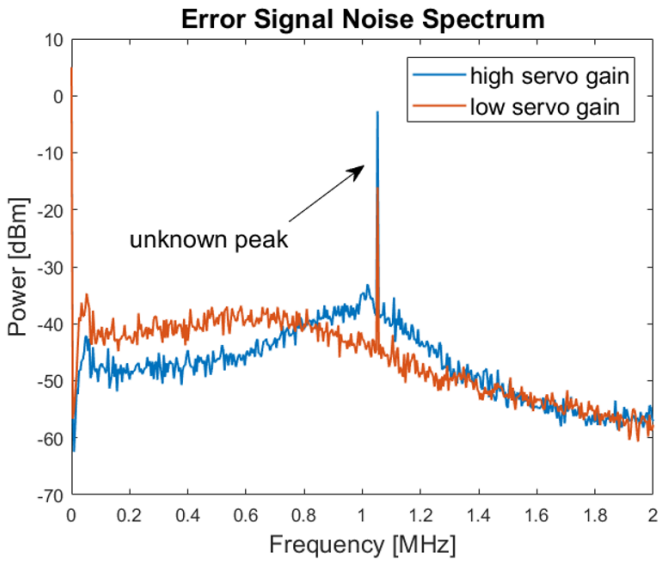

Figure 2.18 : Power spectrum of the PDH error signal obtained by taking its fast Fourier transform when the laser frequency feedback control is enabled. The same spectrum is measured with a low (red) and high (blue) servo gain.

acousto-optic modulator (AOM) shifting the laser frequency before sent to the ULE cavity (see Figure 2.11). The final linewidth of the 320nm UV light is estimated to be around $\sim$ 120kHz, larger than that of 689nm light because of the 1064nm fiber seed having a fundamentally broader spectrum than diode lasers. More details of the 640nm system can be found in Ref. [1].

One common issue in standard PDH laser stabilization is the possible residual amplitude modulation (RAM) caused either directly by the EOM or through other passive components. The frequency of the RAM signal is generally the same as the PDH modulation at Ω, which may lead to, after the demodulation, non-zero baseline offset of the error signal, degrading the lock performance. The RAM signal can be probed by sampling the incident beam right before entering the cavity, and a brief discussion of how we characterize the RAM can be found in Appendix A.3.

Long-term cavity drift

In addition to thermal expansion which has been minimized by temperature stabilizing the ULE cavity at the zero-crossing point 37.2°C as shown in Figure 2.10, there still exists a residual drift in the cavity resonance frequencies. This originates from the creeping of the ULE spacer glass, which results in gradual decrease of the cavity mirror spacing on a time scale of ∼nm/year. This seemingly extremely slow time scale, however, corresponds to a non-negligible drift rate of the resonance frequencies on the order of ∼ 10kHz/day.

It is important to accurately characterize and compensate for this cavity drift, particularly for the 689nm light since a fixed laser frequency is needed for optimal operation of the narrow-line laser cooling. To this end, part of the 689nm master light is sampled and sent to a strontium vapor cell (see Figure 2.4). An AOM is used to shift the frequency of this beam to perform frequency-modulated saturated absorption spectroscopy (SASP) on the $(5s^2)^1S_0 - (5s5p)^3P_1$ transition on the atomic vapor. I have built an automated LabVIEW program (Figure 2.19) to repeatedly scan the AOM frequency and measured the SASP spectrum, from which the relative spacing between the laser frequency ν_{laser} (when locked to the cavity, i.e. $\nu_{atom} = \nu_{cavity}$) and the atomic resonance ν_{atom} is determined. Since ν_{atom} is constant, the change in the spacing $\nu_{laser} - \nu_{atom}$ indicates the drift of the cavity resonance ν_{cavity}. Linear fitting the measured cavity drift, as shown in the Figure 2.20, yields a drift rate, which can be used to adjust the offset sidebands frequency ν_{off} such that the relative spacing $\nu_{laser} - \nu_{atom}$ is constant. In particular, we have chosen such that

$$\nu_{laser} - \nu_{atom} = 82\text{MHz} \tag{2.7}$$

The LabVIEW program is configured to update ν_{off} about once per minute to achieve

Figure 2.19 : The front panel of the LabVIEW control VI managing the long-term stabilization of the 689nm laser frequency. The program scans the frequency applied to the AOM shifting the SASP beams, which yields the frequency modulated SASP spectrum (top-right). The spectrum is fitted to an asymmetric Gaussian lineshape to determine the resonance position, which gives $\nu_{laser} - \nu_{atom}$.

that. Since the Novatech 409B synthesizer used to supply ν_{off} is phase continuous, the 689nm laser maintain locked to the cavity during the changing of ν_{off}.

The cavity drift rate is also observed to change on a time scale of months. While it is around 14.6 kHz/day as shown in Figure 2.20 in Dec 2020, as of Jan 2025 the newest measurements suggest a drift rate of $\sim$ 9kHz/day. During this time, the required offset sidebands frequency has also changed from $\sim$ 30MHz to $\sim$ 45MHz.

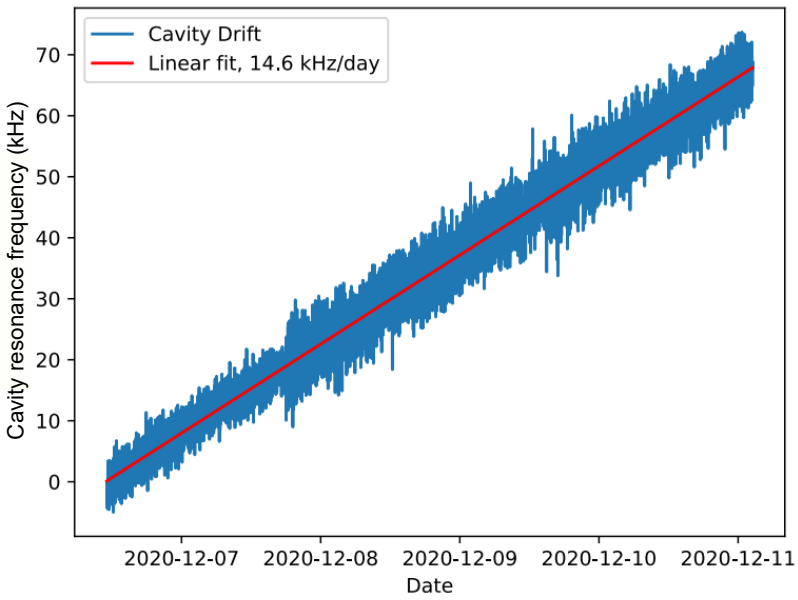

Figure 2.20 : Measured resonance frequency of ULE cavity mode by performing saturated absorption spectroscopy on the $(5s^2)^1S_0 - (5s5p)^3P_1$ transition in ^{88}Sr atomic vapor using the 689nm laser when locked to the cavity. The frequency is referenced to the time at the start of the data taking. Data are sampled over a time span of several days and fitted to extract a linear drift rate of 14.6 kHz/day.

2.3.5 Singlet laser system

Since we will be conducting microwave transition and synthetic dimension experiments with both the triplet and singlet Rydberg series as shown in Figure 2.3, similar laser frequency stabilization systems are constructed to lock the 461nm and 413nm Rydberg excitation photons to another ULE cavity. More details about the singlet laser system is presented in Ref. [110], and here we will present a brief description of the essential components.

Both of the 461nm and 413nm light are produced by second harmonic generation (SHG) in Toptica TA-SHG pro modules. Master source laser at 922nm (826nm) is amplified by tapered amplifier (TA) before entering the SHG cavity where they pump the SHG crystals to generate the frequency doubled light at 461nm (413nm)

with typical maximum output power of $\sim$ 50mW.

The singlet ULE cavity is purchased to have a high finesse at the master wavelengths 922nm and 826nm, which are sent to the cavity for PDH locking. The involved optical and RF setups are, in essence, the same as that has been described above for the 689nm. Because of the source of 922nm and 826nm both being diode lasers, which have intrinsically narrower linewidth, the singlet Rydberg excitation has a combined linewidth of $\lesssim$ 40kHz.

Both 461nm and 413nm light are sent to the science chamber using fibers, and they shine on the atoms with the same counter-propagating configuration as in the triplet case (see Figure 2.5). The 461nm laser is fixed at frequencies far blue detuned in the range of $\Delta \approx 6-18$GHz from the $(5s^2)^1S_0-(5s5p)^1P_1$ transition to suppress off-resonant scattering, and frequency of the 413nm light is adjusted to hit resonances of Rydberg states. Both beams have power of up to $\sim$ 10mW with diameters of $\sim$ 1mm.

2.4 Microwave setup

Transitions connecting Rydberg levels constitute the core of the synthetic dimensions. It is therefore critical to have precision and stability in the frequency sources driving these transitions. Fortunately, the Rydberg-Rydberg transition frequency for our typical range of quantum number ($n \sim 45 - 70$) lies within the microwave range of 10-50 GHz, where affordable commercially available sources offer excellent frequency stability (sub-Hz linewidth) and tunability.

Unlike optical laser beams, the propagation of microwave fields is more perturbed by the physical environment as its wavelength is similar to the dimensions of the experimental apparatus (mm-cm scale). Figure 2.21 shows the positioning of the microwave horn antenna with respect to the experimental chamber. The microwave

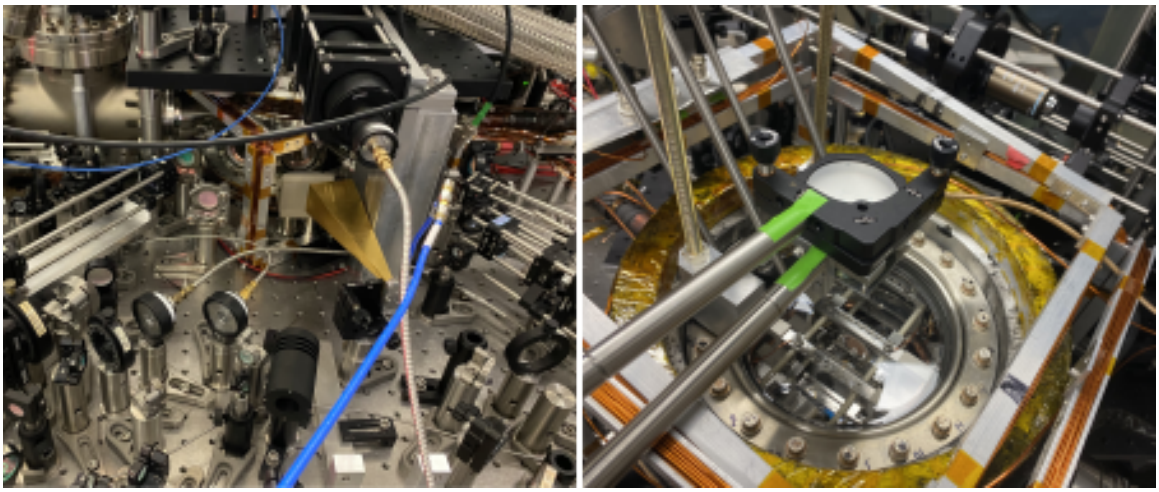

Figure 2.21 : Comparison of the microwave radiation access of the Rydberg apparatus and the under-construction Tweezer apparatus.

radiations emitted from the horn is directed at the atoms through a vacuum viewport with a diameter of 1.5 inches, which sets a lower cut-off frequency of about 5 GHz that we may consider using. More discussions on the initial selection of quantum number and frequency range can be found in the previous work [6]. In this thesis, we will continue using the K-band ($\tilde{1}$7-27 GHz) horn for the majority of the transitions studied. The following section will describe in detail the frequency sources and microwave circuitry used to access different ranges of quantum numbers and types of transitions.

As a general remark, since the current Rydberg apparatus is not originally designed for the synthetic dimension experiment, many aspects of it constitute a non-ideal environment for the microwave fields. For example, the propagation path from the horn to the atoms is directly intercepted by a 2 inch metallic mirror mount (see Figure 2.21), which can cause uncontrolled reflections of the microwave and lead to polarization distortions. The inside of the experimental chamber, which houses metallic

components such as the electric-field plates, can induce frequency- and polarization-dependent interference patterns at the experimental region. These effects are not characterized for the current setup.

2.4.1 Frequency generation methods

Direct synthesis and combining

The synthetic dimension experiment, which is the main result of this thesis and will be discussed in detail in Chapter 4, uses six levels in the $5sns$ ($^3S_1$) Rydberg series around $n \sim 60$ to construct the synthetic lattice. The frequencies of the $nS-(n+1)S$ transitions connecting these adjacent pairs range from $15 - 20$ GHz, which we can directly synthesize using Windfreak SynthHD PRO dual-channel signal generators. Each channel can output up to 24 GHz with maximum power of about $10 - 15$ dBm, and the phase noises are extremely low at less than $-80\,\mathrm{dBc/Hz}$. Since the synthetic dimension experiments requires simultaneous emission of multiple microwave tones to connect the ladder of Rydberg levels, the output signals are then combined using RF combiners (RFLT4W2G26G & RFLT2W2G26G) before passing through the switch (RFSPSTA0218G) and arriving at the horn (RW42HORN25A).

The diagram of this setup is shown in Figure 2.22. The current configuration supports up to 8 frequency sources to be combined, which results in an inherent power loss of 9 dB in each tone. However, as later presented measurements will show, with this microwave power level, we are still able to achieve $\sim$1 MHz Rabi coupling frequency for all $nS - (n + 1)S$ transitions of interests. The combining method is chosen for the synthetic dimension experiments because it generates the cleanest multi-tone frequency spectrum as there is minimum nonlinear processes involved.

One minor drawback of direct synthesis is that, during the experiments, frequen-

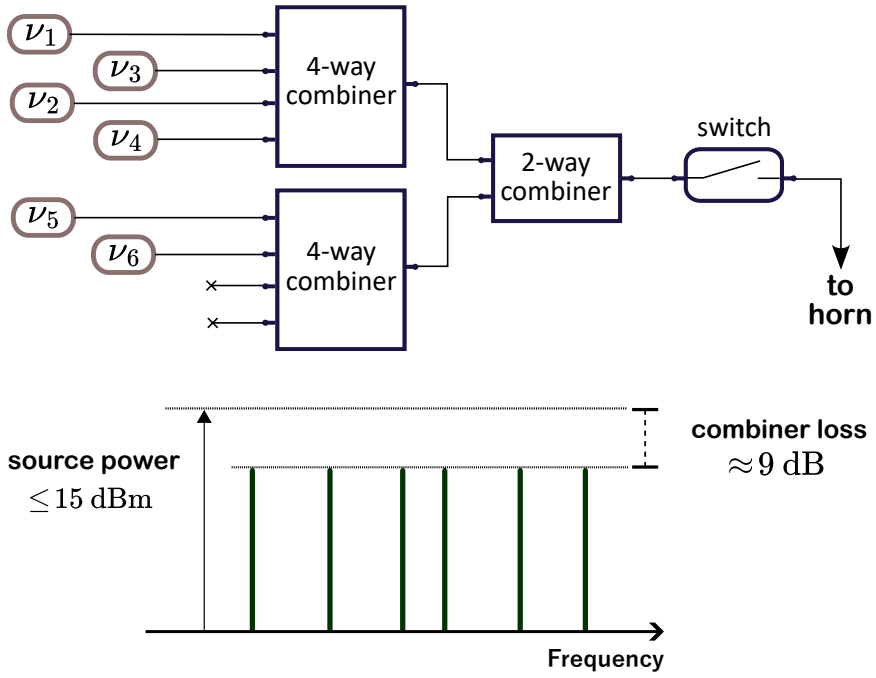

Figure 2.22 : Schematic diagram of the combiner-based setup for generating the microwave tones sent to the horn antenna. Up to eight tones can be combined, and two of the inputs are left empty in the current setup. All the tones (channels) experience an nearly uniform combiner loss of $\sim$ 9dBm.

cies that are (near)-resonant with the atomic transitions are present at the source. This can potentially lead to microwave fields leaking through the powering system, causing atomic transitions to be driven even when the microwave fields are supposedly turned "off" by the switch RFSP2TA1840G in Figure 2.22 (see 3.1.1 for details).

Mixing

Another commonly used method of microwave frequency generation is based on RF mixers, which are passive nonlinear devices with two essential inputs: local oscillator (LO) and intermediate frequency (IF). A mixer suppresses the carrier signal (from LO) and redistributes the power into primarily the 1st-order sidebands with frequencies

LO+IF and LO-IF at the output. For the first experiments with Rydberg synthetic dimensions, and a small fraction of the experiments described here, we used a mixer setup to generate the microwave frequencies. As shown in Figure 2.23, we use a doubled balanced mixer (PE86X1009) with the LO being supplied by the ~ 13 dBm output of a DS-3000 synthesizer (or similarly using the Windfreak SynthHD PRO). The LO signal is kept at a fixed frequency while the IF frequency is tuned to control the resulting sideband frequencies. The IF port can also take input from multiple tones through a combiner to realize multiple tones.

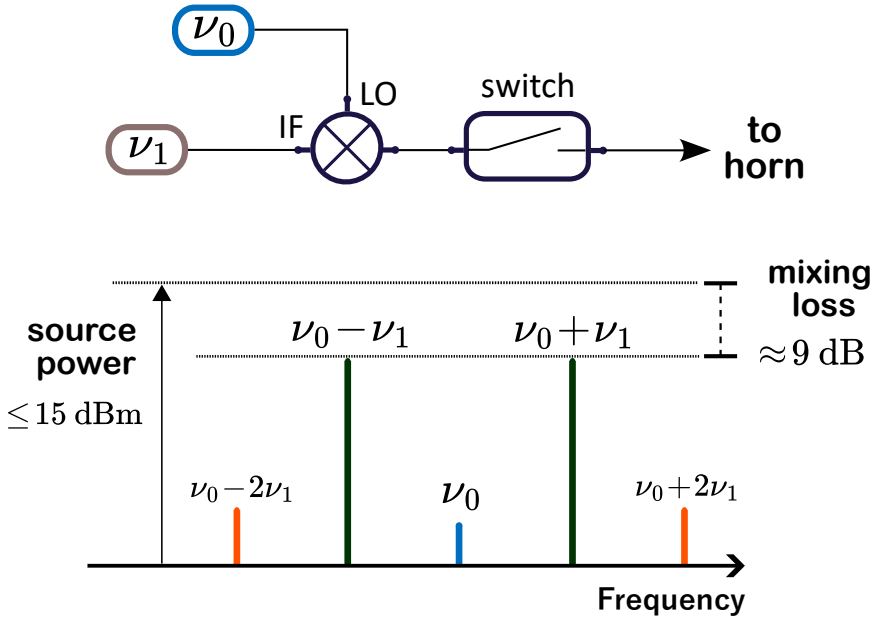

Figure 2.23 : Schematic diagram of the mixer-based setup for generating the microwave tones sent to the horn antenna. For the measurements done with mixer setup in this thesis, only a single tone is being mixed with the local oscillator (LO). The output of the mixer is designated to suppress the LO signal at ν_0 and the higher order sidebands $\nu_0 \pm n \cdot \nu_1$. Typically, one of the first-order $\nu_0 \pm \nu_1$ sidebands is selected to be used to drive microwave transitions.

The most obvious advantage of using the mixer is the ability to generate frequencies (on the LO+IF sideband) higher than that can be directly synthesized. Our

current mixer setup can generate frequency of up to $\sim$34 GHz (with LO at 24 GHz and IF at 10 GHz both from the Windfreak SynthHD PRO channels), which covers quantum number as low as $n \approx 50$. The main drawback of the mixing scheme is that the unused sidebands (and the LO carrier), when not properly filtered, can lead to undesirable microwave signals that may cause accidental resonances with irrelevant transitions and additional AC Stark shifts.

Frequency Multiplication

For principle quantum number $n \lesssim 50$, transition frequency between adjacent Rydberg states approaches $\sim$40 GHz, beyond what is accessible with the mixing scheme. In this regime, we rely on frequency multiplication using a passive doubler (model U2 by Pacific Millimeter Products) with an output frequency range of 40$-$60 GHz. With the Windfreak SynthHD PRO providing a fundamental source frequency of up to 24 GHz, the doubled output goes up to 48 GHz, reaching principle quantum number as low as $n \approx 43$.

The output of the U2 passive doubler is directly coupled to a WR-19 waveguide horn antenna (RW19HORN25C) which emits 40$-$60 GHz efficiently. Although the synthetic dimension experiments mainly involve transitions around $n \sim 60$, the doubler-based setup was used to test the possibility of driving lower-n transitions, which may be used in future experiments. For even lower quantum numbers ($n \sim 40$), one may switch to other similar frequency multipliers (e.g. doubler model E2LF, tripler model U3).

Chapter 3

Microwave-driven Rydberg transitions

As briefly mentioned before, the microwave-frequency Rydberg transitions studied in this thesis cover a wide range of quantum numbers ($n \approx 46 - 70$) and multiple types: S-S, S-P, S-D, D-F. Note that, in all types, the initial states (S or D-state) need to be accessible via our two-photon optical excitation path. This chapter summarizes characterization methods and measured results of these transitions including resonant frequencies, coupling strength, AC Stark shifts and coherence times. For the S-S and S-P transitions particularly, a focus of discussion will be put on exploring their suitability for the construction of Rydberg synthetic dimensions.

With the values of quantum defect measured [7] or quoted from previous studies [8, 111], the state energies of the Rydberg levels and hence their separations (transition frequencies) can be calculated relatively accurately as

$$\Delta E_{n',l',j',n,l,j} = -\frac{\mathrm{Ry}_{84}}{[n' - \delta(n',l',j')]^2} + \frac{\mathrm{Ry}_{84}}{[n - \delta(n,l,j)]^2} \tag{3.1}$$

using the Rydberg constant Ry_{84} mass corrected for the ionic core of ^{84}Sr as $\mathrm{Ry}_{84} = \mathrm{Ry}_{\infty} M_{84}/(m_e + M_{84})$. Figure 3.1 shows the transition frequencies predicted for several Rydberg levels around $n \sim 60$. The microwave frequency is scanned around the predicted value to look for spectroscopic signatures of the transitions, and the actual transitions are typically found (see Section 3.2) within $\sim$10 MHz of the predictions.

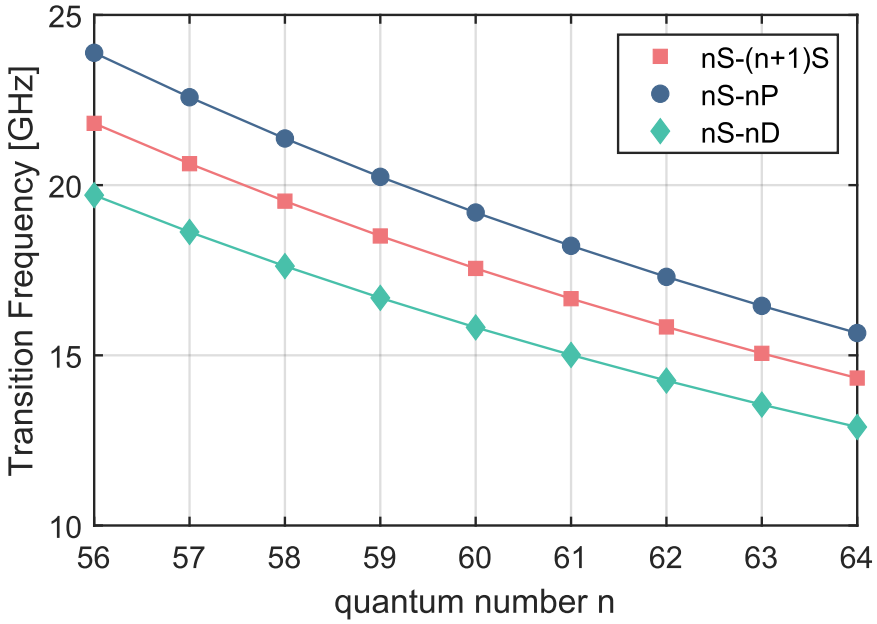

Figure 3.1 : Resonance frequencies $\Delta E_{n',l',j',n,l,j}$ predicted for transitions between singlet Rydberg levels around $n=60$. Previously accepted quantum defect values are used here: $\delta \approx 3.269$ for $5sns\ ^1S_0$, $\delta \approx 2.730$ for $5snp\ ^1P_1$, $\delta \approx 2.381$ for $5snd\ ^1D_2$. Note that for $nS-(n+1)S$ and $nS-nD$, both of which are two-photon transitions, values shown here are the frequency per photon.

3.1 Spectroscopic methods

Calculations shown in Figure 3.1 only predict the transition frequencies between Rydberg states. For constructing synthetic dimensions, however, other characteristics such as Rabi frequency and coherence time of the transitions are essential. Moreover, application of the microwave fields causes AC Stark shift through off-resonant couplings to other levels [11, 112], which can result in deviations between observed transition frequencies and the predictions. The AC Stark shift has different manifestation in different spectroscopic schemes, which will be described individually in this chapter.

The three spectroscopic schemes used in this work are Rabi method, Ramsey

sequence and Autler-Townes spectroscopy. They each correspond to distinct optical/microwave exposure sequences. At the end of the sample preparation stage as discussed in Section 2.1, $\sim$1M ^{84}Sr atoms are trapped in the ODT at a temperature of $\sim 1\,\mu$K. Such a cloud of atoms are exposed to 1000 repetitions of the sequence as shown in Figure 3.2, where different spectroscopic schemes generally share the same sample preparation and SFI detection sequences. In the experiments, the power of

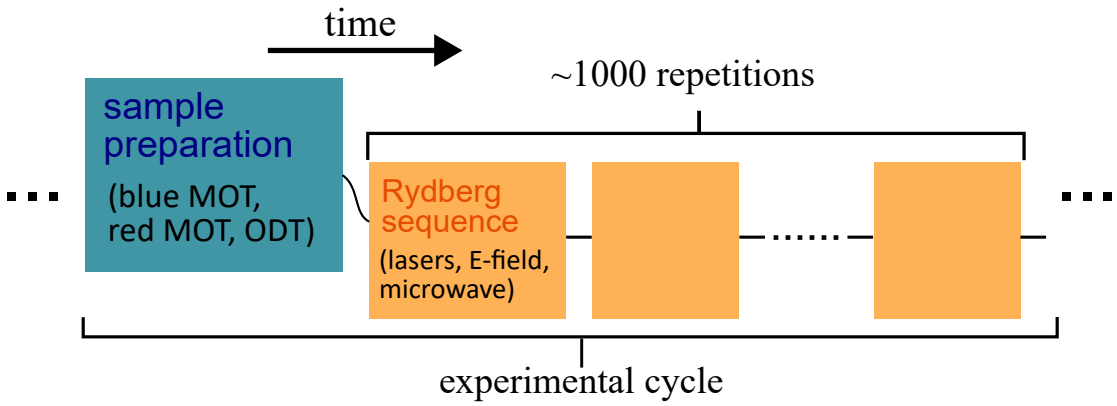

Figure 3.2 : Generic experimental cycle for microwave transition experiments. For each atomic sample prepared, typically $\sim$ 1000 repetitions, each of which is $\sim 200\mu$s long, of Rydberg excitation loops are applied. Detailed exposure sequences vary with different spectroscopic method as will be described below.

the excitation laser beams are controlled such that $\lesssim 1$ Rydberg atom is created per cycle after taking into account the detector quantum efficiency. This suppresses the possibility of having multiple Rydberg atoms simultaneously which introduces Rydberg-Rydberg interactions, causing undesirable complications. This is also to say that all experimental results in this thesis should be considered studies of single-atom physics.

3.1.1 Rabi spectroscopy

The concept of Rabi oscillation, which is a cornerstone of modern atomic physics, is usually understood in a picture where population of a two-level atom coupled to electromagnetic radiation at a fixed frequency ω (near its resonance frequency ω_0) oscillates in time between its two levels. Assuming that the atom is initially in the ground state $|g\rangle$, in the resonance case ($\omega = \omega_0$), the population in the excited state as a function of time is given by

$$P_e = \sin^2\left(\frac{\omega_r}{2} \cdot t\right) \tag{3.2}$$

where it is easy to see that the frequency at which the population oscillates is ω_R, which is called the Rabi frequency. The value of Rabi frequency also quantifies the strength of atom-light coupling giving rise to the oscillations. In the case where the radiation is off-resonance ($\omega \neq \omega_0$), the oscillations take the modifed form

$$P_e(t) = \frac{\omega_r^2}{\Omega_R^2} \sin^2\left(\frac{\Omega_R}{2} \cdot t\right) \tag{3.3}$$

where

$$\Omega_R = \sqrt{\omega_r^2 + \delta^2} \tag{3.4}$$

is called generalized Rabi frequency with $\delta = \omega - \omega_0$ being the detuning.

It can be noted from Eqn. 3.3 that the resonance is the point where the peak population transfer to the excited state maximizes and the oscillation frequency minimizes, making Rabi oscillation an indicator of the resonance condition. However, away from resonance ($\delta > \omega_r$), the diminishing amplitude of the population transfer makes directly observing the oscillations difficult. Therefore, for initial search of a Rydberg-Rydberg microwave transition, we typically scan the microwave frequency

ω while fixing the exposure time t. The corresponding exposure sequence is shown in Figure 3.3. Take the example of searching for the transition $5sns\ ^3S_1 - 5snp\ ^3P_0$

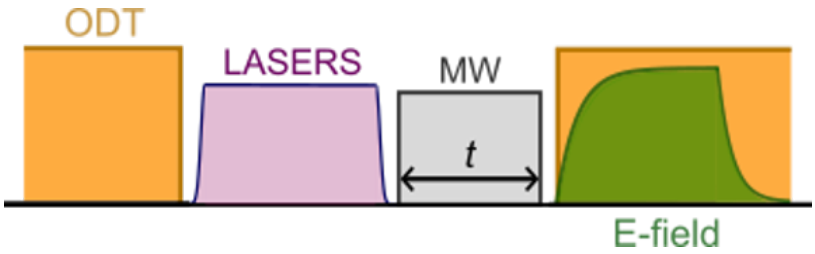

Figure 3.3 : Illustration of the exposure sequence used for initial search of microwave transition and coherence time characterization via decay of Rabi oscillations. The laser pulse arrives first to promote an atom into the frequency selected Rydberg state, and the microwave field is turned on subsequently to drive transitions between Rydberg levels.

$(nS - nP)$, the excitation lasers are pulsed on first, initializing an atom to the nS Rydberg level. The laser pulse is then followed by the exposure of microwave fields, which are set at a medium power (several dBm at the source synthesizer) with adequate exposure time ($\sim 5\mu s$). These settings are empirically chosen for an estimated Rabi frequency of $\omega_r/2\pi \sim 1$ MHz. Immediately after the microwave exposure, the ionization field is turned on, and the nP and nS states get ionized and detected by the MCP sequentially as the electric field strength ramps on gradually, allowing measuring the population fraction in each of the two states as demonstrated in Figure 3.4. Repeating this measurement yields P_{nP} (and P_{nS}) as the microwave frequency ω is scanned, which is expected to have the form of Eqn. 3.3. Figure 3.5 shows the theoretical lineshape as a function of the detuning δ plotted in units of Rabi frequency ω_r. The oscillatory behavior and the width of the central feature capture the scale of the Rabi frequency ω_r. In addition, the position of the center peak (or dip, depending on the set exposure time t) gives the resonance frequency $\omega_0^{(Rabi)}$ with uncertainty less

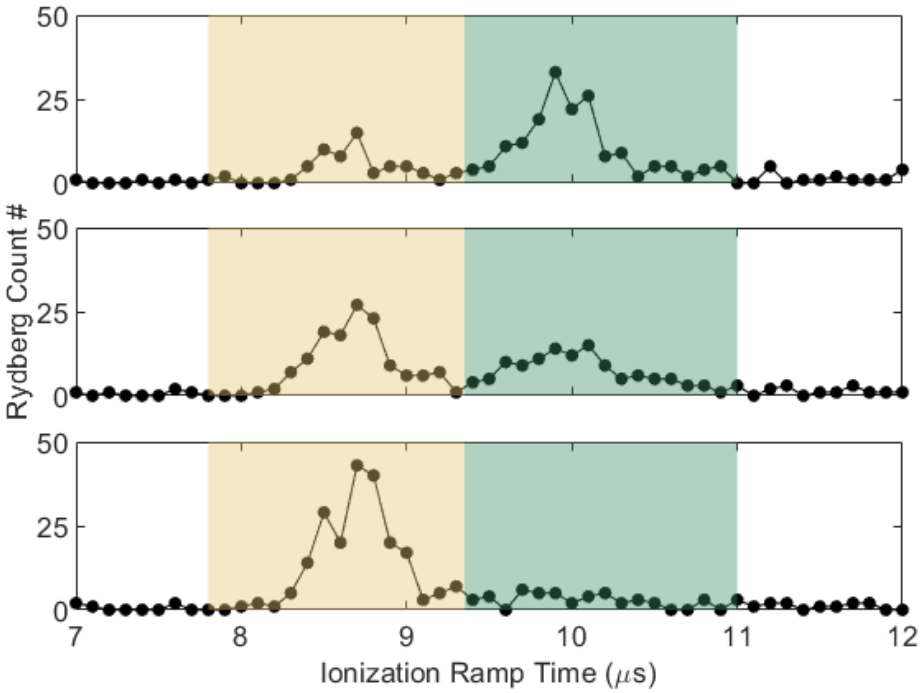

Figure 3.4 : Example ionization spectra showing the presence of both 58S and 58P states. Population fraction can be obtained by summing signals over windows (pink: 58P, blue: 58S) of arrival time. The ionization voltage ramp used here produces a maximum field of ~ 40 V/cm.

than $\sim \omega_r$, good enough for an initial search.

The microwave frequency can now be set to be fixed at the measured resonance frequency $\omega_0^{(Rabi)}$, and the experiments can be repeated with the same sequence but with exposure time t being the scan parameter. The result is the Rabi oscillations as shown in Figure 3.7, which provides a way to inspect the coherence property of the given microwave transition. For state dynamics measurements in Rydberg synthetic dimension experiments (see Chapter 4), it is critical to ensure that the characteristic coherence time of the Rydberg synthetic lattice connected by microwave transitions is long enough to observe the expected dynamics. This characteristic time scale is collectively determined by the coherence time of individual transitions in the

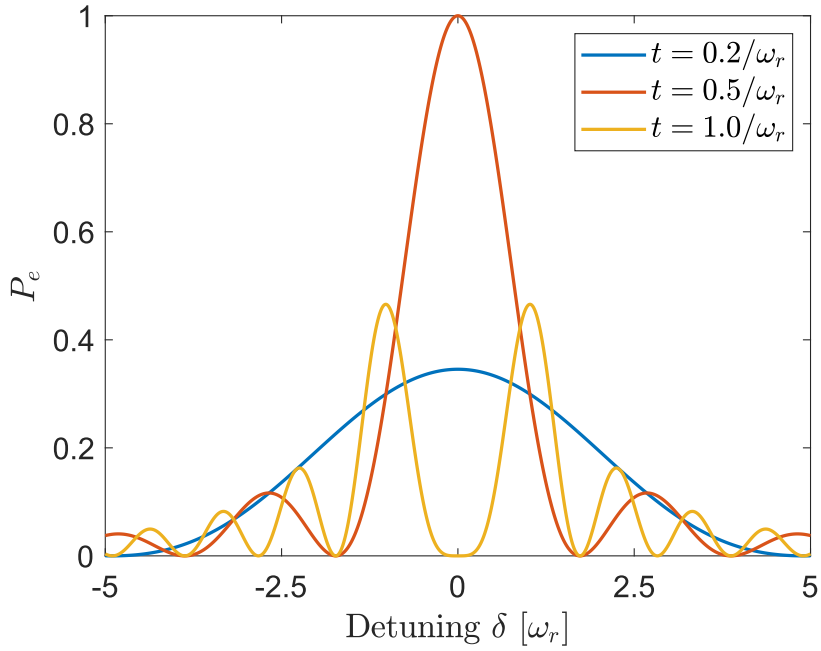

Figure 3.5 : Theoretical spectral lineshape of Rabi method. The excited state probability is plotted as a function of detuning δ (in units of ω_r). At different exposure time t (in units of $1/\omega_r$) of the driving field, peaks or valley may be expected at the resonance $\delta = 0$.

interaction zone (i.e. during the on-time of microwave fields). Here we assume that the combined effect of all sources of decoherence (including natural lifetime, blackbody radiation-induced transitions, off-resonant coupling to irrelevant states, background collisions, etc.) results in an exponential decay in the form $\exp(-t/\tau_{Rabi})$ superposed on the Rabi oscillations, which can be fitted to extract this coherence time τ_{Rabi} for each transition as demonstrated in Figure 3.7.

Note that the Rabi spectroscopy method of a transition requires selective detection of the two states involved. This is satisfied for most of microwave-driven Rydberg transitions of interest in this work except for the $(n-1)P-nS$ transitions, which will not be studied in detail. While the Rabi spectra as in Figure 3.6 and Rabi oscillations as in Figure 3.7 can both, in principle, be fitted to extract the resonance frequency

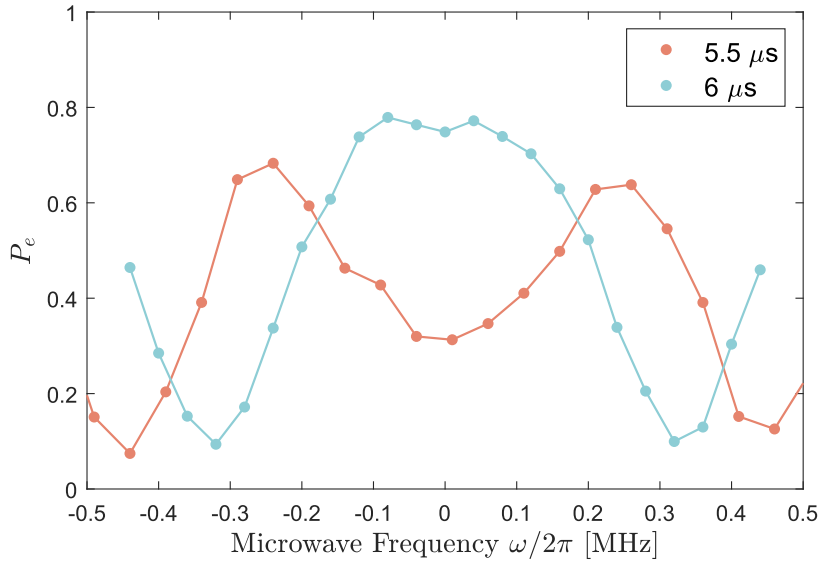

Figure 3.6 : Rabi spectrum of the $5s58s\ ^1S_0 - 5s58p\ ^1P_1$ transition measured at two different exposure time of $5.5\mu s$ and $6\mu s$. The excited state probability P_e as a function of the microwave frequency, which is referenced to the position of the center peak in the $t = 6\mu s$ spectrum.

$\omega_0^{(Rabi)}$ and Rabi frequency ω_r, we leave their measurements to the Autler-Townes method, which provides a more comprehensive characterization of each transition and will be discussed in a later section.

So far, I have labeled the resonance frequency obtained via Rabi spectroscopy with a superscript as $\omega_0^{(Rabi)}$. This is because the observed $\omega_0^{(Rabi)}$ is generally not equal to the intrinsic unperturbed resonance frequency ω_0, but experiences an AC Stark shift as a result of the microwave field itself. For a generic atomic state $|nlj\rangle$ characterized by the electronic quantum numbers n, l and j, application of radiation at frequency ω causes its energy to be shifted by

$$\Delta E_{nlj} = -\frac{1}{4}\alpha_{nlj}(\omega) \cdot \mathcal{E}^2 \tag{3.5}$$

where the polarizability $\alpha_{nlj}(\omega)$ quantifies the easiness of inducing a dipole moment on the atom at frequency ω. This dipole moment is proportional to the field amplitude

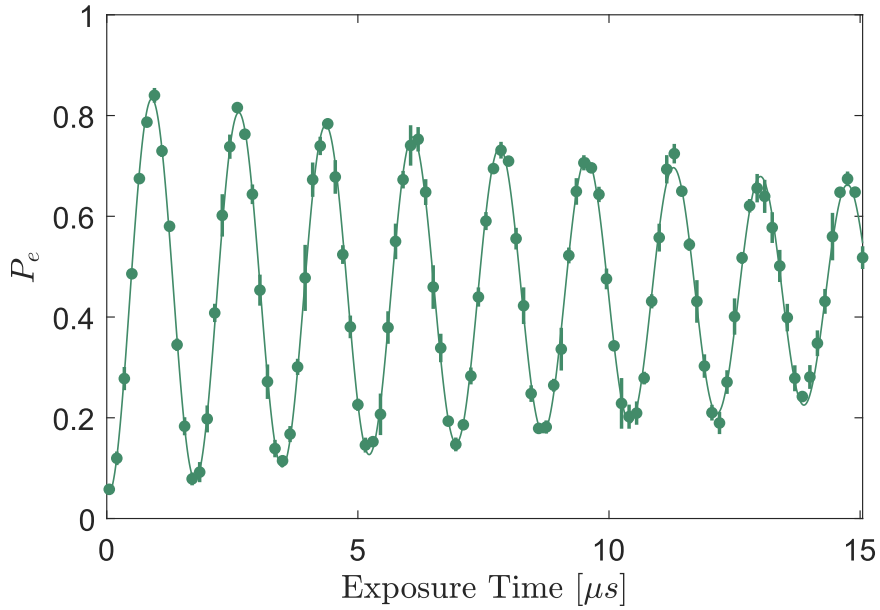

Figure 3.7 : Observed Rabi oscillations of the 58S $^1S_0 - 59S\ ^1S_0$ transition. The excited state probability P_e as a function of microwave exposure time is plotted and fit to a decaying sinusoid of the form $P_e(t) = A\sin(\Omega_R t)\cdot\exp(-t/\tau_{Rabi})$, from which we extract Rabi frequency $\Omega_R = 2\pi\cdot 577.6\text{kHz}$ and decay time $\tau_{Rabi} = 23.7\mu\text{s}$.

$\mathcal{E}$ and then, in turn, interacts with the field, leading to the $\mathcal{E}^2$ (intensity) scaling of the energy shift. Quantum mechanically, the induced dipole moment is a result of the off-diagonal elements of the dipole operator

$$\langle n'l'j'|\hat{\mathbf{d}}|nlj\rangle = -e\,\langle n'l'j'|\hat{\mathbf{r}}|nlj\rangle \tag{3.6}$$

summed over all atomic levels $|n'l'j'\rangle$ when calculating the energy shift via perturbation theory. As mentioned in Chapter 1, strong and fast-scaling polarizability ($\alpha_{nlj} \sim n^7$) is one of the most prominent properties of Rydberg atoms. This is due to closeness between adjacent Rydberg electron orbits, leading to large matrix elements of $\hat{\mathbf{r}}$.

When the transition of interest $nS - nP$ is being (near-)resonantly driven by microwave radiation at frequency ω, as is the case in Rabi method described above, the

same radiation shifts both nS and nP states based on their corresponding polarizability $\alpha_{nS}(\omega)$ and $\alpha_{nP}(\omega)$. Consider that the resultant AC Stark shifts are ΔE_{nS} and ΔE_{nP} respectively, the resonance frequency $\omega_0^{(Rabi)}$ observed via Rabi spectroscopy is actually given by

$$\omega_0^{(Rabi)} = \omega_0 - \Delta E_{nS} + \Delta E_{nP} \tag{3.7}$$

assuming that the atom is initially in state nS. Note that $\omega_0^{(Rabi)}$ is not capable of measuring either the unperturbed resonance frequency ω_0 or the AC Stark shifts on each state ΔE_{nS} and ΔE_{nP}. For measuring these, we will employ the other spectroscopic methods introduced in following sections.

3.1.2 Ramsey sequence

Similar to the Rabi method, Ramsey interferometry also holds historical importance in atomic physics, particularly in precision spectroscopy. The original Ramsey sequence consists of two $\pi/2$ pulses (a quarter period of the Rabi oscillation such as shown in Figure 3.7) separated by a field-free zone of duration T_{Ramsey}. The excited state probability P_e after the second $\pi/2$ pulse, as a function of applied field frequency ω, will form interferometric fringes from which the resonance frequency ω_0 of the transition can be extracted. Because of the typically much longer dark time of T_{Ramsey}, narrower spectral linewidth can be achieved thanks to the longer interrogation time and the absence of the applied field during the dark time, mitigating line broadening due to its intensity inhomogeneities [113].

Another application of the Ramsey sequence comes when the applied frequency is fixed on resonance ($\omega = \omega_0$) while the dark time T_{Ramsey} is being varied. This approach is well known for its usage in measuring the T_2 relaxation time in nuclear

magnetic resonance (NMR) spectroscopy. Here we use this method to measure the unperturbed absolute resonance frequency ω_0 of the Rydberg transitions, the working principle of which is best understood in the picture of the Bloch sphere as shown in Figure 3.8. Considering again the generic Rydberg transition $nS - nP$ with $|nS\rangle$

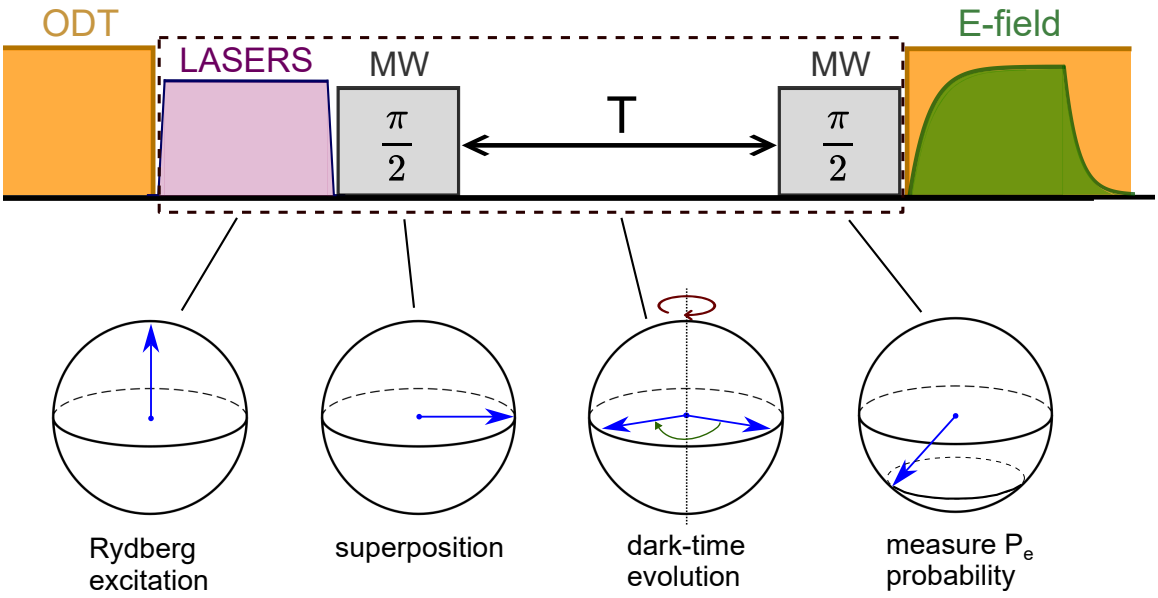

Figure 3.8 : Exposure sequence for the Ramsey interferometry measurements on microwave transitions. The delay time T between the $\pi/2$ pulses is varied to mapped out the precession frequency of the state Bloch vector during the evolution dark-time.

being the initial state, which corresponds to the state vector pointing at the north pole in the Bloch sphere. The first resonant $\pi/2$ pulse brings the atom into an equal superposition of $|nS\rangle$ and $|nP\rangle$ with the state vector lying in the $xy-$plane. Note that the applied field is at the resonance frequency obtained in the Rabi methods $\omega_0^{(Rabi)}$, and this process happens with the Bloch sphere in a rotating frame at frequency that of the applied field $\omega = \omega_0^{(Rabi)}$. Without the dark time, i.e. $T_{Ramsey} = 0$, the second $\pi/2$ pulse would immediately bring the state vector down to the south pole, corresponding to purely the excited state $|nP\rangle$. As T_{Ramsey} increases, the state

vector starts its free precession around the $z-$axis at frequency corresponding to the unperturbed energy difference between $|nS\rangle$ and $|nP\rangle$ in the absence of any AC Stark shifts. If the applied microwave field were present, this energy difference would contain the aforementioned AC Stark shift and be equal to

$$(\Delta E)_{\text{with field}}/\hbar = \omega_0 - \Delta E_{nS} + \Delta E_{nP} = \omega_0^{(Rabi)} \tag{3.8}$$

During the dark time, however, there exists no field that causes AC Stark shifts on either level, the energy difference is therefore unperturbed at $(\Delta E)_{\text{dark}}/\hbar = \omega_0$. In the rotating frame, this results in a precession frequency given by

$$\omega_{Ramsey} = |\omega - \omega_0| \tag{3.9}$$

This precession eventually leads to the sinusoidal oscillation of P_e (projection of state vector on z-axis) as a function of the dark time T_{Ramsey} after the application of the second $\pi/2$ pulse. The oscillation frequency of P_e is given by ω_{Ramsey} and can be much more precisely extracted by fitting the oscillations such as shown in Figure 3.9. Since the applied frequency ω is known, this provides a way of precisely determining the unperturbed transition frequency ω_0.

Note that this method does not demand perfect $\pi/2$ pulses as a detuning from $\omega_0^{(Rabi)}$ or pulse duration different than a quarter cycle will merely results in the state vector pointing out of the $xy-$plane after the first $\pi/2$ pulse. The precession frequency ω_{Ramsey} during the dark time is not affected.

In the experiment, one may repeat the measurement of ω_{Ramsey} with two slightly different applied frequencies ω to confirm the sign of detuning $\omega - \omega_0$. As shown in Figure 3.9 of the Ramsey measurements of P_e in the $(5s59s)\ ^1S_0 - (5s60s)\ ^1S_0$ transition, when the applied microwave frequency was changed from 18505.720MHz to 18505.670MHz, the fitted oscillation frequency increased by 99.73kHz, indicating

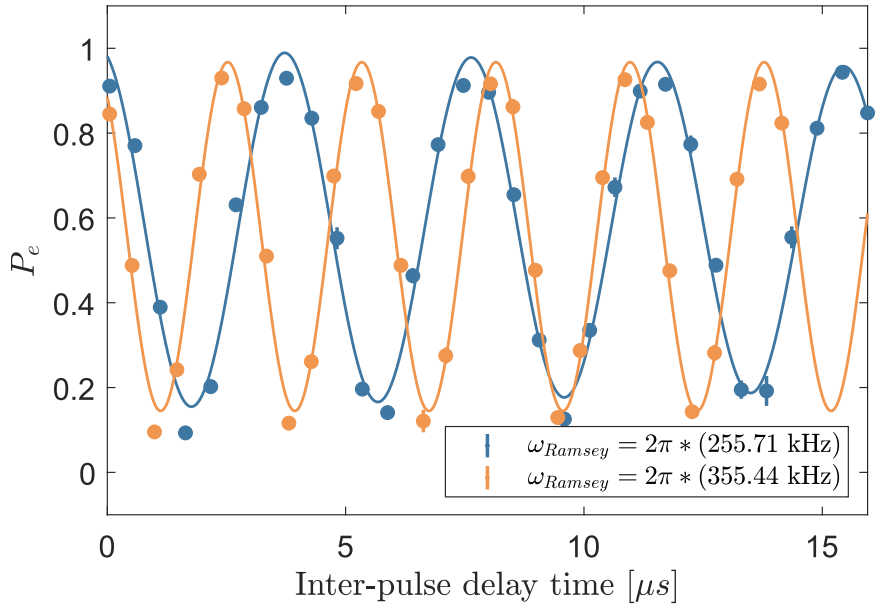

Figure 3.9 : Oscillations of excited state population observed as a function of the inter-pulse delay time T in the $\pi/2 - T - \pi/2$ Ramsey sequence of the $(5s59s)\ ^1S_0 - (5s60s)\ ^1S_0$ transition. As the microwave drive frequency is changed by 50kHz from 18505.720MHz (blue) to 18505.670MHz (orange), we observe an increase of oscillation frequency by 99.73kHz (extracted from the sinusoidal fit shown in solid lines). This indicates that both frequencies are red detuned with respect to the transition. Note that since 59S-60S is a two-photon transition, the actual change of applied frequency is 50kHz*2=100kHz.

that both frequencies are detuned to the blue (higher frequency) side of ω_0, which can be determined as $\omega_0/2\pi = 2 * 18505.720\text{MHz} + 255.71\text{kHz} = 18505.976\text{MHz}$.

3.1.3 Autler-Townes spectrum

Both Rabi spectroscopy and Ramsey interferometry introduced so far have involved exposure sequences of optical Rydberg excitation and the microwave radiations. The optical pulse initializes the atom into the Rydberg state $|nS\rangle$, and the subsequent microwave pulses turn on the coupling Hamiltonian, which drives the $nS - nP$ transition. However, the transition can also be probed in a steady-state approach where

optical and microwave radiations are simultaneously exposed as shown in Figure 3.10. In the presence of the microwave radiation, which is assumed to be near-resonance

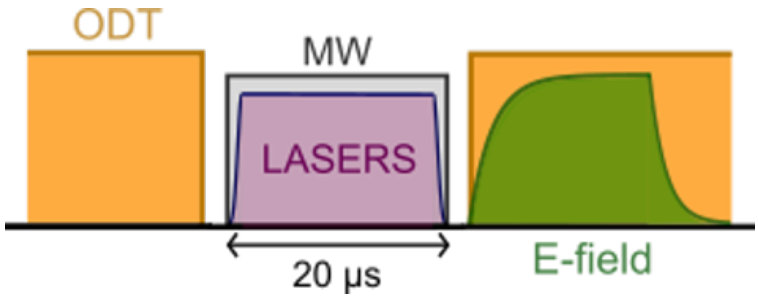

Figure 3.10 : Co-exposure sequence used for Autler-Townes spectra measurements. The excitation lasers probe the Rydberg states which are dressed by the microwave fields. Typical exposure time is $\sim 20\mu$s.

($\omega \approx \omega_0$), the total Hamiltonian of the system can be written in matrix form as

$$\hat{H} = \frac{\hbar}{2}\begin{pmatrix} \delta & \omega_r \\ \omega_r & -\delta \end{pmatrix} \tag{3.10}$$

in an rotating frame. Here $\delta = \omega - \omega_0$ is the detuning, and the Rabi frequency ω_r characterizes the strength of the microwave-induced coupling. This new Hamiltonian can now be diagonalized to yield a new pair of eigen-states $|+\rangle$ and $|-\rangle$, both of which are superposition of $|nS\rangle$ and $|nP\rangle$ as shown in Figure 3.11, and they have respective eigen-energies given by

$$E_\pm = \frac{\hbar}{2}(-\delta \pm \Omega_R) \tag{3.11}$$

where $\Omega_R = \sqrt{\omega_r^2 + \delta^2}$. In other words, the near-resonant microwave field dresses the original two-level ($|nS\rangle$ and $|nP\rangle$) atom into the new eigen-states $|\pm\rangle$. This splitting is know as the Autler-Townes (AT) effect, and the dressed states $|\pm\rangle$ are now the target states of the laser driven Rydberg excitation.

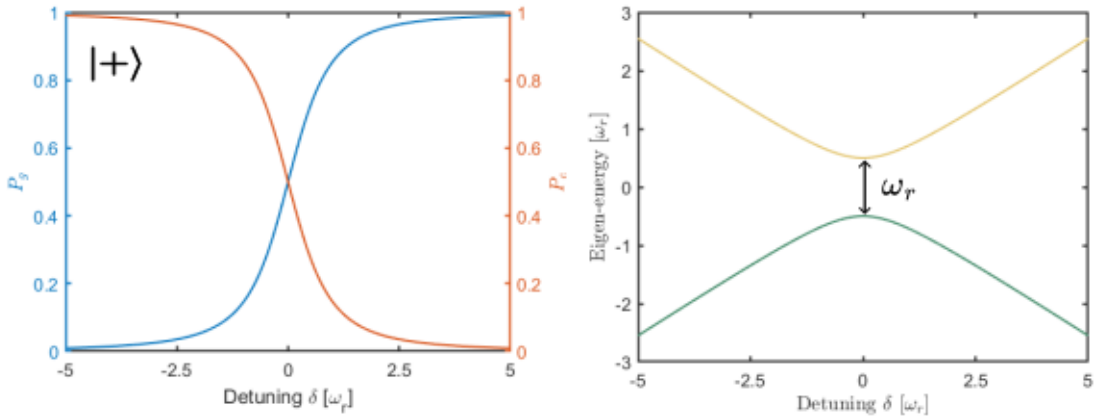

Figure 3.11 : Left: Composition of the dressed state $|+\rangle$ in terms of the probability P_g and P_e in the bare ground and excited Rydberg states. The composition of the lower $|-\rangle$ is an exact opposite of $|+\rangle$. Right: Eigen-energies of the two dressed states as a function of δ. At resonance ($\delta = 0$), the energy splitting is equal to ω_r.

Assuming that the laser frequency is tuned near resonance of two-photon Rydberg transition, i.e. $\hbar\omega_{laser} \approx E_{nS}$, where the term energy E_{nS} of the Rydberg state $|nS\rangle$ is referenced to the strontium ground state $|g\rangle \rightarrow (5s^2)\,{}^1S_0$. In a rotating frame at the laser frequency ω_{laser}, the transition Hamiltonian induced by the lasers can be written as

$$\hat{H}_{laser} = \frac{\hbar\Omega_{Ryd}}{2} |g\rangle \langle nS| e^{i\Delta_{nS}t} + h.c. \tag{3.12}$$

where $\Delta_{nS} = \omega_{laser} - E_{nS}/\hbar$ is the laser detuning from the bare Rydberg level $|nS\rangle$. As mentioned in Section 2.3, the effective two-photon Rabi frequency Ω_{Ryd} of the laser excitation is typically on the order of $\Omega_{Ryd}/2\pi \lesssim 1$ Hz, much smaller than microwave coupling ω_r, allowing us to treat it perturbatively. The theoretical Rydberg excitation rate, as a function of laser detuning Δ_{nS}, is therefore given by Fermi's golden rule as

$$\Gamma(\Delta_{nS}) = \frac{2\pi}{\hbar} \sum_f |\langle f|\hat{H}_{laser}|i\rangle|^2 \rho(\Delta_{nS} - E_f/\hbar) \tag{3.13}$$

where the initial state is the ground state $|g\rangle$, and the final states here are the microwave dressed eigen-states $|\pm\rangle$, hence the final energies are E_+ and E_-. The density of states therefore becomes $\rho(\Delta_{nS} - E_f/\hbar) = [\Delta_{nS} - \delta(E_+)/\hbar + \Delta_{nS} - \delta(E_-)/\hbar]/2$, as a result, $\Gamma(\Delta_{nS})$ can be rewritten as

$$\Gamma(\Delta_{nS}) \propto |\langle +|nS\rangle|^2 \, \delta(\Delta_{nS} - E_+/\hbar) + |\langle -|nS\rangle|^2 \, \delta(\Delta_{nS} - E_-/\hbar) \tag{3.14}$$

In other words, when the laser frequency is scanned around the resonance of $|nS\rangle$, the excitation spectrum consists of two peaks at detuning corresponding to the eigen-energies of $|\pm\rangle$, and the height of the peaks represents the overlap between $|\pm\rangle$ and $|nS\rangle$. Since both $E_\pm$ and state composition of $|\pm\rangle$ can be exactly calculated as shown by Eqn. 3.11 and Figure 3.11, given a measured excitation spectrum $\Gamma(\Delta_{nS})$, one can figure out the microwave detuning δ and subsequently adjust ω accordingly. When the microwave is resonant $\delta = 0$, the dressed states $|\pm\rangle$ become equal superpositions of $|nS\rangle$ and $|nP\rangle$, meaning $|\langle +|nS\rangle|^2 = |\langle -|nS\rangle|^2$, and the excitation spectrum becomes two peaks at the same height separated by $E_+ - E_- = \hbar\Omega_R$. This makes the AT spectrum a single measurement that accurately reveals both microwave resonance frequency ω_0 and the coupling Rabi frequency Ω_R.

Note that, since the Rydberg excitation happens in the presence of the microwave fields, the AT spectrum is also sensitive to AC Stark shift. When the two peaks are balanced, it indicates that the applied microwave frequency is resonantly connecting $|nS\rangle$ and $|nP\rangle$ after accounting for the AC Stark shift they experience. In other words,

$$\omega_0^{(AT)} = \omega_0 - \Delta E_{nS} + \Delta E_{nP} = \omega_0^{(Rabi)} \tag{3.15}$$

same as the resonance frequency obtained in Rabi methods. In addition, the dressed states are still located symmetrically in energy but instead about the AC Stark shifted

$|nS\rangle$. This effect can be captured by rewriting the energy conservation delta function as $\delta(\Delta_{nS} - \Delta E_{nS}/\hbar - E_{\pm}/\hbar)$. As shown by the example in Figure 3.12, compared to the excitation of the bare atomic line (in absence of microwave field) of $61s(^3S_1)$ state, the AT spectrum of the $61s\ (^3S_1) - 62s\ (^3S_1)$ transition undergoes a shift of ΔE_{nS} and splitting of Ω_R, therefore ΔE_{nS} can be extracted from the separation between the bare atomic state $|61S\rangle$ and the center of the AT peaks.

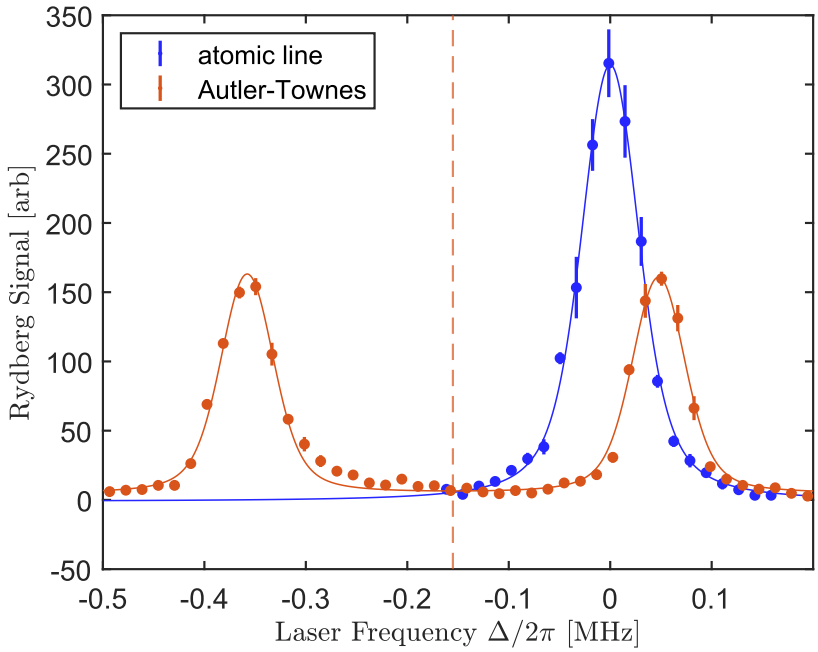

Figure 3.12 : Measured Autler-Townes spectrum of the $5s61s\ ^3S_1 - 5s62s\ ^3S_1$ transition obtained by scanning the frequency $\Delta/2\pi$ of the Rydberg excitation lasers around the atomic resonance of $5s61s\ ^3S_1$. Compared to the bare (without microwave) atomic line plotted in blue, the relative shift of the center of AT splitting (red dashed line) gives the AC Stark shift $5s61s\ ^3S_1$ experiences due to the applied microwave field.

In summary, we use the AT spectrum for tuning the microwave frequency on resonance ($\omega = \omega_0^{(AT)} = \omega_0^{(Rabi)}$) with AC Stark shifted Rydberg transitions as well as definitively characterizing size of the shift and the Rabi splitting Ω_R under resonance condition. Compared to Rabi and Ramsey methods, the AT spectrum measurement

does not require SFI resolvability of involved Rydberg states since the dressed states $|\pm\rangle$ themselves are superposition of the bare Rydberg states. Instead the entire SFI spectrum is summed over to give the total Rydberg excitation rate. That being said, however, in case when the states involved are SFI-resolvable, it can still be informative to inspect the composition of the observed AT peaks through their SFI distribution. This will be demonstrated in Chapter 4 in visualizing the topologically protected edge states via steady state wave-function.

Since the AT spectra here are obtained via optical excitation as a probe of the microwave coupled Rydberg states, it can only be used to measure the AC Stark shift on states that are optically accessible, which are nS (or nD) states per our two-photon Rydberg excitation scheme. In addition, the spectral resolution is determined by the laser linewidth, which limits the minimum Rabi frequency Ω_R that can be extracted from the splitting.

3.2 Transition characterization results

Based on the three spectroscopic methods introduced above, results of some measured quantities of a wide range of Rydberg states and microwave transitions will be listed in this section. A substantial part of the following measurements will be used as guidance for designing synthetic dimension experiments including the results presented in Chapter 4 as well as future related experiments.

3.2.1 Unperturbed resonant frequency

Here we used Ramsey interferometry to measure the absolute energy difference between two Rydberg levels. Following the protocol described in Section 3.1.2, the resonance frequency $\omega_0^{(Rabi)}$ in the presence of the microwave driving field is measured

first using Rabi spectroscopy, from which the Rabi frequency ω_r is extracted to determine roughly the microwave pulse duration needed to generate a $\pi/2$ pulse at given source power. The $\pi/2 - T - \pi/2$ Ramsey sequence is then carried out, with the microwave frequency set to $\omega = \omega_0^{(Rabi)}$, to measure the dark-time evolution frequency $|\omega - \omega_0| = |\omega_0^{(Rabi)} - \omega_0|$ via the oscillation frequency ω_{Ramsey} of the final Rydberg state population at a function of dark time T. For typical microwave power used here (with Rabi frequency $\omega_r/2\pi \approx 100\text{kHz} - 1\text{MHz}$), the size of the net AC Stark shift $(-\Delta E_{nS} + \Delta E_{nP})$ of the transition generally also falls in this range, which rendered the population fringes easily observable. Certain transitions, however, may experience net shift as low as $\lesssim 10$kHz, resulting in fringe separations of $\gtrsim 100\mu$s, which can be difficult to measure reliably with available sample coherence time (see Section 3.2.4). In such cases, the applied microwave frequency ω is usually intentionally detuned from $\omega_0^{(Rabi)}$ to increase the dark-time precession frequency $|\omega - \omega_0|$.

Systematic measurements of the unperturbed frequencies are performed in the range of $50 \lesssim n \lesssim 70$ for the following transitions within the singlet Rydberg series: $5sns\,(^1S_0) - 5s(n+1)s\,(^1S_0)$, $5sns\,(^1S_0) - 5snd\,(^1D_2)$, $5sns\,(^1S_0) - 5snp\,(^1P_1)$ and $5snd\,(^1D_2) - 5s(n-3)f\,(^1F_3)$, among which $nS - (n+1)S$ and $nS - nD$ are both two-photon microwave transitions. Measured results of unperturbed frequencies are listed in Table 3.1 for some selected transitions. These values are then fed into Equation 3.1 for the relative energy between Rydberg levels $|nlj\rangle$ and $|n'l'j'\rangle$

$$\Delta E_{n',l',n,l} = -\frac{\text{Ry}_{84}}{[n' - \delta(n', l')]^2} + \frac{\text{Ry}_{84}}{[n - \delta(n, l)]^2} \tag{3.16}$$

The quantum defects are assumed to be described by the Rydberg-Ritz expression

$$\delta(n, l) = \delta_0(l) + \frac{\delta_2(l)}{[n - \delta_0(l)]^2} + \frac{\delta_4(l)}{[n - \delta_0(l)]^4} \tag{3.17}$$

where δ_0, δ_2 and δ_4 are constant parameters, and an updated set of values for them are

Rydberg transitions	Measured Frequencies (MHz)	Deviation (MHz)
57S-58S	41259.930	0.002
58S-59S	39058.900	0.009
58S-58P	21317.747	-0.005
59S-59P	20193.775	0.005
60S-60P	19147.501	-0.002
57S-57D	37248.428	-0.037
58S-58D	35240.910	0.020
66D-63F	18571.873	-0.001
67D-64F	17711.111	-0.015

Table 3.1 : Measured unperturbed resonance frequencies (energy difference) for representative $5sns\,(^1S_0) - 5s(n+1)s\,(^1S_0)$, $5sns\,(^1S_0) - 5snd\,(^1D_2)$, $5sns\,(^1S_0) - 5snp\,(^1P_1)$ and $5snd\,(^1D_2) - 5s(n-3)f\ (^1F_3)$ transitions in the singlet Rydberg series. These measured frequencies are used to obtained a new set of quantum defect δ values shown in Table 3.2, which produces updated predictions for the transition frequencies and is found to deviate very little from the measured results, demonstrating the low scatter of the measurements. More data can be found in Ref.[7].

Rydberg states	δ_0	δ_2	δ_4
$^1S_0$	3.2688559	-0.0879	-3.36
$^1P_1$	2.7314851	-5.1501	-140.1
$^1D_2$	2.3821857	-40.5009	-878.6
$^1F_3$	0.0873868	-1.5446	7.56

Table 3.2 : Updated quantum defect parameters extracted from the measured unperturbed transition frequencies. More data can be found in Ref.[7].

extracted by fitting the $\Delta E_{n',l',n,l}$ data. The results are shown in Table 3.2, and the updated values of $\delta(n,l)$ are then used to calculate new predicted energy differences, which are compared to the measured results. The deviations, as listed in Table 3.1, are on the order of $\lesssim$ 50kHz. This provides excellent guidance for narrowing down frequency search range when looking for new microwave transitions.

Other than easing the effort of finding new transitions, the measurement of unperturbed frequencies is central to the synthetic dimension experiments, hence details regarding the data analysis extracting the quantum defects $\delta(n,l)$ and comparison with previously reported values for strontium will not be discussed here. They can be found in this published paper [7].

It should be noted that the transition resonance frequencies measured via the Ramsey interferometry sequence is only unperturbed by the optical and microwave radiations that we may actively apply. Uncontrolled stray fields, however, can still cause a nonzero net AC Stark shift on the transitions. For the published results in [7], stray electric field was measured and canceled by applying offset potentials on the ionizing electrode plates down to an estimated amplitude of $\lesssim$ 5 mV/cm.

3.2.2 Rabi frequency

As introduced in Chapter 1, in Rydberg synthetic dimensions, microwave driven transitions between Rydberg levels mimic particle hopping between lattice sites. It is therefore essential to characterize the Rabi frequencies, which determine the transitions rates. Here we show Rabi frequencies obtained using the Rabi oscillation measurements, where the Rabi frequency is given by the observed oscillation frequencies $\Omega_R/2\pi$. This study is aimed to, on a broad scheme in our apparatus, characterize the available microwave coupling strength across different quantum number n and types of transitions, and we will therefore assume the resonance condition that $\omega \approxeq \omega_0^{(Rabi)}$ and $\Omega_R = \omega_r$.

Table 3.3 lists measured results of Ω_R for some representative $5sns\,(^1S_0) - 5s(n+1)s\,(^1P_1)$ transitions in the range of $n \approx 50 - 70$. All transitions studied here are measured using the mixer setup as shown in Figure 2.23 for consistency. The microwave source power (attenuation) is adjusted for each transition such that such that the population oscillation frequency is in a range convenient to measure $\Omega_R/2\pi \sim$ 100kHz$-$1MHz. Based on the source power and the observed Ω_R, we can calculate the maximum available Rabi frequency Ω_{max} associated with each transition. Since the source power is configured in terms of attenuation by decibels (dB), which relates to the microwave field intensity as

$$\text{Attn} = 10\log_{10}(\frac{I}{I_{max}})\ \text{dB} \tag{3.18}$$

or equivalently

$$I_{max} = I \cdot 10^{Attn/10} \tag{3.19}$$

For single photon transitions ($S - P$), the Rabi frequency is proportional to electric

Transitions	$\omega_0^{(Rabi)}$ (MHz)	Attenuation (dB)	Ω_R (kHz)	$\Omega_R^{(max)}$ (MHz)
58S-58P	21317.69	48	577	144.9
57S-57P	22526.81	35	572	32.2
56S-56P	23828.83	30	787	24.9
55S-55P	25233.6	30	721	22.8
54S-54P	26751	15	940	5.3
53S-53P	28392.28	31	888	31.5
52S-52P	30171.16	20	854	8.5
51S-51P	32101.1	15	852	4.8
47S-47P	41708.24	9	693	N/A
46S-46P	44696.8	9	775	N/A

Table 3.3 : Rabi frequencies Ω_R measured for selected $5sns\,(^1S_0) - 5snp\,(^1P_1)$ transitions. Different attenuation is applied to the microwave source power when driving different transitions such that the resultant Ω_R is similar. The attenuation shown here is referenced to the maximum source power (at around +15 dBm neglecting frequency dependence). A magnetic field of $\sim$ 6Gauss is applied to selectively drive the transitions to the $m = +1$ sublevel of the $^1P_1$ state. All transitions shown here are measured with the mixer setup generating the drive frequencies except for 47S-47P and 46S-46P which use frequency doubler.

field amplitude, which is square root of intensity, therefore

$$\Omega_R^{(max)} = \Omega_R \cdot 10^{Attn/20} \quad \text{(single photon)} \tag{3.20}$$

The values of $\Omega_R^{(max)}$ are calculated as an indicator of the inherent strength of the transitions. It should be noted that this method of estimating $\Omega_R^{(max)}$ is only valid when the final output microwave intensity scales linearly with the source power, which is the case for the mixer and combiner setup, but not for the frequency multiplier based setup described in Section 2.4. Moreover, other minor variations such as the frequency dependent loss in the mixing or combining processes are also ignored.

For two photon transitions (such as $S-S$), however, the effective Rabi frequency can be generally approximated to be proportional to the field intensity, and we have

$$\Omega_R^{(max)} = \Omega_R \cdot 10^{Attn/10} \quad \text{(two photon)} \tag{3.21}$$

Table 3.4 shows another set of measurements of $\Omega_R^{(max)}$ focusing on $5sns\,^3S_1 - 5s(n+1)s\,^3S_1$ transitions around $n \sim 60$, which are used to construct synthetic dimension experiments, for reasons to be discussed in Chapter 4.

In both cases of $nS-nP$ and $nS-(n+1)S$ transitions, the maximum Rabi frequencies $\Omega_R^{(max)}$ display strong and irregular n dependence. The transition dipole matrix element is expected to vary smoothly as $\sim n^3$, implying that the microwave driving field experiences frequency-dependent attenuation. This is likely caused by interference patterns built up during its propagation from the horn antenna to the atoms, the path of which involves passing through a small aperture (1.5") into the vacuum chamber and reflections off metallic surfaces. Other factors affecting the final microwave field intensity include the bandwidth of the horn antenna and the cut-off frequency set by the vacuum window.

Transitions	$\omega_0^{(Rabi)}$ (MHz)	Attenuation (dB)	Ω_R (kHz)	$\Omega_R^{(max)}$ (MHz)
65S-66S	13719.685	0	74	0.07
64S-65S	14403.88	15	1781	56.3
63S-64S	15135.12	13	1063	21.2
62S-63S	15915.9	12	485	7.69
61S-62S	16751.72	15	578	18.3
60S-61S	17646.35	0	964	0.96
59S-60S	18606.78	7	318	1.59
58S-59S	19638.4	10	416	4.16
57S-58S	20747.33	0	512	0.51
56S-57S	21941.06	0	176	0.18

Table 3.4 : Rabi frequencies Ω_R measured for selected $5sns\ (^3S_1) - 5s(n+1)s\ (^3S_1)$ transitions. Different attenuation is applied to the microwave source power when driving different transitions such that the resultant Ω_R is similar. The attenuation shown here is referenced to the maximum source power (at around +15 dBm neglecting frequency dependence). A magnetic field of ~ 6 Gauss is applied to selectively drive the transitions to the $m = +1$ sublevel of the $^1P_1$ state. All transitions shown here are measured with the mixer setup generating the drive frequencies.

The maximum Rabi frequencies $\Omega_R^{(max)}$ limits the available tunneling rates one can configure between lattice sites when constructing Rydberg synthetic dimensions. For the $5sns\,^3S_1 - 5s(n+1)s\,^3S_1$ transitions, in order to achieve sizable tunneling rates ($\gtrsim$ 500kHz) without moving to an entirely different frequency band, we chose to work with states $58 \leq n \leq 64$.

3.2.3 AC Stark shift

While the resonance frequency $\omega_1^{(Rabi)}$ of a transition, say $|r_1\rangle \rightarrow |r_2\rangle$, under the influence of AC Stark shift can be confirmed by the Autler-Townes splitting spectrum, introducing a second frequency $\omega_2^{(Rabi)}$ to resonantly drives another transition, say $|r_2\rangle \rightarrow |r_3\rangle$, will cause additional shifts on $|r_1\rangle$ and $|r_2\rangle$ such that $\omega_1^{(Rabi)}$ is no longer resonant. Similarly, $\omega_2^{(Rabi)}$ will cease to be on resonance with $|r_2\rangle \rightarrow |r_3\rangle$ due to the presence of $\omega_1^{(Rabi)}$. As synthetic dimension experiments can consists of many such connecting transitions, characterization of their ac Stark shifts is vital for tuning all the applied frequencies to be resonant.

The results of AC Stark shift measurements presented here will again be focused on $5sns\,^3S_1 - 5s(n+1)s\,^3S_1$ transitions, main ingredients of our synthetic dimension experiments. Thanks to the $S-$states being directly accessible through our optical Rydberg excitation, measuring the AC Stark shift is straightforward as in the example of $58S - 59S$ transition shown above. The AC Stark shift on $|58S\rangle$ is given by the displacement between its bare atomic resonance and the center of the AT splitting as illustrated in Figure 3.12. The same comparison is then with the excitation laser frequencies tuned around that of $|59S\rangle$. The results are listed in Table 3.5 with the shaded cells along the diagonal representing states that are directly connected by the inspected transitions (such as $58S$ and $59S$ by the transition $58S - 59S$). Here the

shift (kHz)	58S-59S	59S-60S	60S-61S	61S-62S	62S-63S
Δ(58S)	-164	-172	-90	-10	-40
Δ(59S)	-14	+334	-114	-16	-18
Δ(60S)	-70	-538	+140	-78	-26
Δ(61S)	-26	-122	-380	-154	-68
Δ(62S)	-16	-46	-72	-44	-78
Δ(63S)	-6	-20	-26	-76	-138

Table 3.5 : Measurements of AC Stark shifts experienced by each $5sns\ ^3S_1$ Rydberg states as caused by each $nS-(n+1)S$ transition. The microwave frequencies driving transitions shown here are generated using the combiner setup, and their source power set to produce a Rabi frequency of 400kHz. A magnetic field of ~ 6 Gauss is applied to selectively drive the transitions between $m = +1$ sublevels of both nS and $(n+1)S$ states.

AC Stark shifts are measured with each transition's corresponding microwave source power set to produce a roughly equal Rabi frequency at about 400kHz to emphasize the variation with quantum number. The non-shaded region of the table, which indicates states not directly connected by respective transitions, are simply measured by the shift of Rydberg atomic resonance position in the presence of respective microwave fields. Figure 3.13 shows the example of the excitation spectra of $62S$ state with and without the microwave field that resonantly drives the $58S - 59S$ transition. An AC Stark shift of 50kHz is observed as the displacement of the excitation resonance.

Since the AC Stark shift is a result of the Rydberg atom being polarized by the microwave radiations via off-resonant coupling to other Rydberg levels, we expect the size of the shift to generally follow the same n^7 scaling as the polarizability $\alpha_{nlj}(\omega)$. However, the measured results in Table 3.5 clearly display an irregular n-dependence

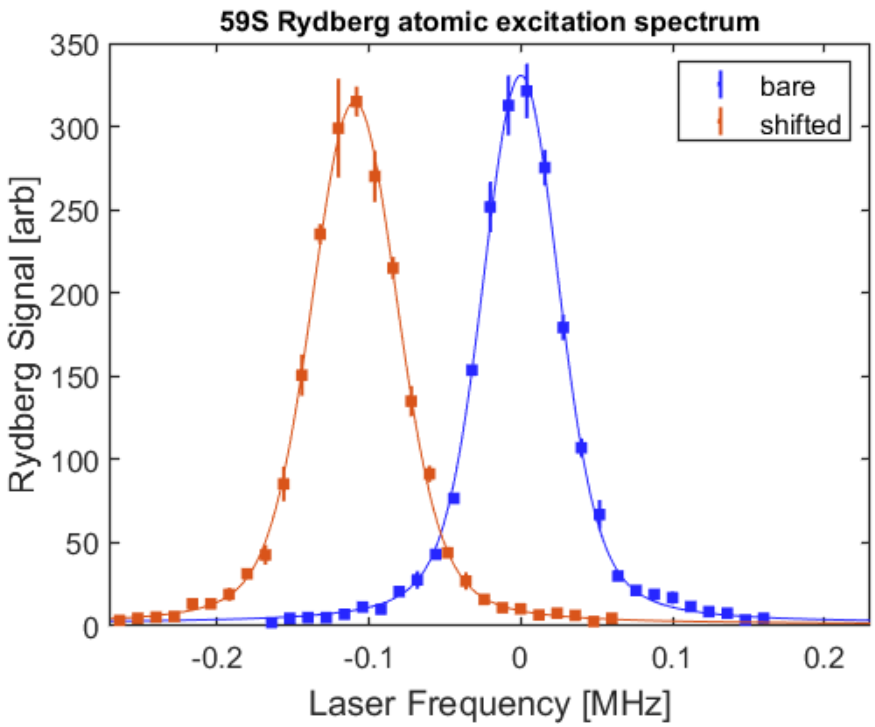

Figure 3.13 : Rydberg excitation spectrum of the bare (blue) $(5s59s)\ ^3S_1$ atomic state compared to in the presence of microwave field (red) that resonantly drives the $(5s60s)\ ^3S_1 - (5s61s)\ ^3S_1$ transition. The AC Stark shift of the $(5s59s)\ ^3S_1$ state is obtained from of the relative shift of the atomic resonance position.

with particularly large shifts for the $59S - 60S$ and $60S - 61S$ transitions. Similar to the variations of the maximum Rabi frequency shown above, this may be caused by microwave fields interference around the vacuum chamber, resulting in anomalously strong off-resonant coupling to some states.

3.2.4 Coherence time

Coherence is a critical property in quantum systems as it characterizes how well a system can maintain its quantum state under the influence of environmental perturbations. In the context of quantum simulation particularly, it determines how closely

the behavior of the experimental systems reproduce that of the Hamiltonian of interest. The coherence of a quantum system can be inspected in space, time or otherwise defined representations. Here we are interested in the temporal coherence of our microwave transitions and will discuss its implications on our choice of transitions for constructing Rydberg synthetic dimension experiments.

As will be described in details in Chapter 4, we want to measure the state dynamics under the Hamiltonian that we construct using the microwave Rydberg transitions. This calls for the desired dynamics to survive the coherence time scale τ_{coh} of the system in the presence of the Hamiltonian, which is defined only when the microwave fields are on. Therefore τ_{coh} is a collective result of the individual coherence time of all the involved transitions, which can be characterized by the decay time τ_{Rabi} of the Rabi oscillations. While exact prediction of the total effective coherence time as a result of the interplay between individual transitions requires setting up and solving complex master equations and can still vary with apparatuses and Hamiltonian of interest, in this section we will simply present measurements on selected transitions and qualitatively inspect dependence on different parameters.

In addition to τ_{Rabi} of Rabi oscillations, the coherence time associated with the Ramsey oscillations such as shown in Figure 3.9 can also provide useful information about the decoherence of superposition states in the dark time. Similar to τ_{Rabi}, we extract τ_{Ramsey} by fitting the probability oscillations with an exponentially decaying amplitude. While the current synthetic dimension experiment does not involve dark-time evolution, we are showing results of τ_{Ramsey} of selected transitions for future references.

Table 3.6 lists measurements of τ_{Rabi} and τ_{Ramsey} of several $5sns\,(^1S_0) - 5snp\,(^1P_1)$ transitions observed at similar Rabi frequencies Ω_R. These are the same transitions

Transitions	Ω_R^{max} (MHz)	Ω_R (kHz)	τ_{Rabi} (μs)	τ_{Rmsey} (μs)
58S-58P	144.9	577	22.0	40.3
57S-57P	32.2	572	39.1	38.2
56S-56P	24.9	787	29.2	36.6
55S-55P	22.8	721	10.2	47.3
54S-54P	5.3	940	6.4	7.0
53S-53P	31.5	888	34.3	39.5
52S-52P	8.5	854	9.5	57.3
51S-51P	4.8	852	22.1	41.6

Table 3.6 : Measurements of coherence times τ_{Rabi} and τ_{Ramsey} of the Rabi and Ramsey oscillations respectively. The transitions inspected here are the same selected $5sns\,(^1S_0) - 5snp\,(^1P_1)$ transitions as in Table 3.3, and the Rabi frequencies Ω_R and Ω_R^{max} are also shown. The attenuation shown here is referenced to the maximum source power (at around +15 dBm neglecting frequency dependence). A magnetic field of $\sim$ 6 Gauss is applied to selectively drive the transitions to the $m = +1$ sublevel of the $^1P_1$ state. All transitions shown here are measured with the mixer setup generating the drive frequencies.

as in the maximum Rabi frequency characterization in Table 3.3, and there is, again, a large and irregular n-dependence of both τ_{Rabi} and τ_{Ramsey}. Upon close inspection, it can be noticed that the coherence times are, to certain extent, correlated with the maximum Rabi frequency $\Omega_R^{(max)}$ in that lower $\Omega_R^{(max)}$ leads to shorter coherence times. As discussed before, $\Omega_R^{(max)}$ characterizes the inherent strength of a transition

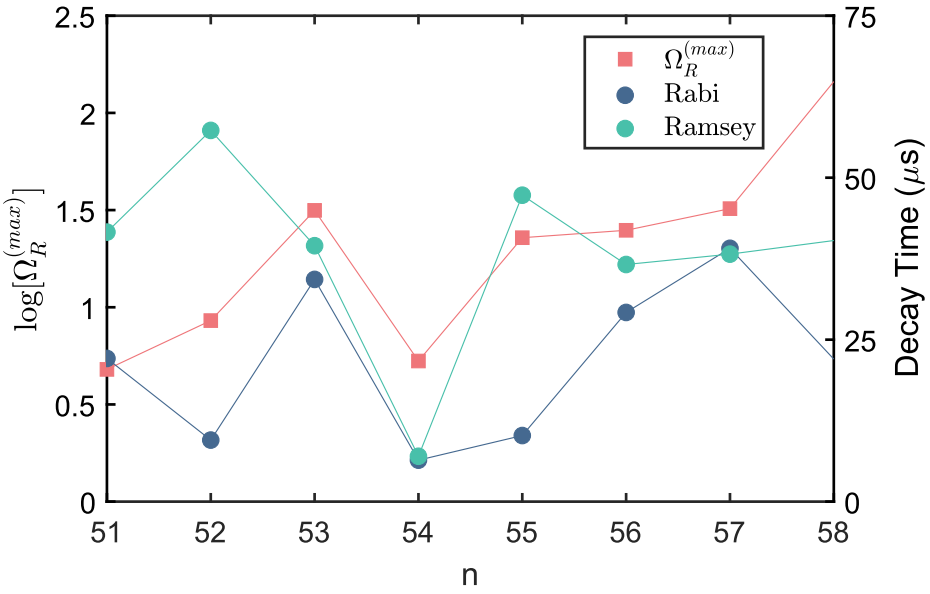

Figure 3.14 : Measured Rabi and Ramsey decay times τ_{Rabi} and τ_{Ramsey} of $5sns(^1S_0)-5snp(^1P_1)$ transitions plotted together with the logarithm of maximum Rabi frequency $\Omega_R^{(max)}$ associated with each transition as measured in Table 3.3.

resulting from the dipole matrix elements, which varies smoothly with n, and the microwave environment of the apparatus. Therefore, a low $\Omega_R^{(max)}$, such as for the $54S-54P$ transition, may indicate a destructive interference at the frequency (or polarization) for the transition of interest, and requires more microwave source power to achieve the same Rabi frequency. However, doing so can enhance other frequency (or polarization) components and results in stronger off-resonant couplings to other states, which get mixed in the dynamics and leads to degraded coherence time. The

similar process may also result in anomalously large AC Stark shift.

A fundamental limit of individual transition decay time is set by the lifetime of the involved states, which is primarily determined by two processes: radiative decay and black-body radiation (BBR) induced transitions [11]. Lifetime of a Rydberg states resulting from both these two processes can be estimated via their respective scaling $\tau_{nat} \propto n^3$, $\tau_{BBR} \propto n^2$ and previously measured values in [2]. The calculated lifetimes

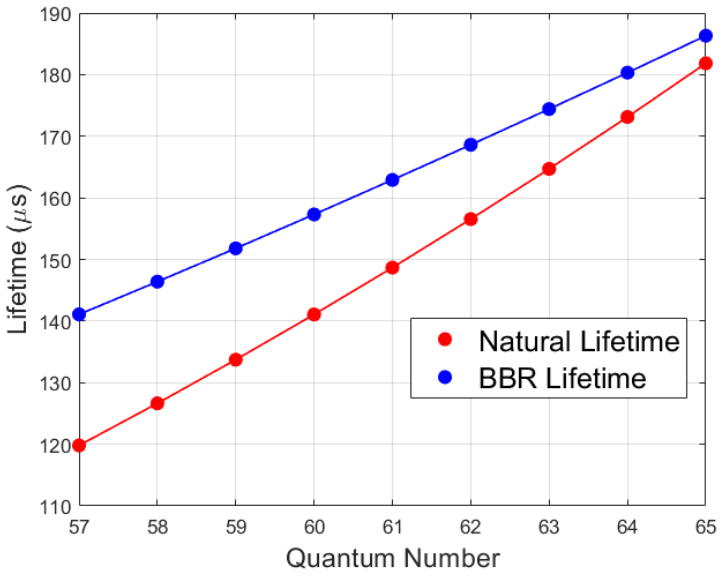

Figure 3.15 : Natural radiative decay lifetime and blackbody induced transition lifetime of $5sns\ ^3S_1$ states estimated by scaling from previous results [2].

are plotted in Figure 3.15 for $5sns\ ^3S_1$ around $n = 60$. The positive n-scaling of lifetimes also provides an incentive to explore transitions at high quantum numbers in the future.

Chapter 4

SSH model with Rydberg synthetic dimensions

The main results of our Rydberg-atom synthetic dimension experiments center around the realization and characterizations of the Su-Schieffer-Heeger (SSH) model. The SSH model, as mentioned in 1.2, is of paradigmatic importance in the studies of topological physics in that it is one of the simplest systems that exhibit topological character. For this reason, the SSH model has seen numerous studies using synthetic dimensions platforms including photonic states, momentum states, magnetic levels, floquet systems and more recently Rydberg atomic states in our lab. Before getting dazzled by the rich topological characteristics of the SSH model and its variants as are explored by these experimental techniques, we will briefly introduce the origin of the SSH model and discuss some of its most well-known topological features.

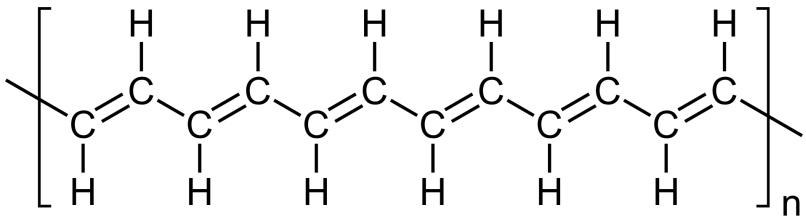

Figure 4.1 : Chemical structure of the trans-polyacetylene polymer molecule. The chain of carbon atoms are connected by alternating single/double bonds.

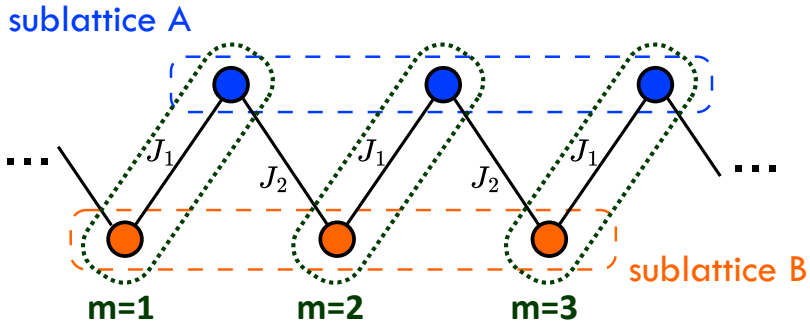

Figure 4.2 : Structural diagram of the SSH model abstracted from the chemical structure in Figure 4.1. Adjacent lattice sites are connected by alternating tunneling rates J_1, J_2. The lattice sites may be categorized into two sublattices A and B such that J_1 and J_2 represent, respectively, tunnelings within and between unit cells, which may be numbered by m.

4.1 The Su-Schrieffer-Heeger model

The now famous Su-Schrieffer-Heeger (SSH) model was originally proposed in 1979 [114] to account for the drastic increase of electrical conductivity in the trans-polyacetylene polymer when doped [115, 116]. This polymer chain has a molecular structure consisting of the repeating unit $[C_2H_2]_n$ as shown in Figure 4.1. The carbon atoms are connected to form a 1D chain with single-double-bond alternating pattern. This structure, after taking the tight-binding approximation, boils down to a 1D lattice-type model as shown in Figure 4.2. The lattice consists of two-site unit cells which are indexed by m, and the intra- and inter-cell tunneling rates J_1 and J_2 form a staggered pattern that represent the alternating bond strength in the polyacetylene. In addition, we may also define two sublattices A and B, and with the sites assignments as shown in Figure 4.2, tunneling only exists between sublattices but not within either A or B. This bipartite structure is what makes the SSH model a chiral symmetric system [117].

4.1.1 Band structure

To calculate the band structure of the SSH model, we will solve for the dispersion relation for the bulk of the system by considering a finite lattice with periodic boundary condition. The derivation in this section largely follows that presented in Ref.[118]. The model Hamiltonian can be written as

$$\hat{H} = J_1 \sum_{m=1}^{N} (|m, B\rangle \langle m, A| + h.c.) + J_2 \sum_{m=1}^{N} (|m+1, A\rangle \langle m, B| + h.c.) \tag{4.1}$$

where N is the total number of unit cells, and the wavefunction is characterized by the electron being in the m-th unit cell and A/B sublattice. In other words, the wavefunction can be separated into the internal and external (with respect to unit cells) parts of the Hilbert space as $|m, A/B\rangle = |m\rangle \otimes |A/B\rangle$ where we may further Fourier transform the external part $|m\rangle$ into the Bloch states

$$|m\rangle = \frac{1}{\sqrt{N}} \sum_{k} e^{ikm} |k\rangle \tag{4.2}$$

Re-writing the bras and kets in the Hamiltonian and separating the internal and external parts again leads to

$$\hat{H} = \sum_{k} [(J_1 + e^{-ik} J_2) |k, B\rangle \langle k, A| + (J_1 + e^{ik} J_2) |k, A\rangle \langle k, B|] \tag{4.3}$$

$$= |k\rangle \langle k| \otimes [(J_1 + e^{ik} J_2) |A\rangle \langle B| + (J_1 + e^{-ik} J_2) |B\rangle \langle A|] \tag{4.4}$$

from which we can extract a block diagnolized form of the Hamiltonian

$$\hat{H}(k) = \begin{pmatrix} 0 & J_1 + e^{ik} J_2 \\ J_1 + e^{-ik} J_2 & 0 \end{pmatrix} \tag{4.5}$$

with the entire Hamiltonian now consisting of one such 2×2 block for each momentum k. The band Hamiltonian $\hat{H}(k)$ can now be further diagnolized to reveal the dispersion

relation, and the energy eigenvalues turn out to be

$$E(k) = \pm\sqrt{J_1^2 + J_2^2 + 2J_1 J_2 \cos(k)} \tag{4.6}$$

with associated eigenvectors

$$|\pm(k)\rangle = \begin{pmatrix} \pm e^{i\phi(k)} \\ 1 \end{pmatrix} \tag{4.7}$$

parameterized by $\phi(k) = \tan^{-1}(\frac{J_2 \sin k}{J_1 + J_2 \cos k})$. The dispersion relation is plotted in Figure 4.3 for different configurations of J_1 and J_2, and it becomes obvious that there

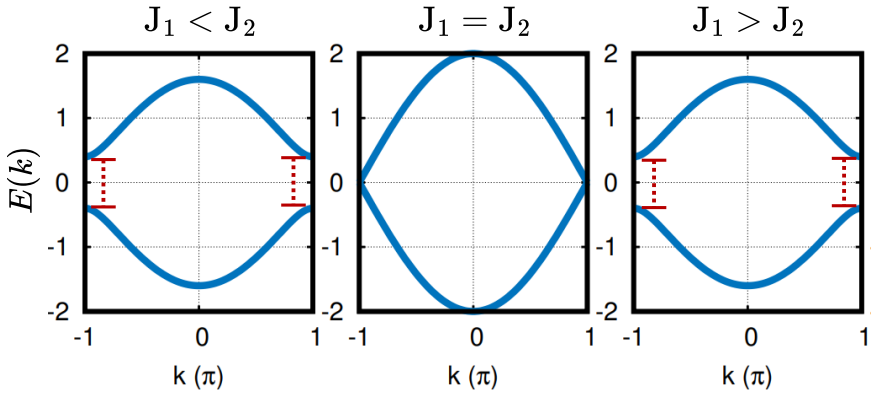

Figure 4.3 : Energy dispersion Equation 4.6 plotted for different scenarios of J_1, J_2. For $J_1 < J_2$ and $J_1 > J_2$, there exists band gap of size $2|J_1 - J_2|$, while at $J_1 = J_2$, the gap closes.

exists an energy gap of $\Delta = 2|J_1 - J_2|$, making the SSH lattice an insulator when the tunneling rates are staggering ($J_1 \neq J_2$). The band gap closes if and only if $J_1 = J_2$, in which case the system becomes a metal.

4.1.2 Winding number

So far the band structure contains nothing "topological" looking, and the two cases where $J_1 < J_2$ and $J_1 > J_2$ seem entirely equivalent. This symmetry will be broken

with a closer inspection of the eigenstates in Equation 4.7. We begin by rewriting the Hamiltonian 4.5 in the geometrical form

$$\hat{H}(k) = \vec{h}(k) \cdot \vec{\sigma} \tag{4.8}$$

in terms of the Pauli matrices

$$\sigma_x = \begin{pmatrix} 0 & 1 \\ 1 & 0 \end{pmatrix}, \ \sigma_y = \begin{pmatrix} 0 & -i \\ i & 0 \end{pmatrix}, \ \sigma_z = \begin{pmatrix} 1 & 0 \\ 0 & -1 \end{pmatrix} \tag{4.9}$$

and matching the components of $\vec{h}(k)$ to 4.5 yields

$$h_x(k) = J_1 + J_2 \cos(k) \tag{4.10}$$

$$h_y(k) = J_2 \sin(k) \tag{4.11}$$

$$h_z(k) = 0 \tag{4.12}$$

By noticing $|\vec{h}(k)|^2 = E(k)^2$ and that $\tan\phi = h_y/h_x$, we discover that the direction of pointing and the magnitude of the vector $\vec{h}(k)$ in the $h_x - h_y$ plane give the eigenstate and the corresponding energy eigenvalue respectively.

A complete set of eigenstates can be represented by the trajectory of $\vec{h}(k)$ over the Brillouin zone ($\phi : -\pi \to \pi$). As shown in Figure 4.4 depicting different scenarios of J_1 and J_2, the trajectory is a circle of radius J_2 in the $h_x - h_y$ plane centered at $\vec{h}(k) = (J_1, 0, 0)$. Note that the origin $\vec{h}(k) = 0$ in the $h_x - h_y$ plane corresponds to zero energy, which matches the gap-less metallic situation. As a result, the origin falls on the $\vec{h}(k)$ trajectory for $J_1 = J_2$, which separates the other two cases $J_1 < J_2$ and $J_1 > J_2$, where the trajectory of the former encloses the origin while the latter does not. Now these two previously symmetric cases have different behaviors, and we may characterize it using winding number $\mathcal{W}$.

The mathematical concept of the winding number represents the number of times a closed curve in a plane travels counterclockwise around a fixed point. It is particularly

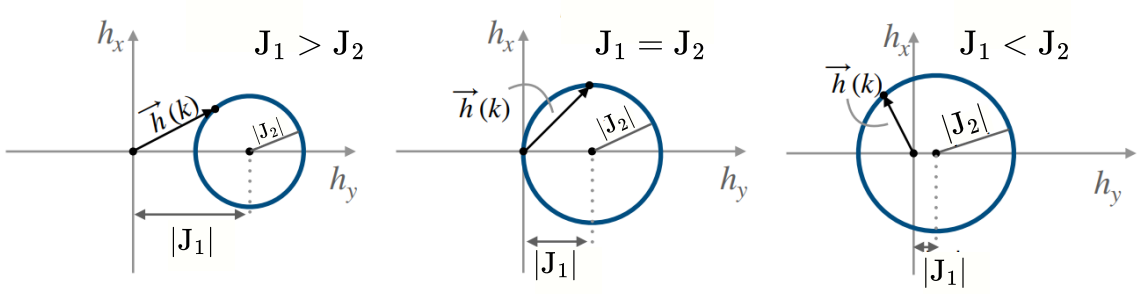

Figure 4.4 : Illustration of different winding situations in the $h_x - h_y$ plane of the geometric representation $\vec{h}(k)$. At $J_1 < J_2$, the $\vec{h}(k)$ trajectory of the Brillouin zone encloses the origin. Figure adopted from Ref. [3].

useful in complex analysis with Cauchy's residue theorem in that it relates integration along closed loop to simply counting the number of poles enclosed by the loop [119]. In the context of quantum physics, discussion of the winding number is generally related to the Berry phase, which is the geometric phase a quantum state acquires over cyclic adiabatic processes in the parameter space of the Hamiltonian [120], such as along the trajectories $\vec{h}(k)$ in our $h_x - h_y$ plane of the SSH Hamiltonian. The Berry phase is responsible for many quantum mechanical phenomena such as the well known Aharonov-Bohm effect [121]. In one dimension, the Berry phase is also known as the Zak phase [122], and it can be shown to take value of $\Phi_{Zak} = \pi\mathcal{W}$ (modulo 2π), where the winding number $\mathcal{W}$ in the SSH case is simply the number of times the trajectory $\vec{h}(k)$ winds about the origin $\vec{h}(k) = 0$.

Now that we are characterizing the topological property of the bulk SSH model using the winding number, it becomes clear that $J_1 < J_2$ and $J_1 > J_2$ are two distinct

topological phases as the winding number takes different values

$$\mathcal{W} = \begin{cases} 1 & J_1 < J_2 \\ 0 & J_1 > J_2 \\ \text{undefined} & J_1 = J_2 \end{cases} \tag{4.13}$$

Moreover, by further inspection of Figure 4.4 one can conclude that a smooth transition between $J_1 < J_2$ and $J_1 > J_2$, both of which are insulating phases by band structure, is not possible without going through the $J_1 = J_2$ trajectory that passes the origin $\vec{h}(k) = 0$. This involves closing the energy gap in the process, which constitute a discontinuous deformation of the shape of the band structure, making this a topological phase transition.

Direct measurements of the winding number, or other topological invariance associated with geometric phases, can be difficult. Experiments in past, such as in the first direct measurement of the Zak phase using a 1D optical superlattice [123], have involved complex methods such as an interferometric approach that requires preparation of individual eigenstates, which can be challenging. It was later proposed that an observable called the chiral displacement [124] can allow one to extract the winding number in 1D chiral system via dynamics of initially localized state [125, 81]. More details will be discussed later in this chapter on how we used the chiral displacement to measure the winding number in the SSH model and probed the topological phase transition.

4.1.3 Topologically protected edge states

Although it is established now that $J_1 < J_2$ and $J_1 > J_2$ correspond to two topologically distinct phases, we have not seen the actual physical consequences of the

different topology as characterized by the winding number. To do that we will actually need to throw away the periodic boundary condition and look at a finite version of the SSH lattice.

For simplicity we will mostly consider a six-site model, same as our experimental setup presented later this chapter. The Hamiltonian in Equation 4.1 is unchanged but with the number of unit cell fixed at $N = 3$. This finite Hamiltonian can be exactly diagonalized to solve for its eigen-energies and the corresponding eigen-states. Shown in Figure 4.5 are the eigen-energies plotted in units of tunneling rate J_1 as a

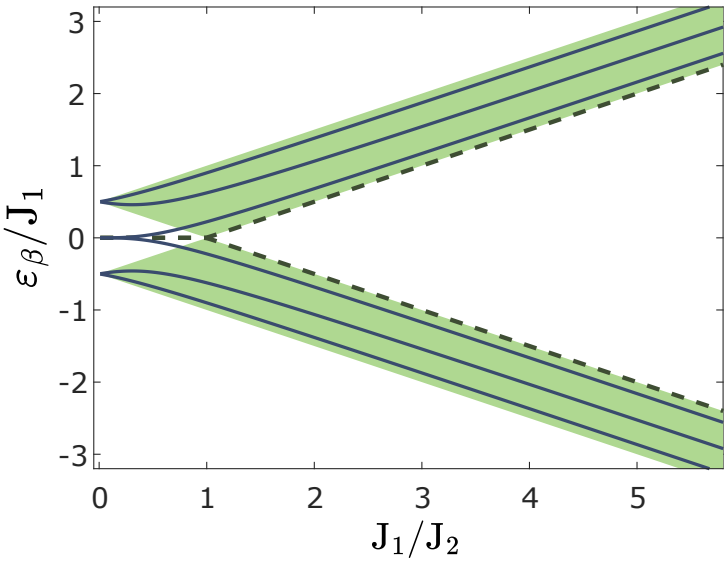

Figure 4.5 : Calculated eigen-energies of six-site SSH as a function of the tunneling rate ratio J_1/J_2 plotted in units of J_1. Shaded region and the dashed lines indicate the calculated energy bands for a large ($N \gg 1$) lattice.

function of the tunneling ratio J_1/J_2. In the large-N limit, there exists a gap between the upper and lower energy bands (green shaded region), and the band gap closes only at exactly $J_1 = J_2$ as predicted in 4.1.1. However, below the band gap closing ($J_1/J_2 < 1$), the two middle eigen-states (dashed lines) merge and remain at zero

energy. This can be understood in the limiting case $J_1 = 0$, $J_2 \neq 0$, where the two sites on both ends of the finite lattice are disconnected from the rest of the chain which is dimerized. There exist two eigen-states with the particle localized on either of the two sites, and both states have zero energy since the Hamiltonian in Equation 4.1 contains no on-site energy term. They are hence known as the protected edge states, and it is important to note that this localization is a universal behavior as a result of the tunneling topology and is therefore not limited to the extreme case of $J_1 = 0$, $J_2 \neq 0$. Even in the 6-site case (blue curves in Figure 4.5), despite that the band gap never really closes until $J_1/J_2 \to 0$ because of finite-size effect, the band structure is qualitatively depicted, and the emergence of the zero-energy edge states are visible as tunneling ratio J_1/J_2 decreases.

The notion of these topologically protected edge states become more apparent upon analyzing the eigen-states of the lattice Hamiltonian. Figure 4.6 shows, for the 6-site lattice, the six eigen-states decomposed into the basis of the individual lattice sites. At tunneling ratio $J_1/J_2 = 0.2 \ll 1$, with winding number $\mathcal{W} = 1$ and the presence of protected edge states, the wave-functions of the two middle eigen-states are mostly concentrated on the boundaries as expected. While the other four eigen-states with non-zero energies have probability density delocalized over all the inner sites. In the opposite case $J_1/J_2 = 5 \gg 1$, where winding number $\mathcal{W} = 0$ vanishes, all eigen-states are delocalized over the entire lattice. These two cases are known as the topologically non-trivial and trivial phases respectively, and they are connected by the topological phase transition happening at uniform tunneling $J_1/J_2 = 1$. Note that the existence of zero-energy protected edge states is the result of the non-trivial topology predicted by the winding number $\mathcal{W}$, which is a topological invariant derived from the bulk (boundary-less) Hamiltonian, making this a classic example of the bulk-edge

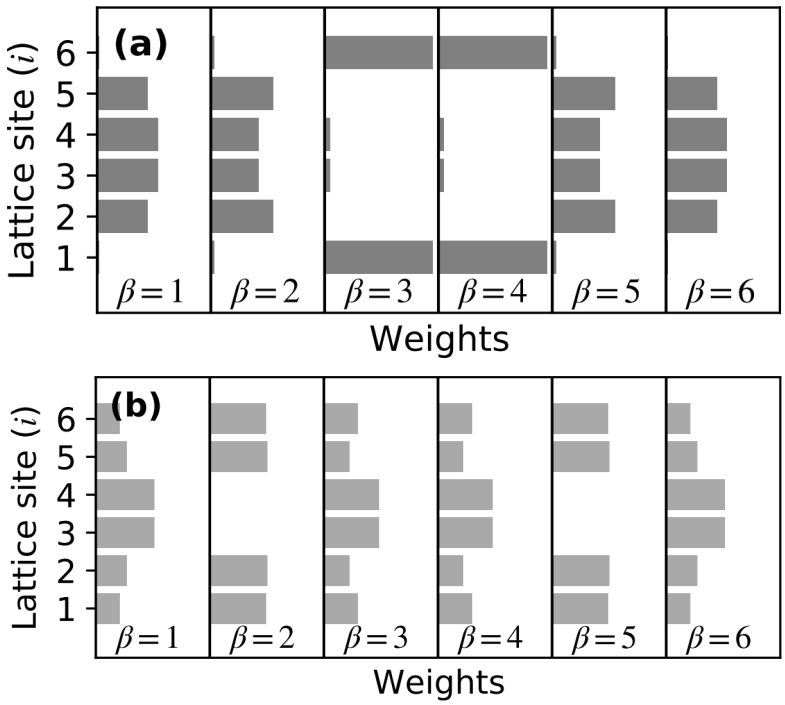

Figure 4.6 : Eigen-states of the six-level SSH lattice calculated by directly diagnolizing the Hamiltonian at $J_1/J_2 = 0.1$ in (a) and at $J_1/J_2 = 10$ in (b). Each eigen-state $|\beta\rangle$ is decomposed into basis of the six bare Rydberg levels $|i\rangle$. The horizontal bars represent the probability density weights $|\langle\beta|i\rangle|^2$. Figure from Ref. [4].

correspondence.

4.2 S-state Rydberg ladder as synthetic lattice sites

As briefly advertised in Section 1.2, Rydberg states, for the n^{-3} scaling of adjacent-level energy spacing, can have transitions resonant with easily accessible microwave frequencies in the ranges of 10-50 GHz. This makes Rydberg states suitable candidates for building synthetic dimension systems. The SSH Hamiltonian introduced in depth above, for its strikingly simple 1D structure and yet rich and prominent topological behavior, has served as an ideal test model for demonstrating synthetic dimension platforms [79, 81, 126]. In the following sections, I will describe a series

of experiments where we demonstrate Rydberg synthetic dimensions by realizing and characterizing a 6-site SSH Hamiltonian.

4.2.1 Previous experiments

A few years ago, we demonstrated, for the first time, a Rydberg synthetic dimension using a ladder of microwave-coupled $^3S_1$ and $^3P_1$ Rydberg states created within a single ^{84}Sr atom [4]. When $\mathrm{J}_1 < \mathrm{J}_2$ as set by the microwave driven transition rate, we observed the degenerate edge states and its topological protection which was robust against perturbations respecting the chiral symmetry of the tunneling pattern [117]. However, among the transitions making up the ladder, the $5sns\ ^3P_1 - 5s(n+1)s\ ^3S_1$ transition was not SFI resolvable, meaning the two states ionize at the same electric field, resulting in lack of ability to see the full state composition within the ladder. Moreover, the $^3S_1 - {}^3P_1$ transitions, generally have short coherence time, which prevented us from making dynamics measurements on time scale long enough comparable to the characteristic time $1/J$.

In the work of this thesis, we present a more thorough inspection of the Rydberg SSH lattice, including eigenstate-resolving energy spectra and direct dynamics measurements of Rydberg state composition [5]. The topological phase transition was also inspected by measuring the winding number $\mathcal{W}$ through system dynamics at different values of tunneling ratios $\mathrm{J}_1/\mathrm{J}_2$ [90].

4.2.2 Two-photon S-S transitions

The entirety of our experiments inspecting the SSH Hamiltonian in Rydberg synthetic dimensions were done using microwave tones generated using the combiner setup as shown in Figure 2.22. The frequencies are used to resonantly drive $5sns\ ^3S_1 - 5s(n+$

1)s $^3S_1$ two-photon transitions to couple adjacent Rydberg levels in a single ^{84}Sr atom. The transitions involved are in the range of $n = 58 - 64$, which have already been inspected in the maximum Rabi frequency study shown in Table 3.4. At the same time, up to five consecutive tones are combined at the same time, connecting a 1D lattice of six $5sns$ $^3S_1$ Rydberg states. However, for synthetic dimension experiments here we used the combiner setup to generate the microwave tones for spectral cleanness, which also results in slightly different values of $\Omega_R^{(max)}$.

Similar to the characterization of the microwave transitions discussed in Chapter 3, the experiments were carried out with the cloud of cold ^{84}Sr atoms in the optical dipole trap (ODT). Although specific condition of the atomic sample is not critical for the experiments because all the Rydberg dynamics happen within a single atom, the essential parameters of the sample are kept constant with minor variations: ∼500K-1M atoms, with peak densities $\sim 10^{11}$ cm^{-3}, and temperature $T \sim 1\,\mu$K.

4.2.3 SFI resolvability

The major advantage for which we adopted a purely S-state lattice is the ability to resolve constituent states on the ionization spectra. This SFI resolvability has been demonstrated by results shown in Chapter 3 in the simple case of a single $5sns$ $^3S_1$−$5s(n+1)s$ $^3S_1$ transition. The generalization to six states is straightforward. Shown individually in Figure 4.7 are the SFI spectra of six consecutive $5sns$ $^3S_1$ states with $n = 58 - 63$ under the same set of ionization ramp voltages. The arrival time of each individual atomic levels are well separated, indicating the ability of resolving state composition when they co-exist on a single ionization profile.

It can be noted that, towards earlier part of the ionization ramp, the arrival time separation between the states with higher n gradually decreases, as well as the

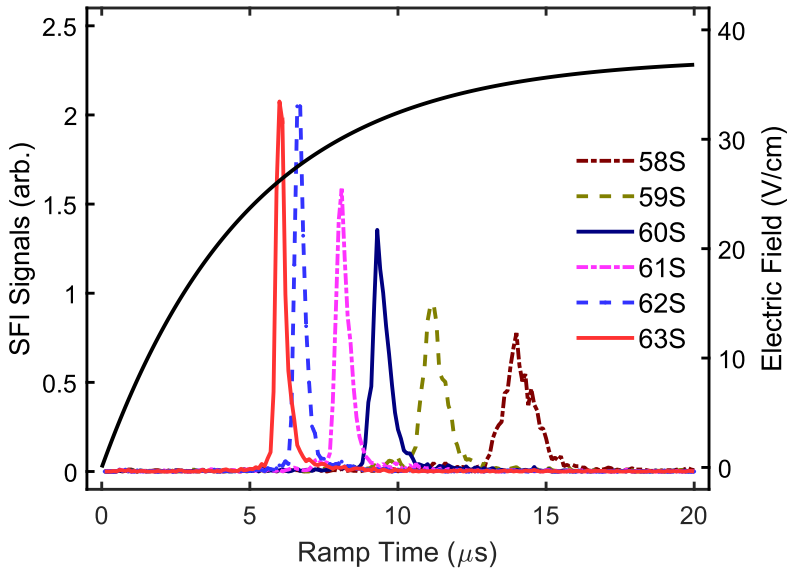

Figure 4.7 : SFI spectra recorded by creating and ionizing individual atomic states of interest involved in the Rydberg synthetic lattice. The time evolution of the applied electric field is also shown. From [5].

widths of the peaks. This is a result of the exponential time profile causing the ionization voltages to vary quicker at earlier time. In the configuration of Figure 4.7, the maximum ionization voltage (i.e. at $t = 20\,\mu s$) would not be enough to efficiently ionize the next lower state $57s$, and the two highest states $62s$ and $63s$ are already visibly overlapping in arrival time. This motivates fitting of the SFI spectra as a high-contrast way to extract the Rydberg population in each state.

Another manifestation of the exponential time profile on a shorter time scale is the noticeable asymmetry within each ionization peak, which demands a more accurate line-shape model to be reliably fitted. We use a skewed Gaussian function in the

following form.

$$S(t) = G(t) \cdot \text{erfc}(-\frac{a(t-\mu)}{\sqrt{2}\sigma}) \tag{4.14}$$

$$G(t) = \frac{A}{\sigma\sqrt{2\pi}} \cdot \exp\left(-\frac{1}{2}\frac{(t-\mu)^2}{\sigma^2}\right) \tag{4.15}$$

Here $G(t)$ is the standard Gaussian distribution with amplitude A, width σ and center μ, and it is modified in $S(t)$ by the error function defined by the skewness parameter a. Shown in Figure 4.8 is an example spectrum of the pure atomic state of $59s$ with the skewed Gaussian fit. It can be seen that the spectral tilting towards early time is well captured in the fitted line.

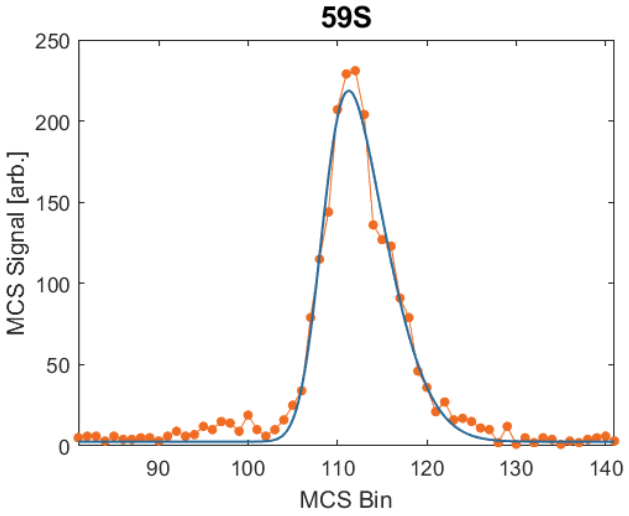

Figure 4.8 : A snapshot of the ionization spectrum of the 59S Rydberg state. Signal as a function of arrival time is fit to a skewed Gaussian profile as shown in Equation 4.15.

In the actual experiments where presence of multiple atomic states are expected on the same spectrum, we fix all other parameters (center position μ, width σ and skewness a) of the individual atomic components and only let the amplitudes A vary. The small number of free parameters provides good reliability for this fitting

method. However, it should be noted that since the ionization electric field ramp profile need to be kept the same in the experiments as is used in all the pure atomic states characterization. Figure 4.9 demonstrates one of the configurations used in the SSH experiment. Here we set the HV supplies to be outputting $-88.3\text{V}/+71.4\text{V}$, which results in the ionization electric field ramp shown in Figure 4.7. The results of individual fitting of the pure atomic state profiles are shown in Table 4.1. These parameters are fixed for each atomic components shown in the fit lines in Figure 4.9, which displays clear state resolvability with good contrast.

State	$\boldsymbol{\mu}$	$\boldsymbol{\sigma}$	**a**
63s	58.8	2.51	2.75
62s	65.1	2.65	2.92
61s	78.9	3.70	3.27
60s	91.3	4.52	2.97
59s	108.4	5.67	2.58
58s	135.8	7.81	2.07

Table 4.1 : Parameters extracted from fitting individual pure atomic ionization time spectra to skewed Gaussian distribution. These parameters (center $\boldsymbol{\mu}$, width $\boldsymbol{\sigma}$ and skewness **a**) are obtained with the ionization supply voltages at $-88.3\text{V}/+71.4\text{V}$, and they are fixed when fitting the experimental ionization spectra with all of them present.

In the current case of a single electric field ramp ionizing up to six states, which is the upper limit in this work, the atomic-level components are still relatively well separated on the ionization spectra. As a result, the skewed Gaussian fitting does not bring drastic enhancement to the population contrast compared to simple windowing as shown in Figure 4.9. However, in future experiments where more states are present

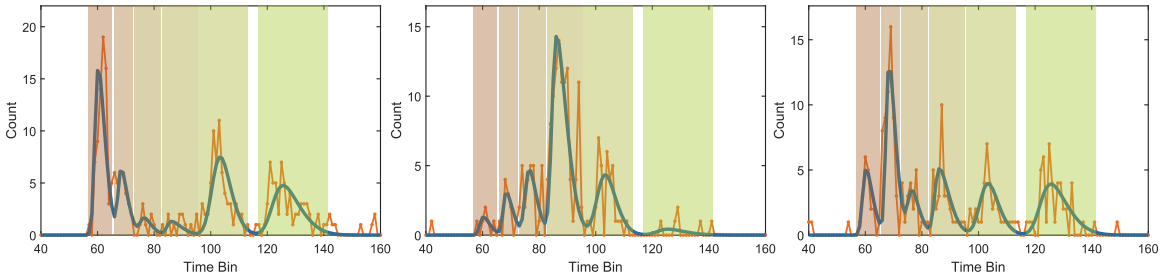

Figure 4.9 : Examples of ionization spectra where the raw Rydberg count (orange) is fitted to six peaks of skewed Gaussian as described by Equation 4.15 with parameters in Table 4.1. The shaded areas indicate rough windows of time bins that represent each states.

on the ionization spectrum, fitting will be necessary in order to achieve state-resolving detection. Another alternative solution, in the case of a larger number of states, is to repeat the same experiment sequence with multiple sets of ionization ramp voltages, each of which covers a subset of all the states. Results from subsets can be combined in post-analysis to retrieve the complete state composition.

4.3 Observation of protected edge states

(The c ontent of this section follows, to a large extent, work presented in our published paper Ref.[5])

As discussed in Section 4.1, the topologically protected edge states will be manifested in both the eigen-energy spectrum, which measures the band structure of the Rydberg lattice, and its eigen-state composition. In the following experiment, we create a 1D SSH ladder using six $5sns\,^3S_1$ states described above, and the five microwave frequencies used to drive the adjacent-n two-photon $S-S$ transitions are listed in Table 4.2 with their respective microwave power settings and resulting Rabi frequencies. The Rabi frequencies follow the $\mathrm{J}_1-\mathrm{J}_2$ alternating pattern with the weaker $\mathrm{J}_1 \approx 160\,\mathrm{kHz}$

Transition	Frequency (MHz)	Power (dBm)	Ω (kHz)
58S-59S	19638.360	-5.4	164
59S-60S	18606.440	5.9	808
60S-61S	17646.885	-1	162
61S-62S	16751.815	-5.1	804
62S-63S	15915.945	-10.3	162

Table 4.2 : Transitions used for constructing the six-state SSH lattice in the topological phase. The microwave source power are adjusted for each applied frequency so as to realize the J_1/J_2 alternating pattern for the coupling Rabi frequencies (tunneling rates) with $J_1 \approx 160$kHz, $J_2 \approx 800$kHz.

on the edges and $J_1 \approx 800\,\mathrm{kHz}$ with a tunneling ratio $J_1/J_2 = 0.2 < 1$, corresponding to the topologically nontrivial regime. The values of J_1, J_2 are determined by the Autler-Townes splitting measurements of the individual transitions. In this configuration, we may rewrite the system Hamiltonian in Eqn. 4.1 in a finite form for our Rydberg lattice as

$$\hat{H}_{\text{lattice}} = \sum_{n=1}^{2N-1} -hJ_{n,n+1}\left(\hat{c}_n^\dagger \hat{c}_{n+1} + h.c.\right) + \sum_{n=1}^{2N} \hat{c}_n^\dagger \hat{c}_n U_n \tag{4.16}$$

where $2N$ is the total number of bare states and $N = 3$ is the number of dimerized unit cells, and the tunneling rates alternate as $J_{n,n+1} = J_1(J_2)$ for $n = 1, 3, 5(2, 4)$. Note that second term, which indicates an on-site potential energy in the lattice model, arises due to the fact that applied microwave frequencies may not exactly match that of the resonance of respective transitions. In addition, it can be shown that, the size of U_n is determined by the detuning of the microwave transitions. For now, we will proceed with the assumption that $U_n = 0$ for all n, and the discussion of how to achieve this resonance condition by adjusting microwave frequencies according to the

AC Stark shift measurements presented in Section 3.2.3 will be left for later.

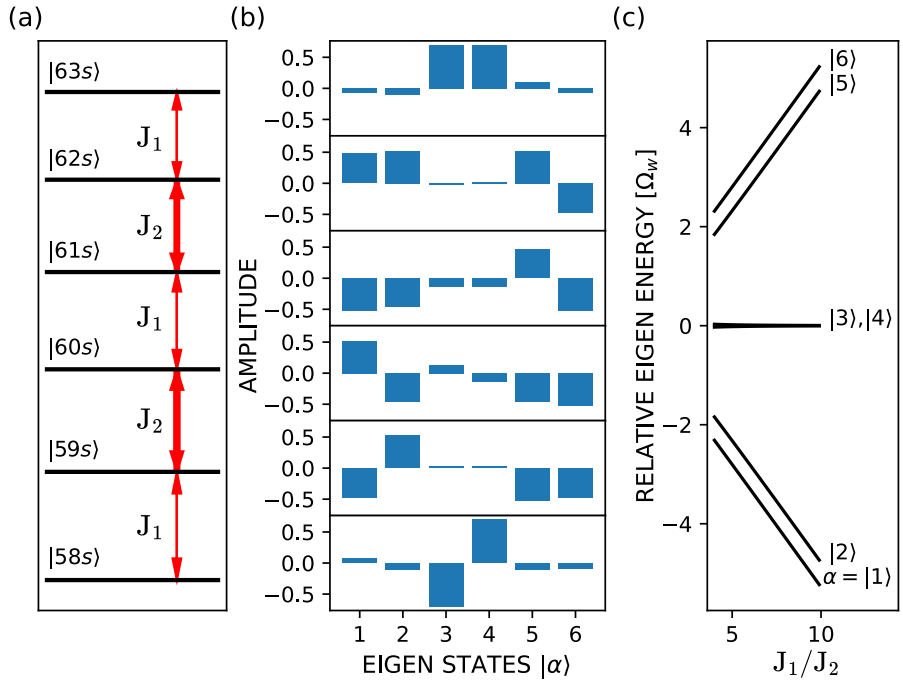

Figure 4.10 : (a) The bare six-level lattice used in the present study. The coupling strengths are $J_1 = 160$kHz, $J_2 = 800$kHz. (b) Projection of the initial individual $|ns\rangle$ bare states into the dressed-state basis, $|1\rangle$-$|6\rangle$. The bars show the overlap amplitudes $\langle\alpha|ns\rangle$ [see Eqn 4.19], which may be chosen to all be real, and their phases relative to each other. (c) Energy-level structure in the dressed-state basis expressed as a function of J_1/J_2. Figure from [5].

With $U_n = 0$, we may now set up and diagnolize the Hamiltonian

$$\langle \hat{H}_{lattice} \rangle = -h \begin{bmatrix} 0 & J_2 & 0 & 0 & 0 & 0 \\ J_1 & 0 & J_2 & 0 & 0 & 0 \\ 0 & J_2 & 0 & J_1 & 0 & 0 \\ 0 & 0 & J_1 & 0 & J_2 & 0 \\ 0 & 0 & 0 & J_2 & 0 & J_1 \\ 0 & 0 & 0 & 0 & J_1 & 0 \end{bmatrix} \tag{4.17}$$

with $J_1 = 160$kHz, $J_2 = 800$kHz for model calculations. As shown in Figure 4.10 (b), the eigen-states $|\alpha\rangle$ are composed of distinct superposition of the six bare Rydberg states $|58s\rangle - |63s\rangle$. It can be seen that $|\alpha = 3\rangle$ and $|\alpha = 4\rangle$ are the topologically protected edge states, which are nearly degenerate around zero energy, and their probability distributions (vertical columns) are primarily concentrated on the two Rydberg sites on the boundary.

Generic experimental configuration for observing the protected edge states is illustrated in Figure 4.11. The $5sns\,^3S_1$ Rydberg manifold is accessed via two photon laser excitation via the $5s5p\,^3P_1$ intermediate state. Optical/microwave exposure sequences for measuring the population dynamics and eigen-energy spectra take similar form as that used for characterizing Rabi oscillations and Autler-Townes splitting respectively as discussed in Chapter 3.

4.3.1 Eigen-energy spectrum

For measurements of the eigen-energy spectrum, the microwave fields are turned on before laser excitation, such that the lasers excite atoms into the microwave-dressed synthetic space instead of into the bare Rydberg states. This is similar to the Autler-Townes splitting measurements discussed in Section 3.1.3. The eigen-energy measurements here simply extend that process from two levels to six Rydberg levels coupled by microwaves. The laser frequency can be scanned near any of the $n\,^3S_1$ state, and the measured total excitation rate, i.e., the sum of all states present in the ionization spectrum, provides a probe of the eigen-states through their overlap with the selected $n\,^3S_1$ state. Quantitatively, the total Rydberg excitation rate is given by

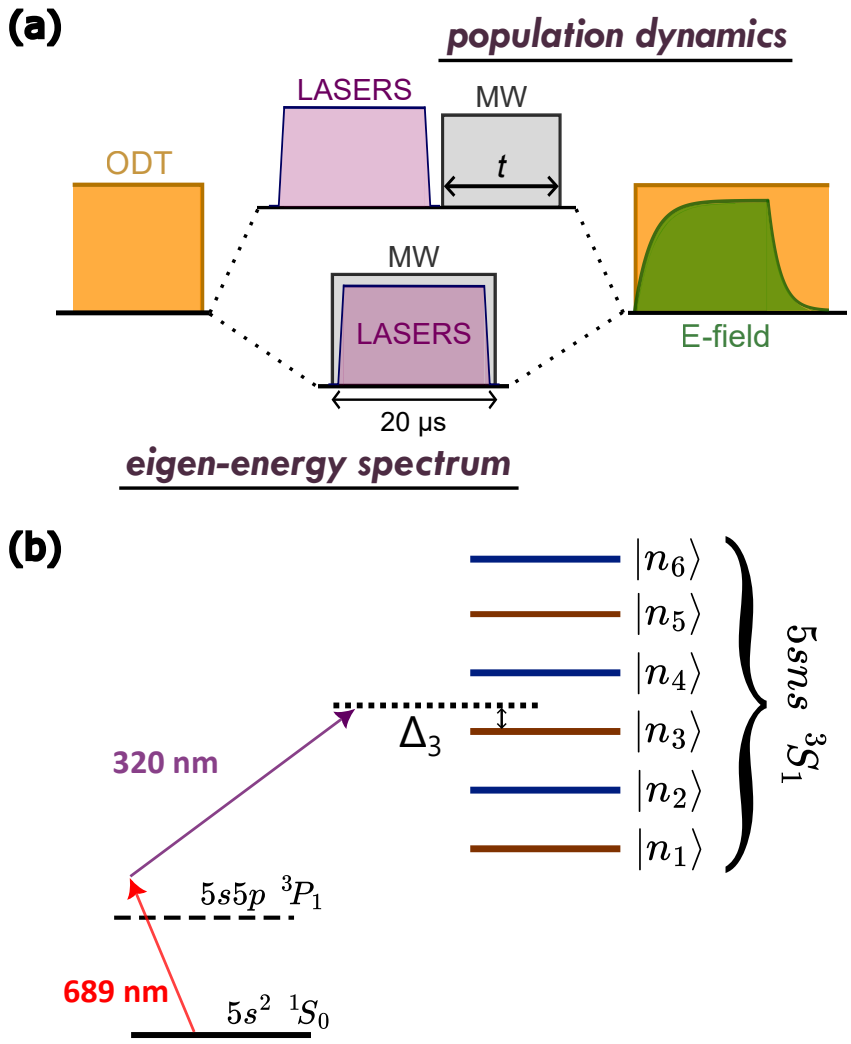

Figure 4.11 : **(a)** The pulse sequence of an experimental cycle. The optical dipole trap (ODT) is turned off during optical/microwave exposure. The ionizing E-field is ramped up after this exposure and decays to zero by the beginning of next cycle. The upper and lower branches show the exposure sequence for the population dynamics and eigen-energy spectrum measurements respectively. **(b)** Experimental realization of the six-site SSH model. Selected n^3S_1 Rydberg states are excited using two-photon transitions through the intermediate $5s5p^3P_1$ state. The laser frequency can be tuned near any selected $|n_i\rangle$ state with detuning Δ_i. Neighboring states are coupled by two-photon microwave transitions.

a form similar to 3.13 as

$$\Gamma(\Delta_i) \propto \sum_{\alpha} |\langle \alpha | n_i \rangle|^2 \, \delta(\Delta_i - \epsilon_\alpha/\hbar) \tag{4.18}$$

where the overlap with the selected bare state $|n_i\rangle$ is summed over all eigen-states $|\alpha\rangle$ with eigen-energies ϵ_α. The delta function, enforcing energy conservation, ensures that the excitation rate peaks when the laser detuning Δ_i from the energy of the bare state $|n_i\rangle$ matches one of the eigen-energies ϵ_α of the Hamiltonian, Eqn. 4.16. The laser linewidths, combined with the 20 µs laser pulse widths, result in an effective laser linewidth of $\sim 120-140$ kHz at $n \sim 60$, sufficient to easily resolve all the eigen-states of interest here.

Figure 4.12(a) shows the excitation spectrum recorded as the laser frequency is scanned across the third bare Rydberg state $|n_3\rangle$ in the synthetic lattice. The vertical bars show the expected peak heights and positions of the eigen-states calculated by directly diagnolizing the Hamiltonian and evaluating $\Gamma(\Delta_3)$, essentially the squares of the horizontal rows in Figure 4.10 (b). As we have discussed, in the topological regime

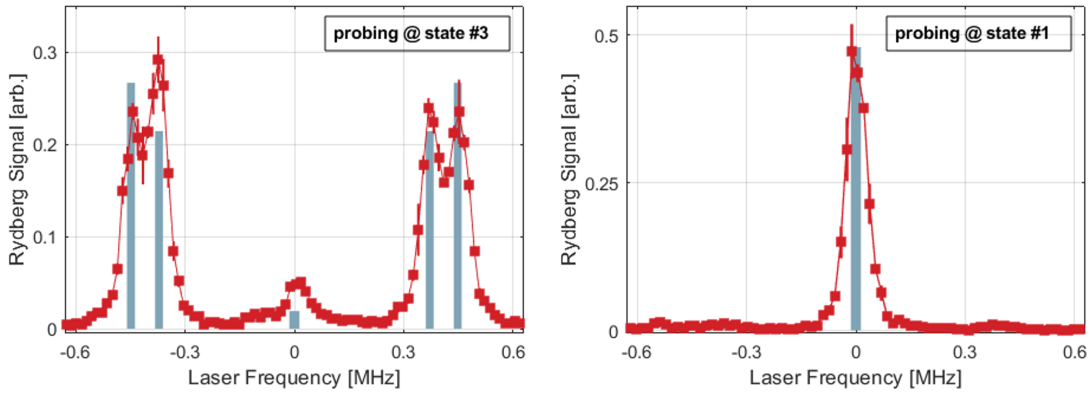

Figure 4.12 : Eigen-energy spectra of the 6-state SSH lattice measured via Rydberg excitation spectra with the laser frequency probing around the 3rd ($|60s\rangle$) and 1st ($|58s\rangle$) bare levels separately. The vertical bars indicate the expected height of each peak located at their respective eigen-energies.

with $J_1/J_2 = 0.2 < 1$, the SSH model is expected to host zero-energy edge states, which correspond to the middle peak at zero in Figure 4.12(a). Here the two edge states are nearly degenerate with energy difference too small to be resolved spectrally and hence appear to be a single peak. Their relatively small peak heights are due to the weak overlap between bare states $|n_3\rangle$ and the edge states as was shown in Figure 4.6. On the other hand, part (b) of Figure 4.12 shows the excitation spectrum with the laser frequency being scanned across the first bare state $|n_1\rangle$. This sits at the lattice boundary and almost only overlaps with the edge states, which results in a dominant single-peak spectrum at zero energy.

In both cases, the general shape of the measured spectra match well the calculation, which confirms the resonance condition that $U_n = 0$. The deviations may be partially attributed to uncertainties in the tunneling rates and in the microwave detuning, which are not considered in the calculations. The emergence of zero-energy components on the excitation spectra is a direct evidence of the topological protected edge states. This spectral observation was also presented in the previous result in Ref.[4], where the laser linewidth was not narrow enough to resolve the two individual states on each side as in Figure 4.12(a).

4.3.2 Population dynamics

While the eigen-energy spectra provides an insightful probe of the SSH Hamiltonian in a steady-state approach, being able to inspect the dynamical behavior of a synthetic-dimension system can be useful in many aspects, including the possibilities of studying quench-type interactions and the potential applications of topological protected states in quantum information processing.

Similar to observing the Rabi oscillations, our study of the state dynamics in

the SSH lattice consists of measuring the fractional population (probability) in each bare Rydberg states $|n_i\rangle$ as a function of evolution time under the SSH Hamiltonian. As illustrated by the top sequence in Figure 4.11 (a), the atom is first excited to a selected $|n_i\rangle$ Rydberg level. After that, the microwave fields are turned on for a duration t, allowing the population to evolve under the couplings. Immediately following extinction of the microwave fields, the population in each Rydberg state is measured using SFI. Repeated measurements with varying microwave exposure times t are used to examine the population dynamics.

Consider initially the case where the $|59s\rangle$ Rydberg state is excited. Figure 4.13 shows the time evolution of the relative populations in the different coupled bare states as a function of the time for which the microwave fields are applied. The total Rydberg population, which is not shown, decays with a time constant of $\sim$70 µs predominantly due to radiative decay. To compensate for this decay and better emphasize the population dynamics, Figure 4.13 shows the evolution of the fractional populations in each $|ns\rangle$ level, i.e., at every point in time the total Rydberg signal is normalized to unity. Figure 4.14 shows the actual SFI spectra where the arrival time signals are fitted to extract the population fraction at the two evolution times $t = 5.05\mu$s and 12.9μs marked by the dashed lines in Figure 4.13.

Inspection of the population dynamics shows that, in essence, whereas at $t = 0$ all the atoms are in the $|59s\rangle$ state, the strong coupling to the $|60s\rangle$ level results in rapid antiphase oscillations between their populations. However, as time increases the weak coupling between the $|60s\rangle$ and $|61s\rangle$ states allows the wave packet to transfer into the strongly coupled $|61s\rangle$-$|60s\rangle$ pair until, by $t \approx 7$ µs, essentially all the population density is entirely localized in this pair. Further evolution leads to continuing periodic transfer of population between the $|59s\rangle$-$|60s\rangle$ and $|61s\rangle$-$|62s\rangle$ pairs. Whereas strong

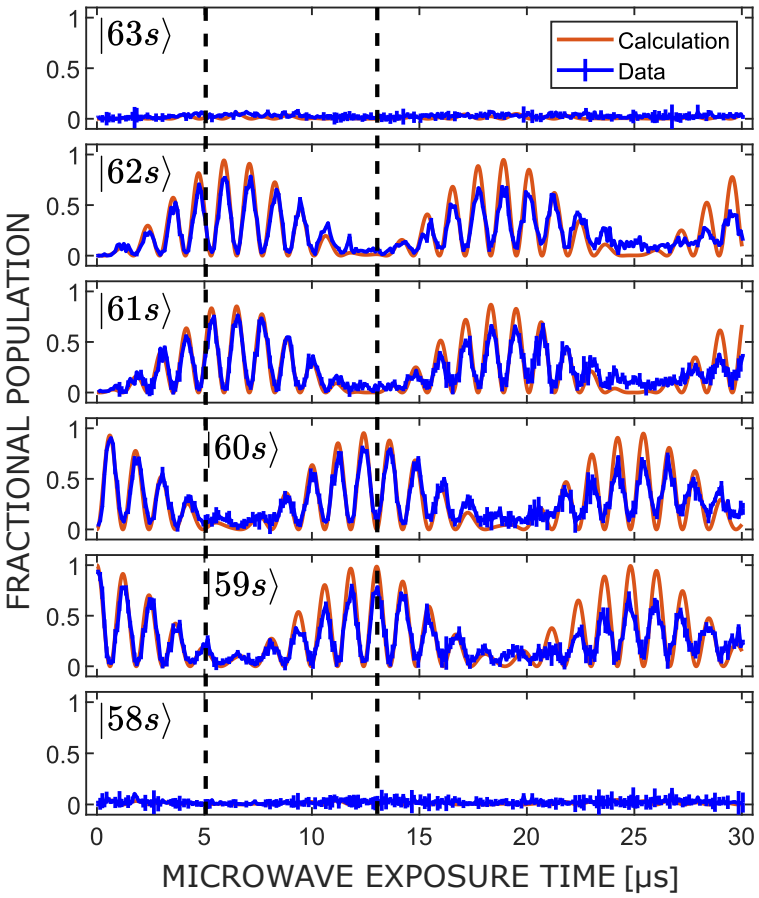

Figure 4.13 : Full state composition dynamics with the Rydberg population initiated on the third state $|n_3\rangle = |59s\rangle$ in the topological configuration. Figure from Ref.[5].

oscillations are seen between the bulk states, no population transfer to the $|58s\rangle$ and $|63s\rangle$ edge states is evident. This is typical of dynamics in the bulk of a system with topologically protected edge states.

Such state dynamics can be quantitatively understood by the following process: the microwave fields project the initially pure bare state $|ns\rangle$ into the dressed basis, i.e.,

$$|ns\rangle = \sum_{\alpha=1}^{6} |\alpha\rangle \langle\alpha|ns\rangle \tag{4.19}$$

Since $|\alpha\rangle$ are eigen-states in the presence of the microwave coupling, during the mi-

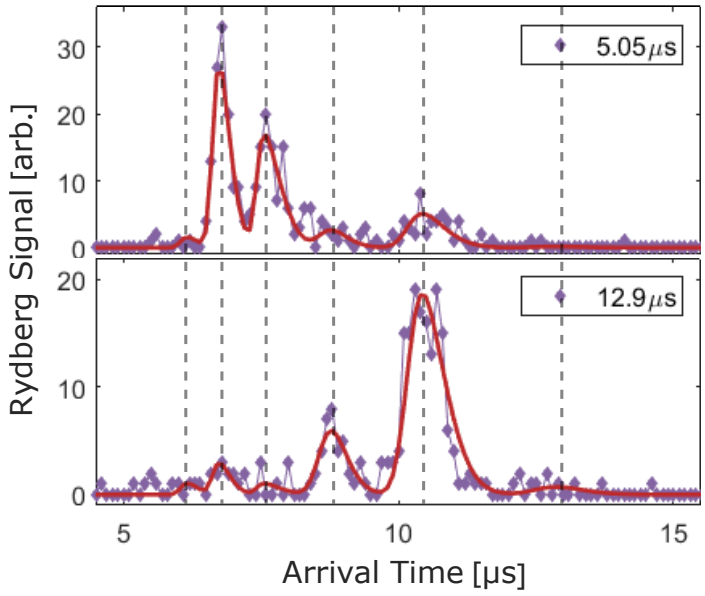

Figure 4.14 : Sampled SFI arrival time spectra recorded at evolution time $t_1 = 5.05\,\mu$s and $t_2 = 12.9\,\mu$s, which are the times indicated by the dashed lines in Figure 4.13. Final fractional populations are obtained by averaging over several such spectra.

crowave exposure time t, they evolve by simply acquiring phase factors corresponding to their respective eigen-energies. As a result, the final population fraction in bare state $|n's\rangle$ after the microwave exposure is obtained by projecting the state at t back to the bare basis as

$$|\langle ns'|\hat{T}|ns\rangle|^2 = \sum_{\alpha,\beta=1}^{6} \langle ns|\alpha\rangle\langle\alpha|ns'\rangle\langle ns'|\beta\rangle\langle\beta|ns\rangle e^{+i\omega_\alpha t} e^{-i\omega_\beta t} \tag{4.20}$$

where the $|\beta\rangle$ are also eigen-states as $|\alpha\rangle$, $\hat{T}$ is the time evolution operator, and $\hbar\omega_{\alpha,\beta}$ are the eigen-energies. The expected dynamics consist of terms oscillating at frequencies $|\omega_\alpha - \omega_\beta|$, and there are three "groups" of eigen-states in terms of energy: $|1\rangle$-$|2\rangle$, $|3\rangle$-$|4\rangle$ and $|5\rangle$-$|6\rangle$ in Figure 4.10 (c). This leads to an intuitive result that, the faster dynamics will be governed principally by the separation between the three "groups" of eigen-states, while slow dynamics by the energy separations within a group.

As is seen in Figure 4.14, model calculations (Eqn. 4.20) reproduce well the observed behavior, and the fact that the boundary sites $|58s\rangle$ and $|63s\rangle$ both stay unpopulated as expected is a direct evidence of the topologically protected edge states. At later times ($t \gtrsim 25$ µs), the amplitude of the population oscillations starts to fall below that predicted by the model. This can be attributed to small detuning of the microwave frequencies. *Ab initio* calculations indicate that frequency detuning less than 50 kHz can lead to damping of the oscillation amplitudes. Furthermore, radiative (or blackbody-radiation-driven) decay to nearby ^3P states can lead to an increasing baseline signal in the SFI spectrum, which again limits the amplitude of oscillations between the coupled states and the contrast in these oscillations. However, even at much later times ($t > 70$ µs), where there are essentially no visible oscillations between the bulk states, no significant population leaks into the edge states, demonstrating that topological protection remains robust in the presence of decoherence.

Figure 4.15 shows a similar population dynamics measurement done with the initial Rydberg excitation creating purely $|58s\rangle$ state on the boundary of the lattice. Initially, for short microwave exposure times, the population remains largely localized in the edge state but begins to tunnel directly into the opposite edge state. Such direct edge-to-edge population transfer is also predicted by the simulations. No significant population buildup in the intermediate bulk states is observed. It should be noticed that, however, small oscillations are observed on population in the $|60s\rangle$ state at early time and are also well reproduced by calculations. This shows the staggered form (overlapping with only the next-nearest neighbor of the edge) of the edge state wave-function as illustrated by 3rd and 4th columns in Figure 4.10(b).

This long-range edge-to-edge tunneling can be understood by noticing that the two zero-energy edge states $|3\rangle$ and $|4\rangle$ are equal (or opposite) superposition of the

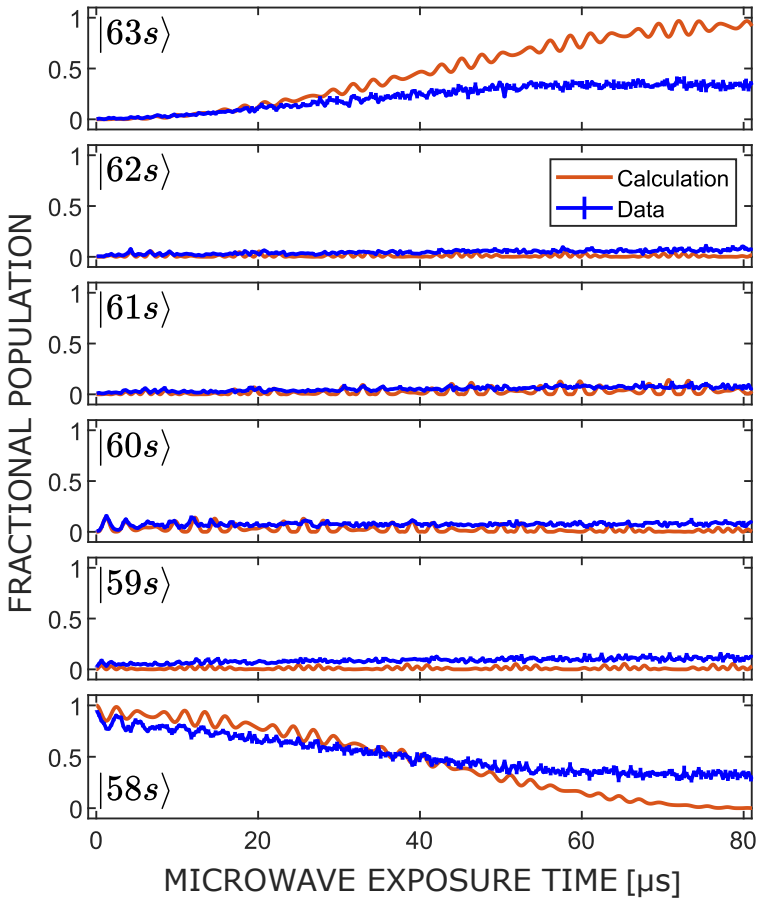

Figure 4.15 : Full state composition dynamics with the Rydberg population initiated on the first state $|r_1\rangle$ in the topological configuration. Figure from Ref.[5].

bare states $|58s\rangle$ and $|63s\rangle$. By initially exciting $|58s\rangle$, we are projecting into a superposition of $|3\rangle$ and $|4\rangle$, which evolves according to their eigen-energies. Therefore, the population oscillations between $|58s\rangle$ and $|63s\rangle$ can be viewed as a quantum beat signal between eigen-states $|3\rangle$ and $|4\rangle$, and the slow tunneling rate is a result of the eigen-energies being nearly degenerate. The time needed to observe a complete population transfer from $|58s\rangle$ to $|63s\rangle$ can be estimated by the inverse of the energy splitting $\Delta_{\text{edge}} = \hbar|\omega_3 - \omega_4|$, which is calculated to be about $1/(2 * 12\text{kHz}) \approx 83.3\mu\text{s}$, consistent with the calculated curve in Figure 4.15. This is significantly longer than

the system coherence time (around $\sim 40\mu$s, which is when measured results start to deviate notably from predictions).

The edge-to-edge tunneling rate, i.e., the energy splitting between the two edge states, also depends sensitively on the number of sites in the synthetic lattice. One can show that, for 1D SSH lattice, every unit cell (two sites) removed leads to an increase in Δ_{edge} by a factor of J_2/J_1. In the case of infinitely many unit cells, the edge-to-edge transfer time goes up to infinity, corresponding to the two edge states being exactly degenerate. Figure 4.16 shows the observed edge-to-edge tunneling for a 4-level SSH lattice, which essentially consists of states that form a subset ($|60s\rangle$-$|63s\rangle$) of the 6-level configuration. The tunneling time here is expected to be $83.3\mu\text{s}/(J_2/J_1) = 16.7\mu$s as indicated by the calculated curves. In this result, we observed more than a full period of beating between $|60s\rangle$ and $|63s\rangle$ before the oscillation amplitude falls notably due to decoherence.

Further experiments and model simulations were undertaken to explore the effects of edge transition detuning, and, through this, the robustness of edge-to-edge tunneling. To this end, a series of measurements were performed in which the $|62s\rangle - |63s\rangle$ transition was purposely detuned. Long-range tunneling from the initially pure $|58s\rangle$ state to the $|63s\rangle$ end is measured as a function of this detuning frequency in Figure 4.17 showing representation dynamics. The population transferred to $|63s\rangle$ is fit to decaying sinusoidal when possible to extract the edge-to-edge tunneling rates, which are plotted in Figure 4.18 for both the four- and six-level lattices. In each case, detuning of the edge transition leads to an increased tunneling rate. In addition, the edge states energy splittings are exactly determined from the minimums of the curves to be $\sim$ 6kHz and $\sim$ 30kHz for 6- and 4-level lattices, consistent with the calculations.

With further detuning of the edge-state transition, chiral symmetry is broken and

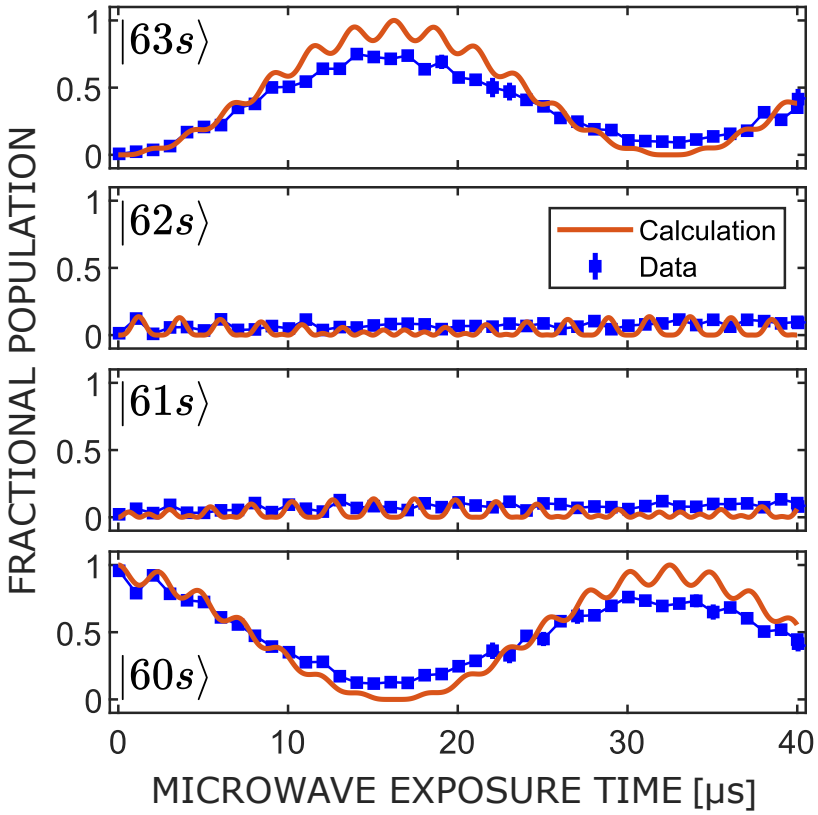

Figure 4.16 : Full state composition dynamics with the Rydberg population initiated on the first state $|r_1\rangle$ in the topological configuration.

the edge states are no longer topologically protected, allowing population transfer from an edge state into the neighboring bulk states (and vice versa). This behavior is demonstrated for the $|58s\rangle$ level in Figure 4.19 which shows, for the six-level lattice, the final relative populations in the bulk and edge bare states, expressed as a function of the detuning, following application of a microwave field of 2.4 μs duration. As is evident from the figure, a detuning of ∼400 kHz leads to the rapid transfer of population from the $|58s\rangle$ state to the neighboring strongly-coupled $|59s\rangle$ and $|60s\rangle$ states. (On the short timescale chosen, very little transfer to other lattice sites is seen.) The measurements are again in reasonable agreement with model predictions.

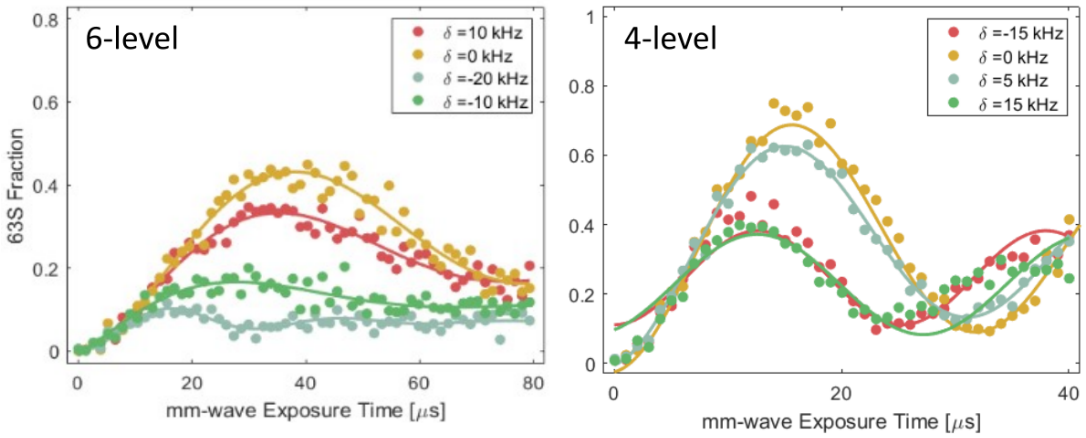

Figure 4.17 : Fraction of Rydberg population observed on the $|63s\rangle$ with the laser excitation initiating the atom on the $|58s\rangle$ state. The microwave detuning δ of the $|62s\rangle - |63s\rangle$ transition is being scanned around resonance.

4.3.3 AC Stark shift compensation

As emphasized above, most of the shown results rely on the assumption that each applied microwave tone is on resonance with its respective transition, i.e. $U_n = 0$. This is achieved by compensating the applied frequencies based on AC Stark shift measurements. Table 4.3 lists the AC Stark shifts measured on each involved Rydberg state due to each transitions at their respective microwave power settings that results in the topological regime of $J_1 = 160$kHz and $J_2 = 800$kHz. The measurements are carried out using the same method as in Section 3.2.3. Here I will describe the general process of calculating the required microwave frequency adjustment.

Taking the $|58s\rangle$-$|59s\rangle$ transition as an example, an intended resonant Rabi frequency of 164kHz is achieved at applied microwave frequency of 19638.360MHz as shown in Table 4.2. Since this is a two-photon transition, we may note

$$\nu_0 = 19638.360\,\text{MHz} * 2 = 39276.720\,\text{MHz} \tag{4.21}$$

where ν_0 is the microwave frequency, in Hz, corresponding to the Rabi resonance of

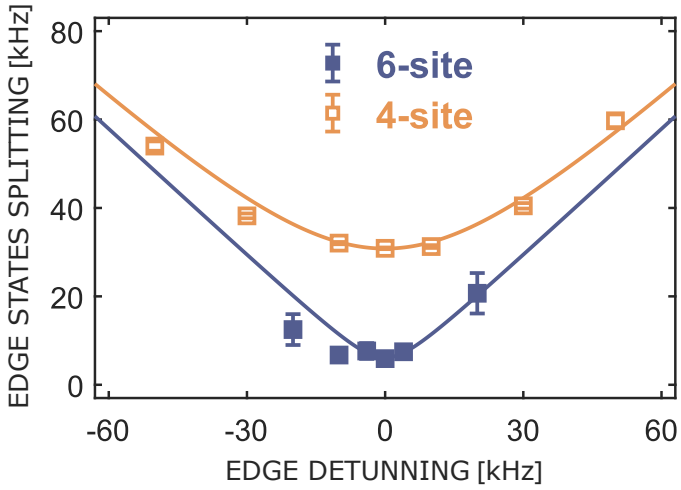

Figure 4.18 : Edge state energy splitting measured from the edge-to-edge tunneling rate as a function of the edge transition detuning. The solid lines show the calculated results.

the transition in the presence of only its own driving field. Now we consider how another applied microwave frequency changes this resonance frequency by shifting $|58s\rangle$ and/or $|59s\rangle$ states, i.e. the numbers in the first two rows in Table 4.3. For instance, the application of the $|59s\rangle$-$|60s\rangle$ transition shifts $|58s\rangle$ and $|59s\rangle$ by -316kHz and $+594$kHz respectively. Consequently, the resonance frequency of the $|58s\rangle$-$|59s\rangle$ transition will become

$$\nu_0^{'} \longrightarrow 39276.720\ \text{MHz} + 594\ \text{kHz} - (-316\ \text{kHz}) = 39277.630\ \text{MHz} \tag{4.22}$$

It should be noted that this calculation assumes that the AC Stark shift measurements of individual transitions are decoupled, i.e. measured values in Table 4.3 are unaffected by the presence of other frequencies. This should, to first order, be a good approximation.

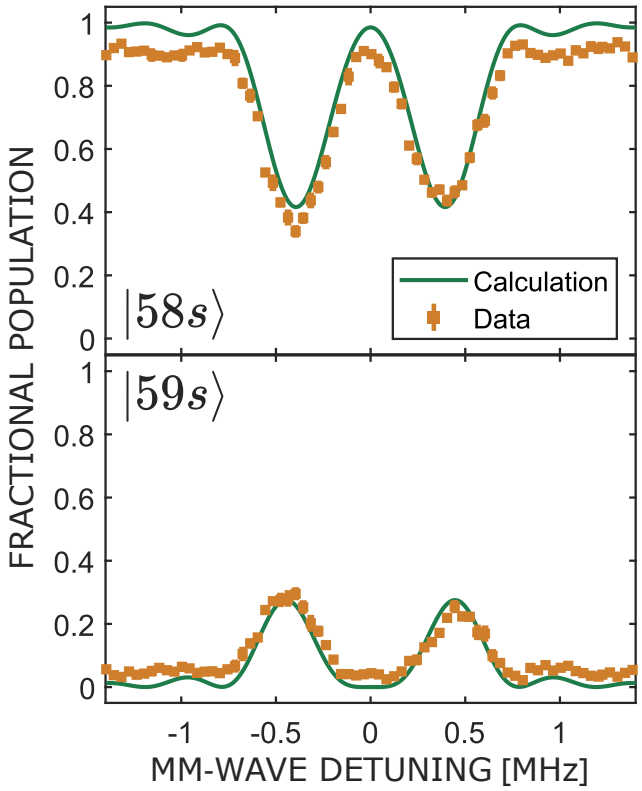

Figure 4.19 : Population transfer following initial population of the 58 $^3S_1$ "edge" state as a function of the detuning of the $|58s\rangle$-$|59s\rangle$ transition. The populations were measured 2.5 µs after turn-on of the microwave fields, at which time the majority of the population transfer is to the neighboring strongly coupled $|59s\rangle$ and $|60s\rangle$ states. The solid lines show the results of model simulations.

shift (kHz)	58s-59s (160 kHz)	59s-60s (800 kHz)	60s-61s (160 kHz)	61s-62s (800kHz)	62s-63s (160kHz)
58s	-68	-316	-10	-26	-4
59s	0	+594	-42	-48	-8
60s	-30	-876	+34	-160	-12
61s	-12	-228	-136	-290	-30
62s	-6	-74	-28	-62	-34
63s	-2	-36	-10	-154	-62

Table 4.3 : Measurements of AC Stark shifts experienced by each $5sns$ $^3S_1$ Rydberg states as caused by each S-S transition involved in the topological configuration (J_1 = 160kHz, J_2 = 800kHz) of the synthetic SSH lattice.

Similar calculation can be done to evaluate the change of $\nu_0^{(Rabi)}$ due to the rest of the transitions in Table 4.3, and this process gives a generalized formula for the final resonance frequency $\nu_0^{'}$ of the i-th transition in the presence of the entire Rydberg lattice as

$$\nu_0^{'} = \nu_0 + \sum_{j \neq i} [\Delta_u^{(j)} - \Delta_l^{(j)}] \tag{4.23}$$

where $\Delta_u^{(j)}$ ($\Delta_l^{(j)}$) is the AC Stark shift caused by the j-th transition on the upper (lower) level of the i-th transition. Note that the $j = i$ case is not being summed over because the shifts caused by the i-th transition itself have already been compensated at the initial resonance frequency ν_0 obtained by getting a balanced Autler-Townes splitting spectrum.

Transition	ν_0 (MHz)	$\nu_0^{'}$ (MHz)	$\nu_0^{'}$-ν_0 (kHz)
58S-59S	39276.720	39277.572	852
59S-60S	37212.880	37212.810	-70
60S-61S	35293.770	35294.288	518
61S-62S	33503.630	33503.894	264
62S-63S	31831.890	31831.858	-32

Table 4.4 : The resonance microwave frequencies (after doubling accounting for being two-photon transitions) before (ν_0) and after ($\nu_0^{'}$) applying the compensation calculated from AC Stark shifts.

Table 4.4 shows the corrected resonance frequency $\nu_0^{'}$ for all five transitions. As can be seen, the size of the corrections can be on the same order as the Rabi frequencies J_1, J_2. Because of uncertainties in the AC Stark shift measurements and possible microwave power fluctuations, $\nu_0^{'}$ are still not precisely the resonant frequencies. The

actual applied microwave frequencies are further more finely tuned, empirically based on trial and error, until the measured eigen-energy spectra as shown in Figure 4.12 matches the predictions.

4.4 Topological phase transition

(Content of this section follows, to a large extent, work presented in our published paper Ref.[90])

So far we have focused our study of the SSH Hamiltonian in the topological regime ($J_1/J_2 = 0.2 < 1$). We will now use the established schemes of probing the eigen-energy spectrum and measuring state dynamics and try to watch the emergence of the topological order when the tunneling rate ratio is varied across the critical point $J_1/J_2 = 1$. To this end, we prepared five different microwave power configurations resulting in in the following tunneling rates as shown in Table 4.5. where the con-

	Tunneling rates				
J_1 (kHz)	160	400	400	800	160
J_2 (kHz)	800	800	400	400	800
J_1/J_2	0.2	0.5	1	2	5

Table 4.5 : Configurations of tunneling rates used to study the topological phase transition in the SSH lattice. The ratio J_1/J_2 is scanned across the critical point $J_1/J_2 = 1$.

figuration of $J_1/J_2 = 0.2$ is the topologically non-trivial regime that we have already inspected above.

For each J_1, J_2 configuration, the AC Stark shifts caused by all the involved transitions are characterized and used to adjust the microwave frequencies to achieve

the resonance condition $U_n = 0$. As discussed above, the frequencies are then finely tuned such that the measured eigen-energy spectra match that of calculated. Figure

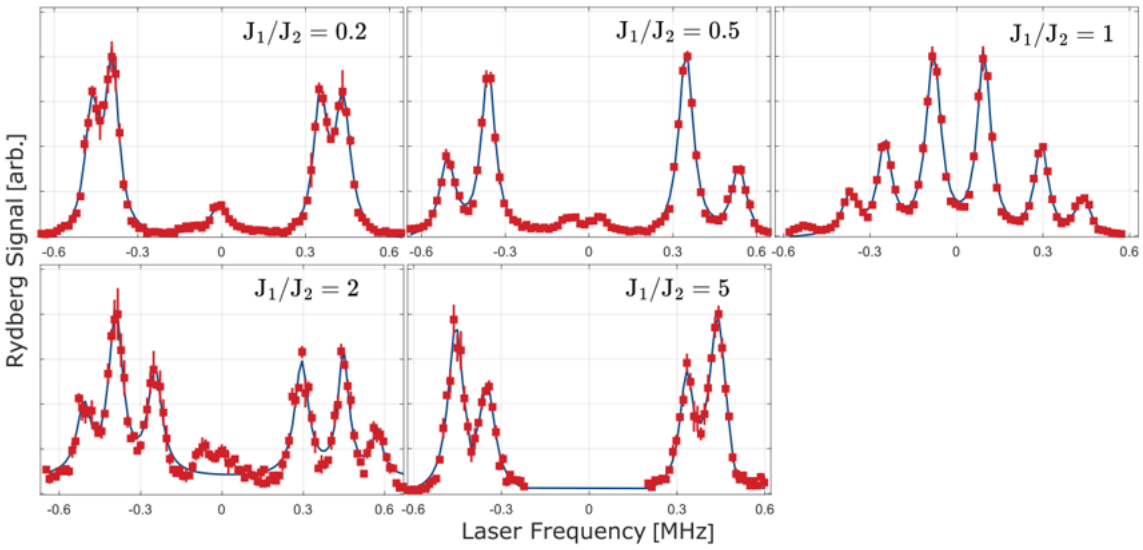

Figure 4.20 : Eigen-energy spectra of the SSH lattice at different tunneling rates J_1, J_1. At each configuration, we pick a bare Rydberg state $|n_i\rangle$ around which the excitation spectrum is taken and plotted here. The spectra are fit to Lorentzian lineshape with appropriate number of peaks, and the eigen-energies can be extracted from the fit parameters. In the data of $J_1/J_2 = 2$, the signals present at the center of the spectrum are believed to be Rydberg molecule excitation.

4.20 shows representative spectra all of which are fit to multiple Lorentzian lines, where the height of each peak gives the integrated line-strength which represents the contribution from each eigen-state. The eigen-energies are extracted from the fit peak positions and are plotted as a function of the tunneling ratio J_1/J_2 in Figure 4.21. The measured results agree well with the calculated results despite the uncertainties in the tunneling rates and microwave frequencies.

Measurements of the eigen-energies essentially constitute a rough characterization of the band structure of which the coarseness depend on the number of synthetic sites involved. At small values of J_1/J_2 the middle two eigen-states are (quasi)-

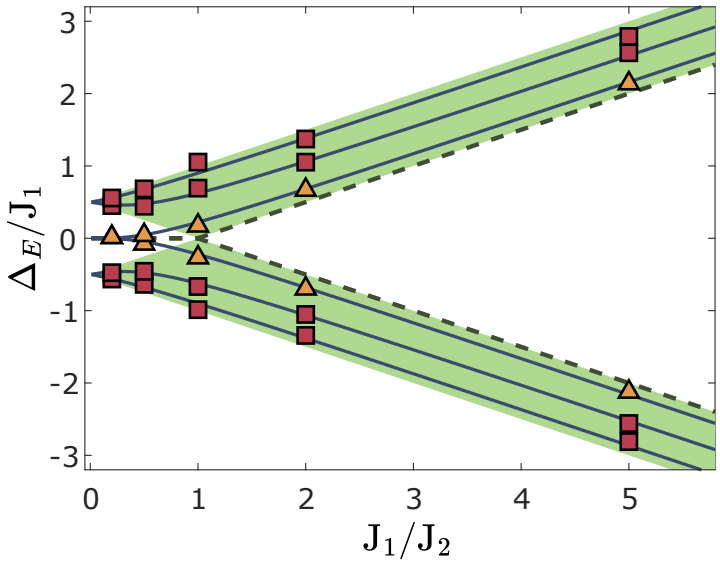

Figure 4.21 : The eigen-energies (in units of the tunneling rate J_1) measured from the peak positions (Δ_E) in the Lorentzian fits of the Rydberg excitation spectra at different tunneling ratios J_1/J_2. The triangles and squares denote the edge (at small J_1/J_2) and bulk states, respectively, and the solid lines show the calculated results (same as in Figure 4.5). Uncertainties in measured eigen-energies are small compared to size of the markers. At $J_1/J_2 = 0.2$, the two edge states become nearly degenerate (with 6 kHz energy spacing), and only one peak is resolved in the spectrum. The shaded region indicates the calculated energy bands for an infinitely long lattice, the dashed lines the two innermost eigen-states.

degenerate at zero energy, indicating the existence of topologically protected edge states energetically located at the center of the band gap. The phase transition that occurs as J_1/J_2 increases past one is clearly seen through the disappearance of the edge states and the opening of a band gap. Note that in the measured results, the critical point (where the two middle eigen-states meet at zero energy) occurs at a tunneling ratio $J_1/J_2 \approx 0.3$ as a result of the finite size (6 sites) of the experimental system. As is indicated in Figure 4.21, for an infinitely long lattice, the phase transition occurs exactly at the expected tunneling ratio $J_1/J_2 = 1$.

Chiral displacement

The sets of microwave frequencies and amplitudes finalized for each tunneling ratio J_1/J_2 in the spectral measurements are then used to measure the state dynamics. Figure 4.22 shows the results for tunneling ratio of $J_1/J_2 = 800\text{kHz}/160\text{kHz} = 5$. Here

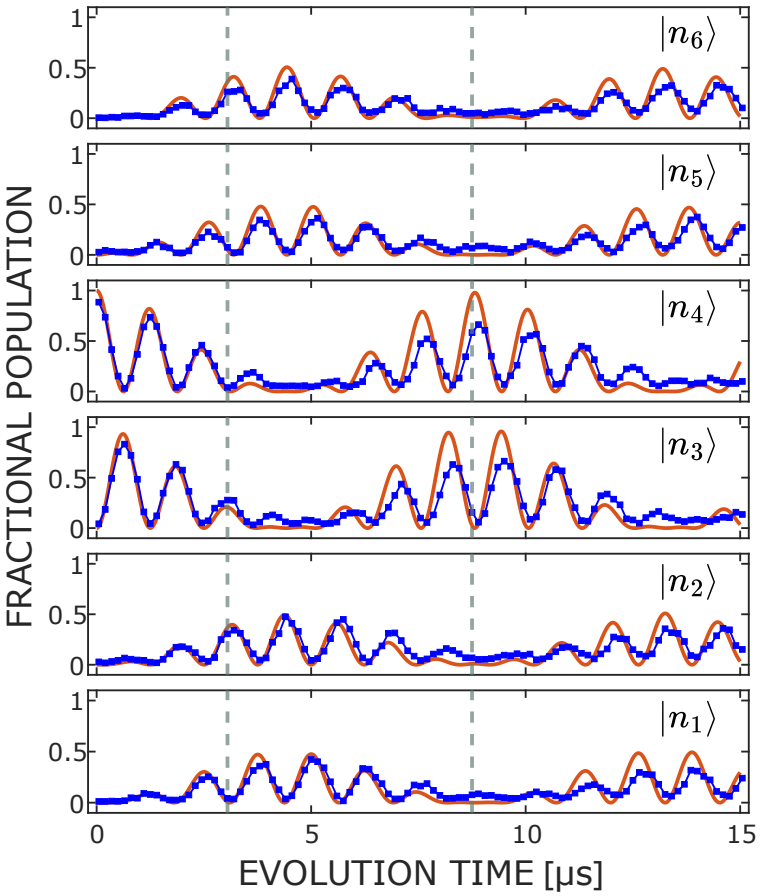

Figure 4.22 : Full state composition dynamics with the Rydberg population initiated on the fourth state $|n_4\rangle$ in the topologically trivial regime of $J_1/J_2 = 800\text{kHz}/160\text{kHz} = 5$.

the initially localized probability distribution diffuses into all other Rydberg sites as expected. The significant amount of population that tunnels into the two outermost sites particularly demonstrates that the system is in the topologically trivial phase.

Assessment of which topological phase the SSH system is in, however, does not necessarily rely on qualitatively inspecting the existence of protected edge states. For a 1D chiral system such as that described by our SSH Hamiltonian, a chiral operator $\hat{\Gamma}$ can be defined in the block-diagonal form

$$\hat{\Gamma} = \begin{pmatrix} \mathbb{1} & 0 \\ 0 & -\mathbb{1} \end{pmatrix} \tag{4.24}$$

where the two identity matrices run through the sublattices A and B, as defined in Figure 4.2. It has been shown [125] that the expectation value of a composite 'chiral position' operator $\langle \hat{\Gamma} \cdot \hat{m} \rangle$, with $\hat{m}$ being the unit cell operator, reveals the system winding number $\mathcal{W}$ via the bulk dynamics. Specifically, with the initial population localized on a single site in the standard SSH model, $\langle \hat{\Gamma} \cdot \hat{m} \rangle = \mathcal{W}/2 + ...$, where ... denotes oscillating terms that are averaged out in the long-time limit. For convenience, going forward we will define the mean chiral displacement value as $C(t) = 2 \langle \hat{\Gamma} \cdot \hat{m} \rangle$ such that $C(t) \cong \mathcal{W}$ at late times. For our 6-state SSH lattice, we have

$$\hat{\Gamma} = \begin{pmatrix} 1 & 0 & 0 & 0 & 0 & 0 \\ 0 & -1 & 0 & 0 & 0 & 0 \\ 0 & 0 & 1 & 0 & 0 & 0 \\ 0 & 0 & 0 & -1 & 0 & 0 \\ 0 & 0 & 0 & 0 & 1 & 0 \\ 0 & 0 & 0 & 0 & 0 & -1 \end{pmatrix}, \; \hat{m} = \begin{pmatrix} 1 & 0 & 0 & 0 & 0 & 0 \\ 0 & 1 & 0 & 0 & 0 & 0 \\ 0 & 0 & 2 & 0 & 0 & 0 \\ 0 & 0 & 0 & 2 & 0 & 0 \\ 0 & 0 & 0 & 0 & 3 & 0 \\ 0 & 0 & 0 & 0 & 0 & 3 \end{pmatrix} \tag{4.25}$$

which leads to

$$C(t) = 2 \langle \hat{\Gamma} \cdot \hat{m} \rangle = \mathcal{W} + \cdots \tag{4.26}$$

$$= 2(P_1 - P_2 + 2P_3 - 2P_4 + 3P_5 - 3P_6) \tag{4.27}$$

where P_i is the probability of being in the i-th bare Rydberg state. This can be directly evaluated from the measured population dynamics.

Figure 4.23(a-b) show the mean chiral displacement $C(t)$ evaluated from the dynamics data for $J_1/J_2 = 5$ and $J_1/J_2 = 0.2$ respectively. The measured values of $C(t)$ agree reasonably well with theoretical predictions obtained from direct diagnolization of the Hamiltonian. The dynamics of $C(t)$ show oscillatory behavior as expected. In order to average out the oscillating terms in $C(t)$, the cumulative time average, i.e., the average over all past time $\overline{C}(t) = 1/t \cdot \int_0^t C(t')\, dt'$, is taken and plotted in Figure 4.23(c).

The oscillations present in $C(t)$, and in the original population dynamics, have characteristic periods naturally determined by the tunneling rates J_1, J_2, each of which has an associated time scale $\tau_w = 1/J_w$ and $\tau_s = 1/J_s$, with J_w, J_s being the weaker and stronger of J_1, J_2, respectively. The measurements of $C(t)$ for the two different tunneling ratios $J_1/J_2 = 0.2$ and 5 share exactly opposite strong/weak Rabi frequencies. As indicated by the vertical dashed lines in Figure 4.23(c), the initial transient, which is determined by the initially localized state, is quickly averaged out within $t \simeq \tau_s$. Beyond the weak-tunneling time scale $t \gtrsim \tau_w$, most of the oscillations in $\overline{C}(t)$ have died out, and $\overline{C}(t)$ converges to 0 or 1, which is consistent with the expected values of winding number for the trivial ($J_1/J_2 = 5$) and topological ($J_1/J_2 = 0.2$) phases, respectively.

Measurements of $C(t)$ and the time average $\overline{C}(t)$ are repeated for five different tunneling ratios J_1/J_2 with the same range of evolution times $t = 0 - 15\,\mu s$. At each ratio, we take the final ($t = 15\,\mu s$) value of $\overline{C}(t)$ as the long-time average of $C(t)$, i.e., we approximate $\overline{C}(t \to \infty) \approx \overline{C}(t = 15\mu s)$. The averaging time is longer than the characteristic times τ_w, τ_s for any of the tunneling rates used here such that most of

the oscillatory behaviors have died out at $t = 15\mu s$ as shown in Figure 4.24.

The measured values of $\overline{C}(t)$ are plotted in Figure 4.25 as a function of the tunneling ratio. The long-time limit of the chiral displacement $C(t)$, which provides a measure of the system winding number $\mathcal{W}$, exhibits a clear transition from 0 to 1 as the tunneling ratio J_1/J_2 decreases through one, further demonstrating the trivial-to-topological phase transition seen in the eigen-energy spectrum. As a result of the finite size (6 sites) of our experimental system, the data points exhibit a smooth crossover near the critical point $J_1/J_2 = 1$ rather than the step function expected in the case of an infinitely long chain.

The data points and calculations are further categorized in Figure 4.25 into groups with different J_1 (160 kHz, 400 kHz, 800 kHz). In particular, the theoretical calculations at the three values of J_1 share a common general trend with which the measured data points agree reasonably well. The value of $\overline{C}(t)$, as obtained from time averaging $C(t)$, generally depends on both the characteristic periods τ_w, τ_s (equivalently J_w, J_s) and the averaging time. Since the latter is fixed at 15 µs, changes in τ_w, τ_s lead to variations in the number of periodic oscillations that are being averaged over. This is reflected in the smaller oscillation amplitudes in the calculated curves in Figure 4.25 as the tunneling rates increase. At $J_1 = 800$ kHz, the calculated curve is already relatively smooth with only small oscillations as the long-time limit is approached, demonstrating that cumulative averaging efficiently extracts the winding number from the chiral displacement measurements.

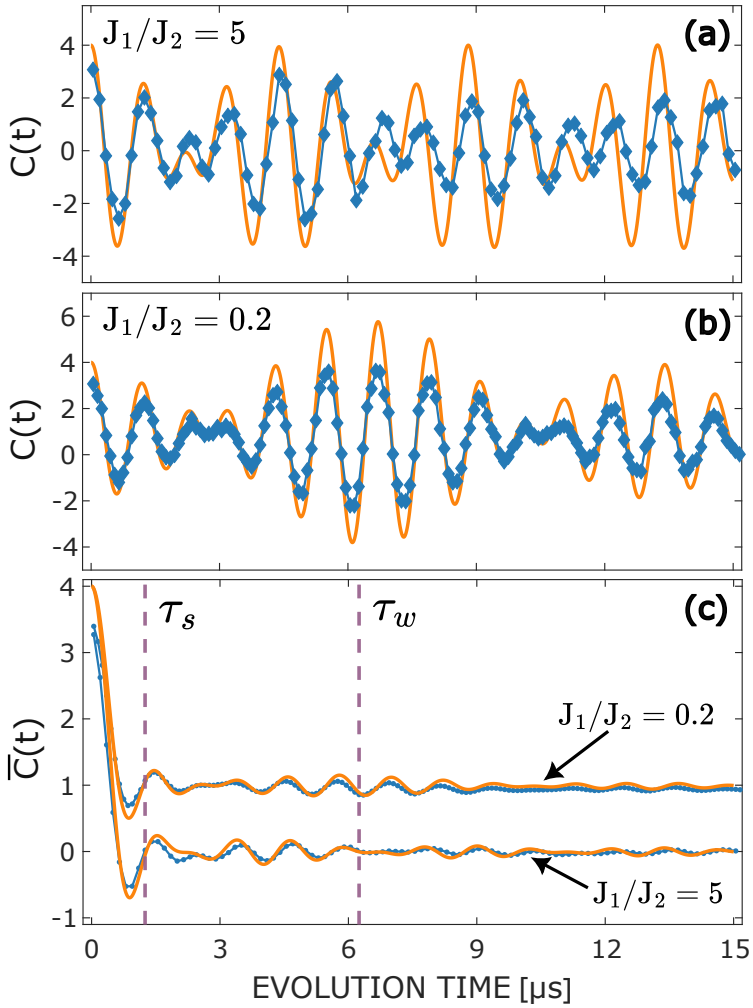

Figure 4.23 : (a-b) Mean chiral displacement $C(t)$ as a function of the evolution time t , comparing theoretical calculations (solid orange curves) and experimental results (connected blue dots) for (a) $J_1/J_2 = 800\,\text{kHz}/160\,\text{kHz} = 5$ and (b) $J_1/J_2 = 160\,\text{kHz}/800\,\text{kHz} = 0.2$. (c) The cumulative average $\overline{C}(t)$ for the two tunneling ratios. Vertical dashed lines mark the characteristic periods τ_w, τ_s corresponding to the tunneling rates (see text.) Measurement uncertainties of the chiral displacement shown here are small compared to the size of data markers.

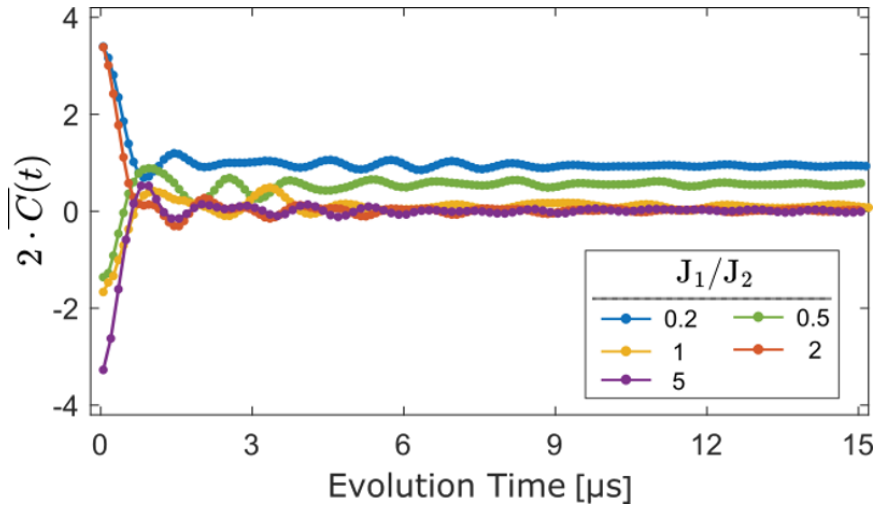

Figure 4.24 : Cumulative averaged results $\overline{C}(t)$ of the chiral displacement for each of the five tunneling ratios. The final value $\overline{C}(t = 15\mu s)$ in each curve is taken as a measurement of long-time average value $\overline{C}(t \to \infty)$.

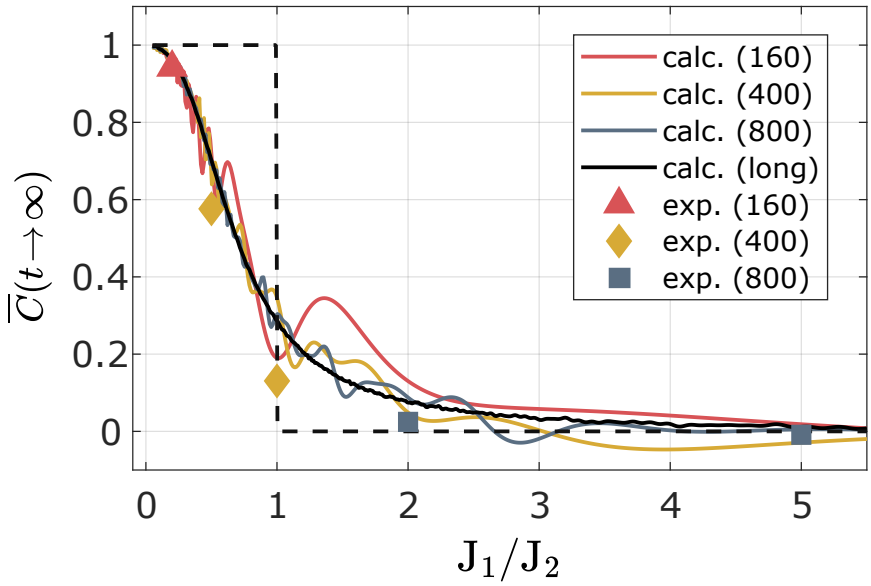

Figure 4.25 : The long-time average of the mean chiral displacement $\overline{C}(t \to \infty) \approx \overline{C}(t = 15\ \mu s)$ as a function of the tunneling ratio J_1/J_2. The symbols show the measured results obtained using the values of J_1 indicated in parentheses. Measurement uncertainties are small compared to the symbols. The solid curves show the corresponding calculated values. The black solid line shows the limiting case of a very long-time average, and the dashed line is the ideal behavior expected for an infinitely long lattice.

Chapter 5

Conclusion

In this thesis work, we have demonstrated that Rydberg states provide a great platform for constructing synthetic dimension systems. Even in the single atom case, as of current, it has shown great versatility in that both state dynamics and eigen-energy measurements can be performed with straightforward microwave coupling schemes.

Specifically, we have constructed a six-site Su-Schrieffer-Heeger (SSH) model in the synthetic space comprised six $(5sns)\,{}^3S_1$ Rydberg levels with $n \sim 60$ in a single ^{84}Sr atom. We are able to realize the topological non-trivial phase in the SSH model via the existence of protected edge states, which manifest through eigen-states composition that can be probed both in a steady-state approach as well as dynamically. Noticeable results include bulk population oscillations and long-range edge-to-edge tunneling, both of which have been observed with good agreement with theoretical predictions in 4- and 6-site synthetic lattices.

The topological phase transition present in the SSH Hamiltonian has also been explored by measuring the eigen-energy spectrum and, through the mean chiral displacement, the winding number $\mathcal{W}$ evaluated from the bulk dynamics. The measured results map out a smooth phase transition of $\mathcal{W} = 0 \rightarrow 1$, indicating the loss of nontrivial topology as the tunneling rate ratio is changed across the critical point of $\mathrm{J}_1/\mathrm{J}_2 = 1$. In particular, it is shown that long-time averaging of the mean chiral displacement $\overline{C}(t)$ can provide a reliable measure of the winding number even for limited system size and sampling time, both of which can be limited in experimental

settings due to technical challenges and decoherence.

5.1 Future directions

The success with the SSH lattice demonstrates the potential of Rydberg synthetic dimensions to simulate and faithfully reproduce complex Hamiltonians. The experiences we have acquired on building the microwave sources and characterizing Rydberg transitions, particularly of their coherence properties and associated AC Stark shifts, lays the foundation for extending the current scheme to the realization of other interesting synthetic dimension systems. Here we briefly discuss possible directions of further studies.

5.1.1 Choosing transitions

As we have seen, properties of constituent Rydberg transitions can pose limiting factors for the construction of synthetic dimensions. Disregarding anomalies caused by microwave interference in the apparatus, the three most relevant quantities: coupling strength (Rabi frequency) $\Omega_R \propto n^2$, AC Stark shift $\Delta_{Stark} \propto n^7$ and coherence time (lifetime) $\tau \propto n^3$ all scale differently with quantum number n. While the Rabi frequency can usually be increased by simply raising the microwave intensity. As we move towards expanding the synthetic dimension (by adding Rydberg levels and/or creating more complex geometries), the system coherence time is bound to degrade, and it will become increasingly more cumbersome to fully characterize and compensate for the AC Stark shifts. This motivates exploring Rydberg transitions over a wider range of n. In particular, one may choose to work at higher n for longer coherence times, benefiting dynamics-type measurements. When that is not necessary, lower n can be favorable to suppress AC Stark shifts, potentially drastically reduce

the effort of tuning the entire synthetic lattice to resonant condition $U_n = 0$.

S-P transitions.

5.1.2 Complex lattice structures

Extension of the present experimental scheme to larger system using 8-10 Rydberg levels or more is straightforward. It is also possible, by directly coupling non-adjacent states, to form closed loops and plaquettes, which can create complex lattice geometries. Figure 5.1 shows two of the particular interesting models realizable within the S-P-D Rydberg manifold that have been inspected.

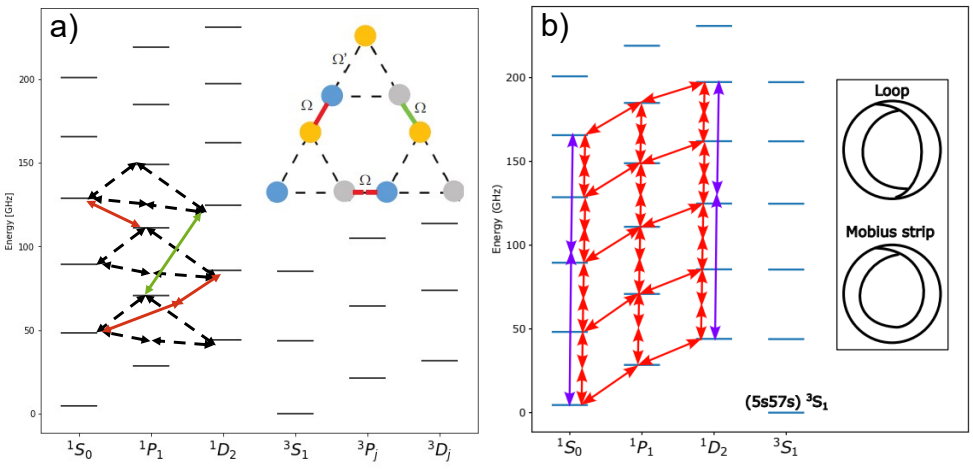

Figure 5.1 : Possible transition schemes for realizing the 2D Kagome lattice and the Mobius strip in Rydberg synthetic dimensions. Both proposed schemes involve only S, P and D Rydberg levels. Figure from Ref [6].

The breathing Kagome lattice is a tripartite model with three sites per unit cell with inter- and intra-cell tunneling rates Ω and Ω'. The Kagome model is predicted to possess topologically non-trivial order which manifests through the existence of protected corner states with probability distribution concentrated on the corners of the lattice, analogous to the edge states present in the SSH model. Therefore we

expect similar measurements of steady-state eigen-energy spectrum and population dynamics will reveal the protected corner states.

Still within the S-P-D manifold, a strip of Rydberg states can be formed by coupling all adjacent levels as illustrated by the red labeled transitions in Figure 5.1(b). The two ends of the strip are defined by the S and D states with lowest and highest quantum numbers n. A loop can be closed by connecting the lower and higher ends with long-range S-S and D-D two-photon transitions (purple labeled). Conversely, one may connect the ends diagonally by driving the S-D and D-S transitions instead. By doing this, the strip is essentially twisted before attached end-to-end, which results in the well known Möbius strip. Population dynamics measurements can give hints of this famous one-sided topology through phase evolution of wave-packets traversing the strip.

5.1.3 Rydberg-Rydberg interaction

As has been alluded to in Chapter 1, the real exciting potential of the Rydberg synthetic dimensions platform lies in its combination with the Rydberg-Rydberg interaction between individual atoms. For this purpose, a new apparatus in Killian lab has been under construction, where an optical tweezer system is being developed to form arrays of individual atoms, and the Rydberg states excitation and detection techniques will be incorporated. The general scheme is illustrated in Figure 5.2 showing that atoms trapped in their respective tweezer sites can all be prompted into the synthetic dimension consisting of the same Rydberg levels. When tweezer sites are brought closer, strength of the Rydberg-Rydberg interactions between atoms can get comparable to the tunneling rates between single-atom Rydberg levels connected by microwave transitions. This process couples the external space (tweezer sites)

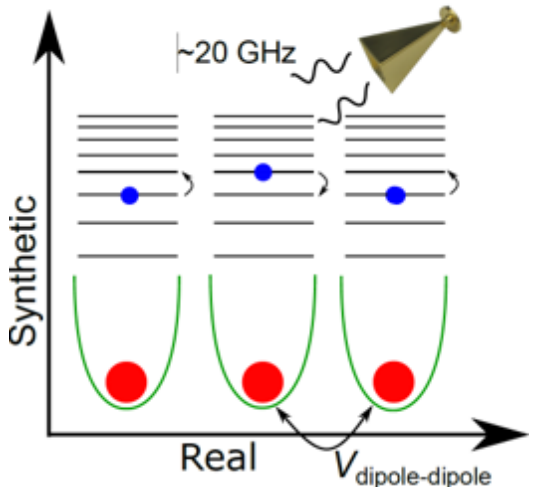

Figure 5.2 : Illustration of multi-atom Rydberg synthetic dimension systems.

with the internal degrees of freedom (synthetic lattice sites), thereby also making it a multi-atom system.

As an example, one of the first demonstrative experiments we propose to do in this scheme is to observe localized interactions in the synthetic dimension. Consider two atoms in adjacent tweezer sites and both excited into a same synthetic lattice connected by $S - P$ single photon transitions. When the atoms are in adjacent S-P states (such as $51S$ and $51P$ as shown in Figure 5.3), they interact strongly through the typical dipole-dipole potential in the form

$$V_{\text{dip}} = \frac{\mu^2_{ns,n'p}}{R^3} \tag{5.1}$$

where R is the inter-atomic distance, and the dipole matrix element $\mu^2_{ns,n'p}$ falls off rapidly with the difference $|n - n'|$. At small values of $|n - n'|$, $\mu^2_{ns,n'p}$ decreases by an order of magnitude for every unit increment of $|n - n'|$. Combined with the $1/R^3$ spatial dependence, V_{dip} can be thought of as a localized interaction that only couples states that are adjacent in both the real (tweezer sites) and synthetic (Rydberg levels)

space. In particular, for $R = 10\mu$m, which can be easily achieved between tweezer sites, and $n = n' \approx 50$ in strontium, we have $V_{\text{dip}}/h \sim 10$MHz. Consider that the

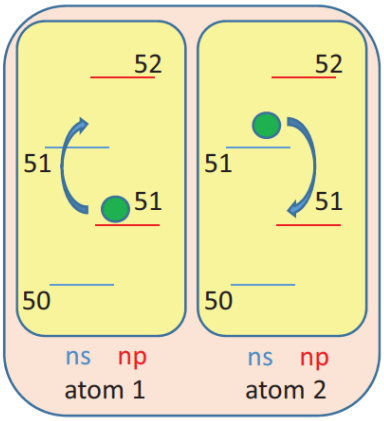

Figure 5.3 : Two atoms individually trapped in closely space ($\sim \mu$m) optical tweezer sites can interact strongly via dipole-dipole matrix element between adjacent $|ns\rangle$, $|np\rangle$ states.

Rydberg levels in the synthetic dimension coupled with an uniform tunneling rate J, one can initialize the states of the two atoms to be on opposite ends of the synthetic lattice and have their Rydberg wave-packets traversing the lattice and interact when arriving at neighboring S and P levels. When J $\ll V_{\text{dip}}$, this process resembles generic 1-dimensional collision in real space with localized interactions. We propose to study this synthetic-space collision and inspect its comparison with the real-space analogy.

Alternatively, we can achieve similar localized interactions with a synthetic lattice consisting of only S states. Normally, interactions between two atoms in the $|ns\rangle$ and $|n's\rangle$ states are in the van der Waals form of

$$V^{\text{vdW}}_{ns,n's} = \frac{C_{ns,n's}}{R^6} \tag{5.2}$$

where $C_{ns,n's}$ is much weaker and, more importantly, rather insensitive to $|n - n'|$. However, in the vicinity of Förster resonance, which happens when the two-atom

energy both in S-state is close to a P-state pair, i.e. $E(|ns, n's\rangle) \approx E(|n''p, n'''p\rangle)$, the interaction strength can get strongly enhanced by state mixing, and it crosses over to a $1/R^3$ dependence. Luckily, in strontium, it is predicted that there exists such a Förster resonance around n=50 for $|n - n'| = 2$ with rapid fall off with changes in $|n - n'|$. Based on these, we will also be exploring the possibility of collision-type experiments using S-state synthetic lattice, with which we can exploit the full state-resolving ionization detection used in the SSH experiments.

Appendix A

Laser Stabilization Setup Details

A.1 Cavity mirror specification

The specifications of the cavity mirrors are listed in detail in the order confirmation from SLS. Both mirror substrates are of 0.25" thickness and 1" diameter. The S1 surfaces have a super polished finish which results in a surface quality of 10-5, and the S2 surfaces have a surface quality of 20-10.

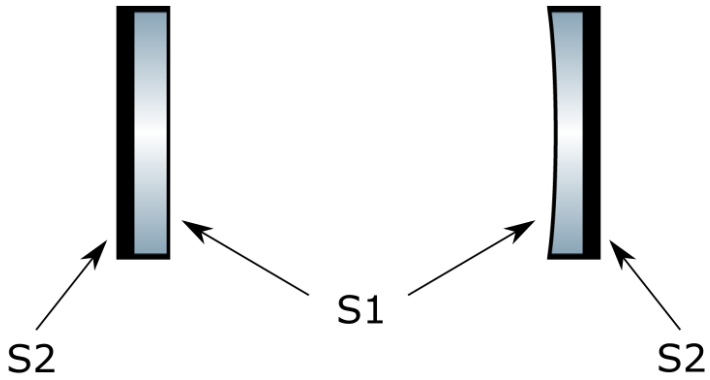

Figure A.1 : Illustration of the S1 and S2 surface of the cavity mirrors

The S1 surfaces are the ones that form the cavity, and they need to be highly reflective. SLS provided measurements on the transmission of the S1 surfaces at all three wavelengths as shown in Figure A.2. These numbers are used to calculate the cavity finesse in Table 2.3.

On the other hand, the S2 surfaces are supposedly anti-reflective to mitigate unwanted etalon effect building up between S1 and S2. The measurements on the reflection off the S2 surfaces are also provided and shown in Figure A.3. The reflection is below 0.2% for all three wavelengths.

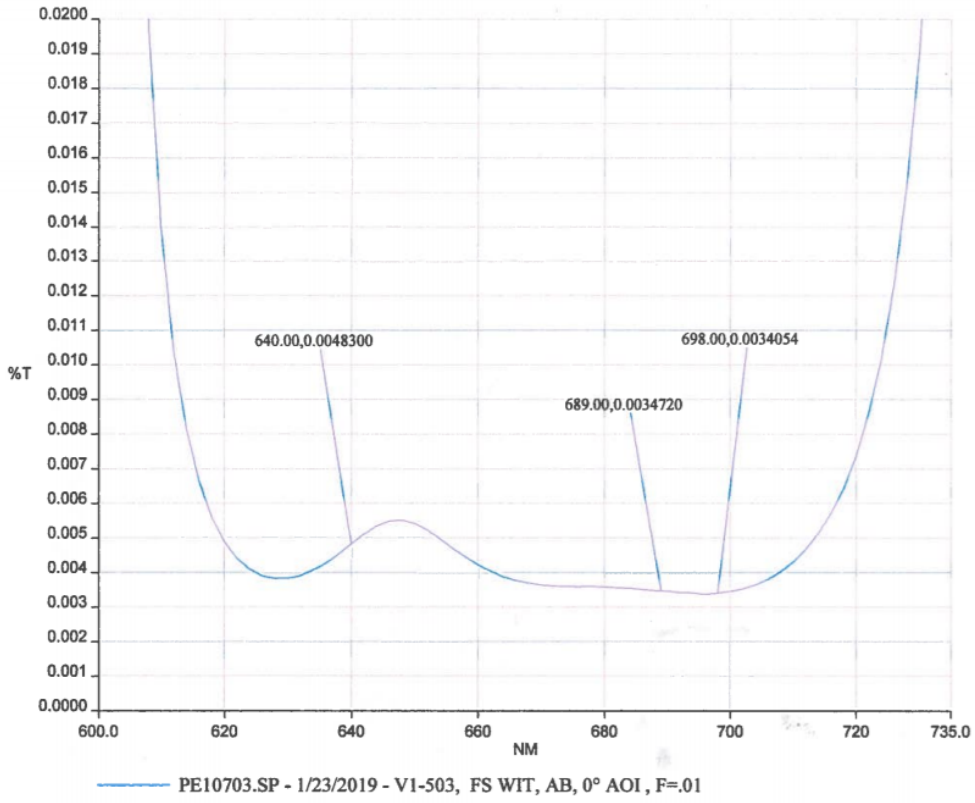

Figure A.2 : Measurements of the transmission of the S1 surfaces at 640 nm, 689 nm and 698 nm. Data from Stable Laser System, Inc.

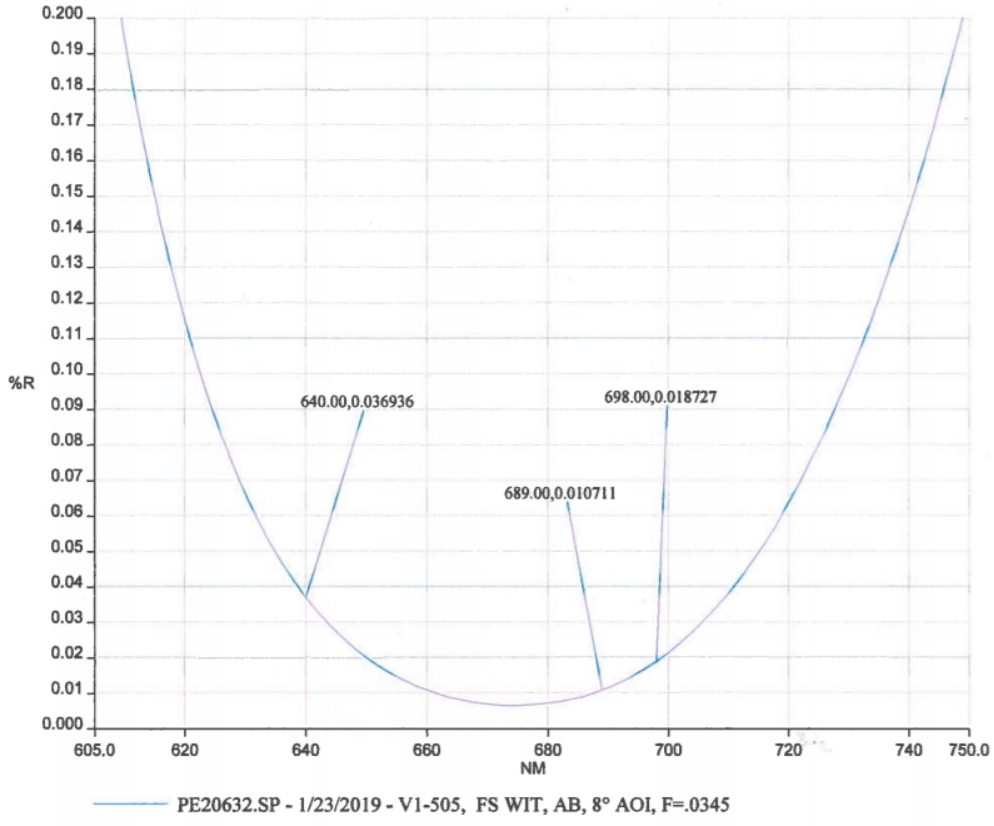

Figure A.3 : Measurements of the reflection off the S2 surfaces at 640 nm, 689 nm and 698 nm. Data from Stable Laser System, Inc.

A.2 Mode matching

To maximize the coupling efficiency of the input light into the cavity. The spatial profile of the input beam needs to resemble that of the cavity resonating mode. This is the process of mode matching. Ultimately, the purpose is to match the Gouy phase of the particular cavity mode so that the light interfere constructively between different round trips. Here we present the calculations for the process of mode matching the 689nm laser beam as an example.

The cavity mode profile can be calculated with the known cavity specifications. For the fundamental Gaussian mode (TEM00), which is what we almost always use, the beam waist is given by [127]

$$\omega_0^4 = (\frac{\lambda}{\pi})^2 \frac{d(R_1 - d)(R_2 - d)(R_1 + R_2 - d)}{(R_1 + R_2 - 2d)^2} \tag{A.1}$$

where R_1 and R_2 are the radius of curvature (ROC) of the two mirrors respectively with d being the mirror spacing. The formula gives the $1/e^2$ beam radius ω_0 at the waist. The waist can be located, in general, inside or out of the cavity, and its exact position can be calculated using

$$\begin{aligned} t_1 &= \frac{d(R_2 - d)}{R_1 + R_2 - 2d} \\ t_2 &= \frac{d(R_1 - d)}{R_1 + R_2 - 2d} \end{aligned} \tag{A.2}$$

where t_1 and t_2 are the distance between the waist and each of the mirror. For a plano-concave cavity as we have, the waist always sits exactly at the plano mirror, which comes out by simply having the corresponding ROC being infinite.

Using Equation A.1 and the known cavity geometry, the beam radius at waist of the cavity mode is calculated to be $\omega_0 = 209.4$ μm for 689 nm. In other words, to achieve mode matching, the input beam needs to have a waist exactly at the plano

mirror with a radius of 209.4 μm. As already shown in the bottom-left part of Figure 2.11, the light emitted by the laser is coupled into a fiber. After passing through the EOM, the light is out-coupled using the fiber output collimator in the cage system. The mode-matching lens then shapes the beam into the desired profile. To start with, one needs to know the initial profile of the output collimator. We picked Thorlabs TC06FC-633 triplet collimator for its superior beam quality (and its AR coating range which covers 689 nm). The collimator has a measured output profile as shown in Figure A.4. The beam shape is Gaussian and circular, allowing usage of a single

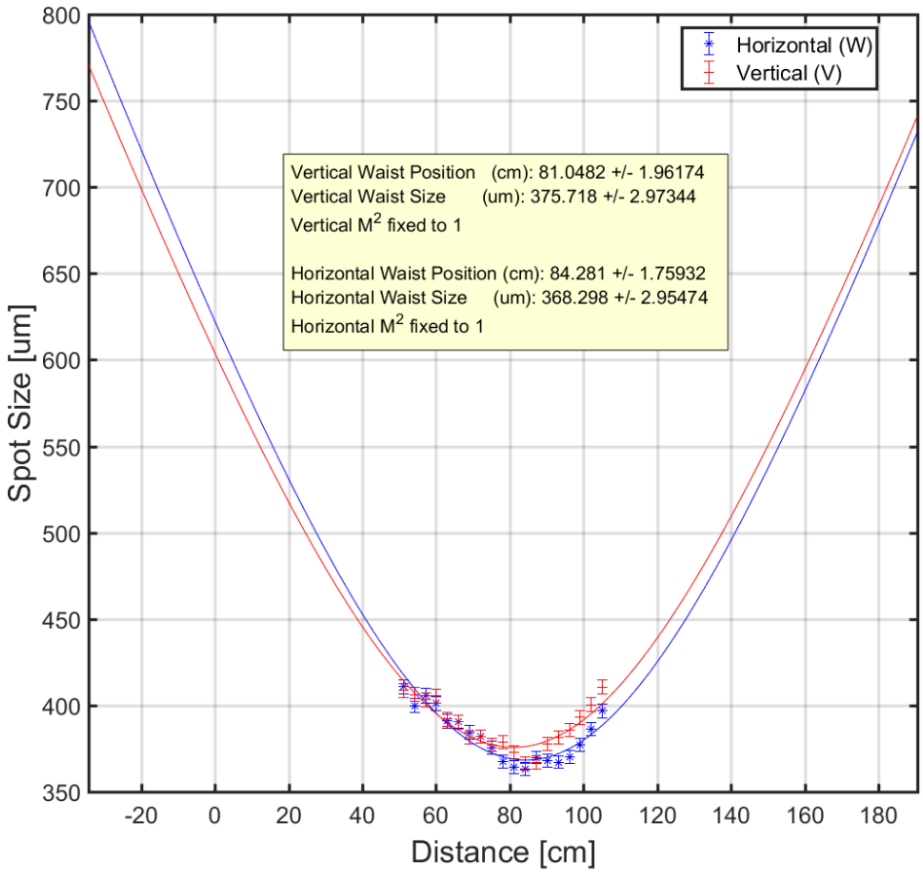

Figure A.4 : Measured output beam profile of the 689nm fiber collimator. The zero distance is referenced to the front face of the fiber collimator.

lens to achieve the mode matching. Figure A.5 shows the actual mode-matching

setup for 689 nm light with the relevant distances measured and labeled. Note that, as mentioned before, the precise location of the cavity is not known. However, by assuming that it sits exactly in the middle of the whole housing chamber, the distance from the cavity mirror surface to the front face of the housing chamber is estimated to be (261 mm - 100mm)/2 = 80.5mm. In other words, the beam waist needs to be placed 80.5mm inside the housing from the front face shown in the diagram.

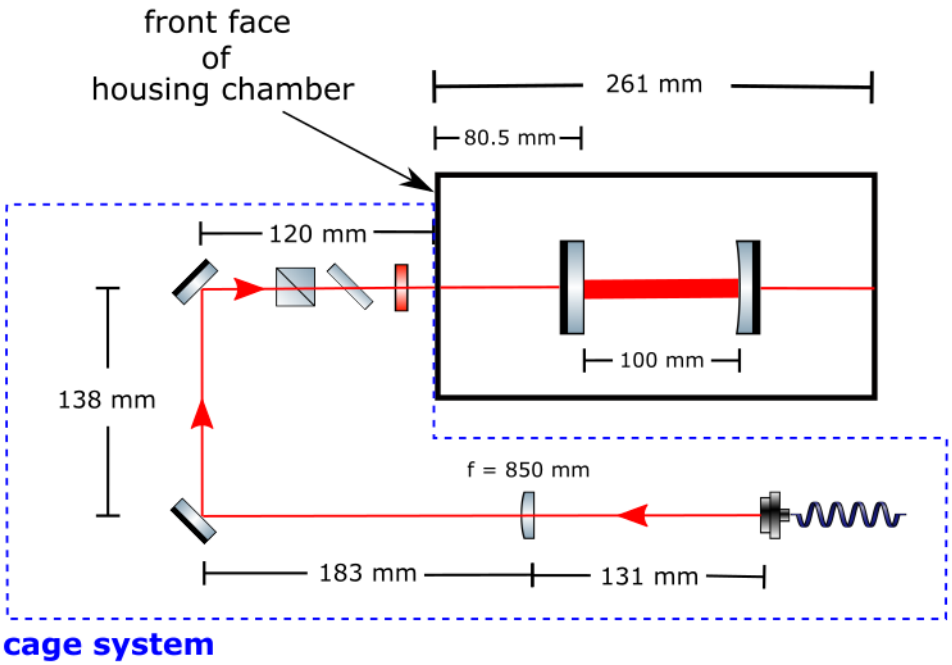

Figure A.5 : Path of the 689nm incident beam into the ULE cavity. The mode matching is done using a single lens with $f = 850$mm.

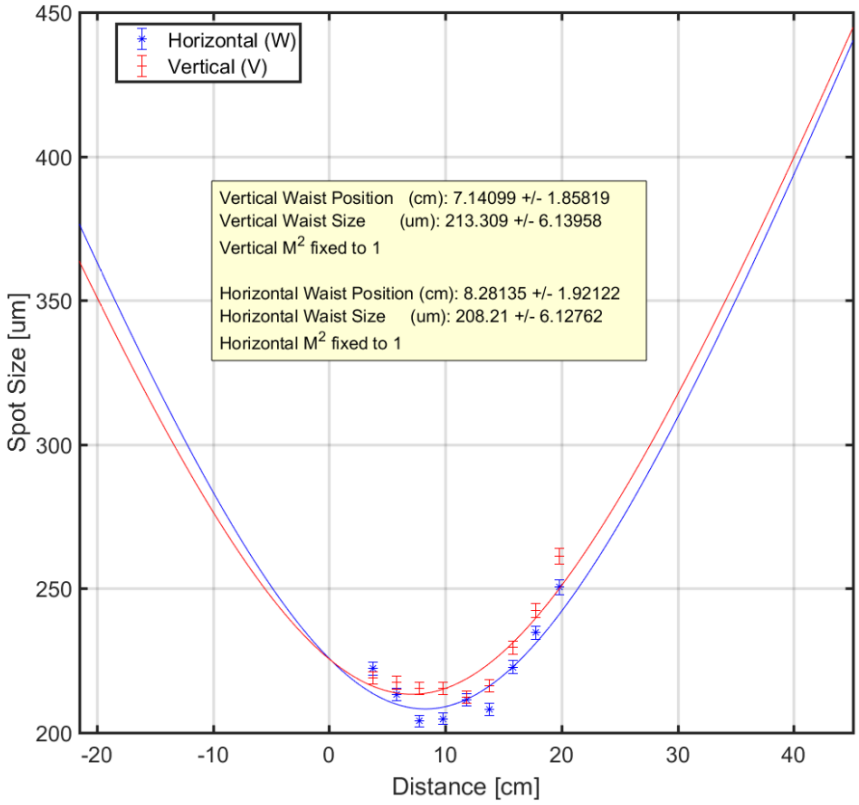

Figure A.6 : Measured final profile of the 689nm beam after all the optical elements before entering the ULE cavity vacuum housing. The zero distance is referenced to the window of the outer housing.

A.3 Ram

A.3.1 Origin of RAM

The RAM effect, as the name suggests, is modulation of the amplitude of the light as a by-product of the phase modulation. It mainly originates from the birefringence of the EOM crystal. While Wong and Hall [128] have given detailed analysis on this, here is a simple model demonstrating the process.

Since EOM crystals generally have two mutually orthogonal principle axes (namely fast and slow) with different value of V_π, when a RF signal is being applied to the EOM, polarizations along the two axes experience different modulation depth. Consider a beam of laser linearly polarized at an angle θ with respect to the fast axis of an EOM crystal. One can decompose the complex field amplitude after the modulation as

$$\tilde{\mathbf{E}} = \tilde{\mathbf{E}}_f \exp[i(\omega t + \beta_f \sin \Omega t)] + \tilde{\mathbf{E}}_s \exp[i(\omega t + \beta_s \sin \Omega t)] \tag{A.3}$$

where β_f and β_s are the modulation depth in the fast and slow axes respectively. It is assumed that the two modulations are in phase with the same frequency Ω. At any point in time, the real electric field amplitude is given by

$$\mathbf{E} = \mathbf{E}_f \cos(\omega t + \beta_f \sin \Omega t) + \mathbf{E}_s \cos(\omega t + \beta_s \sin \Omega t) \tag{A.4}$$

with resulting polarization axis at an angle θ' with respect to the fast axis

$$\theta' = \tan^{-1} \frac{E_s \cos(\omega t + \beta_s \sin \Omega t)}{E_f \cos(\omega t + \beta_f \sin \Omega t)} \tag{A.5}$$

The difference in β_f and β_s makes the polarization axis time dependent and oscillate at the modulation frequency Ω. After passing through the PBS before entering the

cavity, this oscillating polarization is translated into an amplitude modulation at frequency Ω of the transmitted light.

As discussed in section 2.3.1, the PDH error signal measures the phase information of the cavity reflection coefficient, and the phase information is carried by the signals oscillating at the modulation frequency Ω in the reflected beam intensity. Since the RAM has the same modulation frequency Ω, the mixer cannot distinguish between the two signals, leading to an offset on the PDH error signal after the demodulation.

A.3.2 Monitoring RAM

In principle, as long as the polarization is well aligned with the axis of the EOM crystal, the RAM effect can be mitigated. However, in practice, especially with fiber coupled EOM, the polarization can change in a temperature and stress-dependent way. This would cause RAM to produce fluctuating offset, which eventually becomes frequency fluctuations in the locked laser. Therefore, the RAM needs to be constantly monitored to see if the error signal is contaminated. The most straightforward way is by simply looking at the baseline on the PDH error signal. However, this only works when the laser lock is not engaged as the laser feedback would force the error signal to zero.

A separate monitoring system was thus built by sampling the beam before entering the cavity with a beam splitter as already shown in Figure 2.11 and A.5. This sampled beam is detected by a fast photodiode and then mixed with the 20 MHz PDH modulation signal. The idea is to reproduce the error signal but without the cavity information, which enables out-of-loop measurements of only the offset caused by RAM. Figure A.7 shows the corresponding optical and RF setup. The orange beam, which is used for measuring RAM, is sampled from the incident beam after passing the

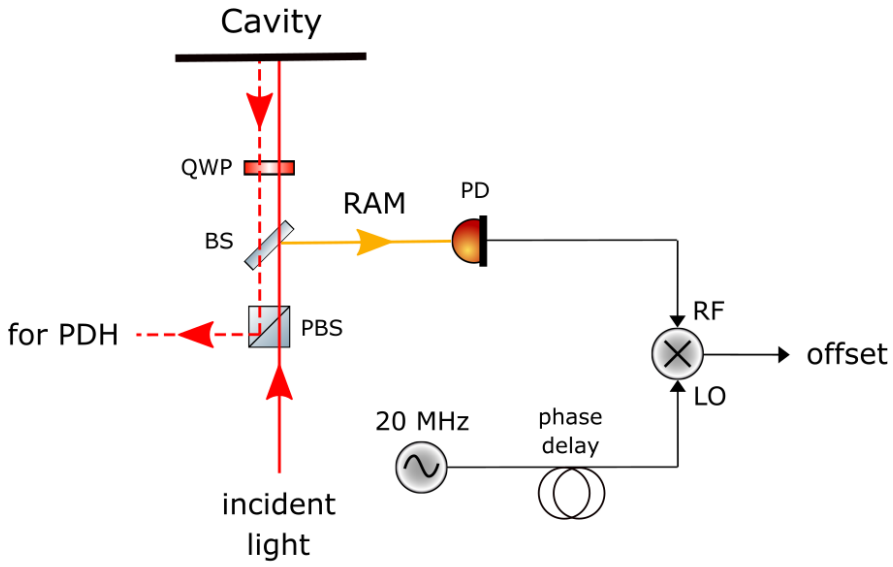

Figure A.7 : Setup for the out-of-loop RAM monitoring system. The orange arrow is the beam for RAM measurement, and the red dashed line is the cavity reflected light used for PDH error signal. The modulation frequency (20 MHz for 689 nm), attenuation and amplification (not shown here) and phase delay might differ between two wavelengths, but the general setup is common. QWP: quarter-wave plate, PBS: polarizing beam-splitter, BS: (plate) beam-splitter.

PBS so that it has the amplitude modulation but does not interact with the cavity. Since the transmission coefficient of the BS is generally polarization dependent, it should be placed before the QWP to ensure pure circular polarization after the QWP. The local oscillator (LO) signals for the mixer is provided by the same 20 MHz modulation source from the PDH signal unit through a RF splitter. The mixing needs to be phase-matched with that for the PDH error signal such that the offset measured here changes in phase (or 180° out of phase) with the offset on the error signal. This is done by adjusting the phase delay of the LO signal path by changing cable length. At 20 MHz, the phase shift per foot in coax cable is roughly 10°, making the length of cable needed manageable.

To verify the phase matching condition, one can manually change the RAM offset by rotating the polarization of the light going through the EOM or changing its temperature (or with DC bias voltage) and watch how offset from the RAM monitor and in the PDH error signal respond. Figure A.8 shows the two of them as I abruptly rotated a half wave plate before the light couples into the EOM fiber (in the middle

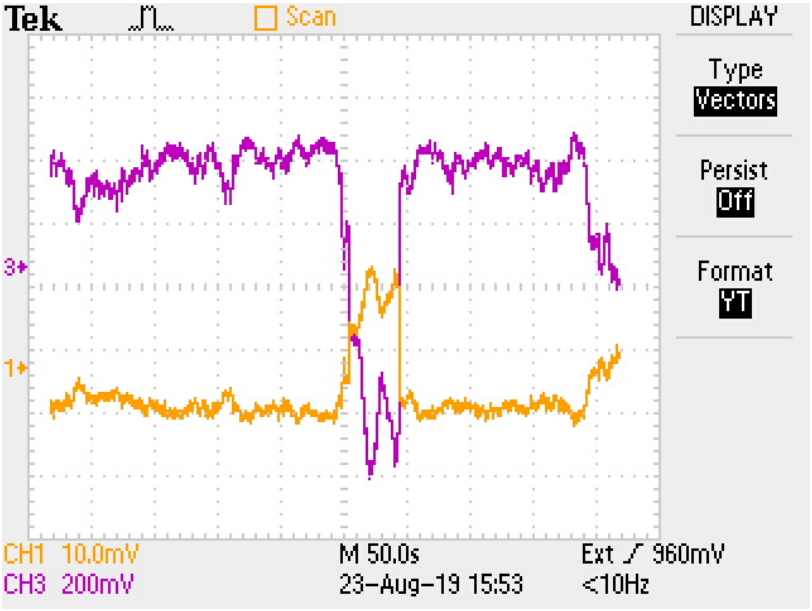

Figure A.8 : Scope traces showing the offset on the PDH error signal (Ch3) and measured from the RAM monitoring setup (Ch1) demonstrating proper phase match. This is done with 640 nm light on the AdvR EOM.

of the traces) and changed the set point of the temperature controller for the EOM (towards the end). The laser was far off resonance from any significant cavity mode, so the PDH error signal has no visible cavity peaks. It is clear that the measurements from the RAM monitoring system closely represents the behavior of the offset on the error signal by staying almost exactly 180° out of phase.

For 689 nm, it seems that the offset is relatively stable. The ratio between the offset and the peak-to-peak size of the error signal, which is what ultimately determines

the frequency deviation of the locked laser from the cavity resonance, is typically close to the example shown in Figure 2.17. The laser has not been unlocked due to the RAM offset, and we can manually adjust the offset simply using a trim-pot on the FALC module.

Bibliography

[1] J. D. Whalen, *Probing nonlocal correlations with ultralong-range Rydberg molecules*. PhD thesis, Rice University, June 2021.

[2] F. Camargo, *Rydberg Molecules and Polarons in Ultracold Strontium Gases*. PhD thesis, Rice University, June 2017.

[3] N. Batra and G. Sheet, "Understanding Basic Concepts of Topological Insulators Through Su-Schrieffer-Heeger (SSH) Model," 2019.

[4] S. K. Kanungo, J. D. Whalen, Y. Lu, M. Yuan, S. Dasgupta, F. B. Dunning, K. R. A. Hazzard, and T. C. Killian, "Realizing topological edge states with Rydberg-atom synthetic dimensions," *Nat. Comm.*, vol. 13, p. 972, Feb. 2022.

[5] Y. Lu, C. Wang, S. K. Kanungo, S. Yoshida, F. B. Dunning, and T. C. Killian, "Wave-packet dynamics and long-range tunneling within the Su-Schrieffer-Heeger model using Rydberg-atom synthetic dimensions," *Phys. Rev. A*, vol. 109, p. 032801, Mar. 2024.

[6] S. K. Kanungo, *Rydberg-atom synthetic dimensions*. PhD thesis, Rice University, Aug. 2022.

[7] R. A. Brienza, Y. Lu, C. Wang, S. K. Kanungo, T. C. Killian, F. B. Dunning, J. Burgdörfer, and S. Yoshida, "Microwave spectroscopy of low-l singlet strontium Rydberg states at intermediate $n, 50 \lesssim n \lesssim 70$," *Phys. Rev. A*, vol. 108,

p. 022815, Aug. 2023.

[8] C. L. Vaillant, M. P. A. Jones, and R. M. Potvliege, "Long-range Rydberg–Rydberg interactions in calcium, strontium and ytterbium," *J. Phys. B At. Mol. Opt. Phys.*, vol. 45, p. 135004, July 2012.

[9] R. Ding, *Spectroscopy of ^{87}Sr Rydberg Atoms and Molecules*. PhD thesis, Rice University, Sept. 2019.

[10] J. Rydberg, "XXXIV. On the structure of the line-spectra of the chemical elements," *The London, Edinburgh, and Dublin Philosophical Magazine and Journal of Science*, vol. 29, no. 179, pp. 331–337, 1890.

[11] T. F. Gallagher, *Rydberg atoms*. Cambridge University Press, 2005.

[12] A. Browaeys and T. Lahaye, "Many-body physics with individually controlled Rydberg atoms," *Nature Physics*, vol. 16, pp. 132–142, Jan. 2020.

[13] P. Scholl, M. Schuler, H. J. Williams, A. A. Eberharter, D. Barredo, K.-N. Schymik, V. Lienhard, L.-P. Henry, T. C. Lang, T. Lahaye, A. M. Läuchli, and A. Browaeys, "Quantum simulation of 2D antiferromagnets with hundreds of Rydberg atoms," *Nature*, vol. 595, p. 233–238, July 2021.

[14] H. Labuhn, D. Barredo, S. Ravets, S. de Léséleuc, T. Macrì, T. Lahaye, and A. Browaeys, "Tunable two-dimensional arrays of single Rydberg atoms for realizing quantum Ising models," *Nature*, vol. 534, p. 667–670, June 2016.

[15] M. D. Lukin, M. Fleischhauer, R. Cote, L. M. Duan, D. Jaksch, J. I. Cirac, and P. Zoller, "Dipole Blockade and Quantum Information Processing in Mesoscopic Atomic Ensembles," *Phys. Rev. Lett.*, vol. 87, p. 037901, June 2001.

[16] E. Urban, T. A. Johnson, T. Henage, L. Isenhower, D. D. Yavuz, T. G. Walker, and M. Saffman, "Observation of Rydberg blockade between two atoms," *Nature Physics*, vol. 5, p. 110–114, Jan. 2009.

[17] M. Saffman, T. G. Walker, and K. Mølmer, "Quantum information with Rydberg atoms," *Rev. Mod. Phys.*, vol. 82, pp. 2313–2363, Aug. 2010.

[18] M. Saffman, "Quantum computing with atomic qubits and Rydberg interactions: progress and challenges," *Journal of Physics B: Atomic, Molecular and Optical Physics*, vol. 49, p. 202001, Oct. 2016.

[19] L. I. R. Gil, R. Mukherjee, E. M. Bridge, M. P. A. Jones, and T. Pohl, "Spin Squeezing in a Rydberg Lattice Clock," *Phys. Rev. Lett.*, vol. 112, p. 103601, Mar. 2014.

[20] J. A. Hines, S. V. Rajagopal, G. L. Moreau, M. D. Wahrman, N. A. Lewis, O. Marković, and M. Schleier-Smith, "Spin Squeezing by Rydberg Dressing in an Array of Atomic Ensembles," *Phys. Rev. Lett.*, vol. 131, p. 063401, Aug. 2023.

[21] C. S. Adams, J. D. Pritchard, and J. P. Shaffer, "Rydberg atom quantum technologies," *Journal of Physics B: Atomic, Molecular and Optical Physics*, vol. 53, p. 012002, Dec. 2019.

[22] L. Pezzè, A. Smerzi, M. K. Oberthaler, R. Schmied, and P. Treutlein, "Quantum metrology with nonclassical states of atomic ensembles," *Rev. Mod. Phys.*, vol. 90, p. 035005, Sept. 2018.

[23] J. D. Whalen, S. K. Kanungo, R. Ding, M. Wagner, R. Schmidt, H. R. Sadeghpour, S. Yoshida, J. Burgdörfer, F. B. Dunning, and T. C. Killian, "Probing

nonlocal spatial correlations in quantum gases with ultra-long-range Rydberg molecules," *Phys. Rev. A*, vol. 100, p. 011402, July 2019.

[24] Y. Lu, J. D. Whalen, S. K. Kanungo, T. C. Killian, F. B. Dunning, S. Yoshida, and J. Burgdörfer, "Resolving rotationally excited states of ultralong-range Rydberg molecules," *Phys. Rev. A*, vol. 106, p. 022809, Aug. 2022.

[25] T. Hänsch and A. Schawlow, "Cooling of gases by laser radiation," *Optics Communications*, vol. 13, pp. 68–69, Jan. 1975.

[26] K. Vogel, T. Dinneen, A. Gallagher, and J. Hall, "Narrow-line Doppler cooling of strontium to the recoil limit," *IEEE Transactions on Instrumentation and Measurement*, vol. 48, p. 618–621, Apr. 1999.

[27] A. Aeppli, K. Kim, W. Warfield, M. S. Safronova, and J. Ye, "Clock with 8×10^{-19} Systematic Uncertainty," *Phys. Rev. Lett.*, vol. 133, p. 023401, July 2024.

[28] G. Lochead, D. Boddy, D. P. Sadler, C. S. Adams, and M. P. A. Jones, "Number-resolved imaging of excited-state atoms using a scanning autoionization microscope," *Phys. Rev. A*, vol. 87, p. 053409, May 2013.

[29] S. R. Cohen and J. D. Thompson, "Quantum Computing with Circular Rydberg Atoms," *PRX Quantum*, vol. 2, p. 030322, Aug. 2021.

[30] J. T. Wilson, S. Saskin, Y. Meng, S. Ma, R. Dilip, A. P. Burgers, and J. D. Thompson, "Trapping Alkaline Earth Rydberg Atoms Optical Tweezer Arrays," *Phys. Rev. Lett.*, vol. 128, p. 033201, Jan. 2022.

[31] C. Hölzl, A. Götzelmann, E. Pultinevicius, M. Wirth, and F. Meinert, "Long-Lived Circular Rydberg Qubits of Alkaline-Earth Atoms in Optical Tweezers," *Phys. Rev. X*, vol. 14, p. 021024, May 2024.

[32] K. R. A. Hazzard and B. Gadway, "Synthetic dimensions," *Physics Today*, vol. 76, p. 62–63, Apr. 2023.

[33] R. P. Feynman, "Simulating physics with computers," *International Journal of Theoretical Physics*, vol. 21, p. 467–488, June 1982.

[34] "40 years of quantum computing," *Nat. Rev. Phys.*, vol. 4, pp. 1–1, Jan. 2022.

[35] T. H. Johnson, S. R. Clark, and D. Jaksch, "What is a quantum simulator?," *EPJ Quantum Technology*, vol. 1, July 2014.

[36] S. A. Wilkinson and M. J. Hartmann, "Superconducting quantum many-body circuits for quantum simulation and computing," *Applied Physics Letters*, vol. 116, June 2020.

[37] A. A. Houck, H. E. Türeci, and J. Koch, "On-chip quantum simulation with superconducting circuits," *Nature Physics*, vol. 8, p. 292–299, Apr. 2012.

[38] X. Zhang, E. Kim, D. K. Mark, S. Choi, and O. Painter, "A superconducting quantum simulator based on a photonic-bandgap metamaterial," *Science*, vol. 379, p. 278–283, Jan. 2023.

[39] I. Bloch, J. Dalibard, and S. Nascimbène, "Quantum simulations with ultracold quantum gases," *Nature Physics*, vol. 8, p. 267–276, Apr. 2012.

[40] F. Schäfer, T. Fukuhara, S. Sugawa, Y. Takasu, and Y. Takahashi, "Tools for quantum simulation with ultracold atoms in optical lattices," *Nature Reviews*

Physics, vol. 2, p. 411–425, July 2020.

[41] C. Gross and I. Bloch, "Quantum simulations with ultracold atoms in optical lattices," *Science*, vol. 357, p. 995–1001, Sept. 2017.

[42] C. Monroe, W. C. Campbell, L.-M. Duan, Z.-X. Gong, A. V. Gorshkov, P. W. Hess, R. Islam, K. Kim, N. M. Linke, G. Pagano, P. Richerme, C. Senko, and N. Y. Yao, "Programmable quantum simulations of spin systems with trapped ions," *Rev. Mod. Phys.*, vol. 93, p. 025001, Apr. 2021.

[43] R. Blatt and C. F. Roos, "Quantum simulations with trapped ions," *Nature Physics*, vol. 8, p. 277–284, Apr. 2012.

[44] A. Aspuru-Guzik and P. Walther, "Photonic quantum simulators," *Nature Physics*, vol. 8, p. 285–291, Apr. 2012.

[45] M. Greiner and S. Fölling, "Optical lattices," *Nature*, vol. 453, p. 736–738, June 2008.

[46] D. Jaksch, C. Bruder, J. I. Cirac, C. W. Gardiner, and P. Zoller, "Cold Bosonic Atoms in Optical Lattices," *Phys. Rev. Lett.*, vol. 81, pp. 3108–3111, Oct. 1998.

[47] M. Greiner, O. Mandel, T. Esslinger, T. W. Hänsch, and I. Bloch, "Quantum phase transition from a superfluid to a Mott insulator in a gas of ultracold atoms," *Nature*, vol. 415, p. 39–44, Jan. 2002.

[48] D. Jaksch and P. Zoller, "The cold atom Hubbard toolbox," *Annals of Physics*, vol. 315, p. 52–79, Jan. 2005.

[49] A. Mazurenko, C. S. Chiu, G. Ji, M. F. Parsons, M. Kanász-Nagy, R. Schmidt, F. Grusdt, E. Demler, D. Greif, and M. Greiner, "A cold-atom Fermi–Hubbard

antiferromagnet," *Nature*, vol. 545, p. 462–466, May 2017.

[50] M. Boll, T. A. Hilker, G. Salomon, A. Omran, J. Nespolo, L. Pollet, I. Bloch, and C. Gross, "Spin- and density-resolved microscopy of antiferromagnetic correlations in Fermi-Hubbard chains," *Science*, vol. 353, p. 1257–1260, Sept. 2016.

[51] L. W. Cheuk, M. A. Nichols, K. R. Lawrence, M. Okan, H. Zhang, E. Khatami, N. Trivedi, T. Paiva, M. Rigol, and M. W. Zwierlein, "Observation of spatial charge and spin correlations in the 2D Fermi-Hubbard model," *Science*, vol. 353, p. 1260–1264, Sept. 2016.

[52] R. A. Hart, P. M. Duarte, T.-L. Yang, X. Liu, T. Paiva, E. Khatami, R. T. Scalettar, N. Trivedi, D. A. Huse, and R. G. Hulet, "Observation of antiferromagnetic correlations in the Hubbard model with ultracold atoms," *Nature*, vol. 519, p. 211–214, Feb. 2015.

[53] P. N. Jepsen, J. Amato-Grill, I. Dimitrova, W. W. Ho, E. Demler, and W. Ketterle, "Spin transport in a tunable Heisenberg model realized with ultracold atoms," *Nature*, vol. 588, p. 403–407, Dec. 2020.

[54] M. J. Martin, M. Bishof, M. D. Swallows, X. Zhang, C. Benko, J. von Stecher, A. V. Gorshkov, A. M. Rey, and J. Ye, "A Quantum Many-Body Spin System in an Optical Lattice Clock," *Science*, vol. 341, p. 632–636, Aug. 2013.

[55] C. Chin, R. Grimm, P. Julienne, and E. Tiesinga, "Feshbach resonances in ultracold gases," *Rev. Mod. Phys.*, vol. 82, pp. 1225–1286, Apr. 2010.

[56] W. S. Bakr, J. I. Gillen, A. Peng, S. Fölling, and M. Greiner, "A quantum gas microscope for detecting single atoms in a Hubbard-regime optical lattice," *Nature*, vol. 462, p. 74–77, Nov. 2009.

[57] A. M. Kaufman and K.-K. Ni, "Quantum science with optical tweezer arrays of ultracold atoms and molecules," *Nature Physics*, vol. 17, p. 1324–1333, Nov. 2021.

[58] R. Jördens, N. Strohmaier, K. Günter, H. Moritz, and T. Esslinger, "A Mott insulator of fermionic atoms in an optical lattice," *Nature*, vol. 455, p. 204–207, Sept. 2008.

[59] C. A. Regal, M. Greiner, and D. S. Jin, "Observation of Resonance Condensation of Fermionic Atom Pairs," *Phys. Rev. Lett.*, vol. 92, p. 040403, Jan. 2004.

[60] M. W. Zwierlein, C. A. Stan, C. H. Schunck, S. M. F. Raupach, A. J. Kerman, and W. Ketterle, "Condensation of Pairs of Fermionic Atoms near a Feshbach Resonance," *Phys. Rev. Lett.*, vol. 92, p. 120403, Mar. 2004.

[61] O. Boada, A. Celi, J. I. Latorre, and M. Lewenstein, "Quantum Simulation of an Extra Dimension," *Phys. Rev. Lett.*, vol. 108, p. 133001, Mar. 2012.

[62] D. I. Tsomokos, S. Ashhab, and F. Nori, "Using superconducting qubit circuits to engineer exotic lattice systems," *Phys. Rev. A*, vol. 82, p. 052311, Nov. 2010.

[63] O. Boada, A. Celi, J. Rodríguez-Laguna, J. I. Latorre, and M. Lewenstein, "Quantum simulation of non-trivial topology," *New Journal of Physics*, vol. 17, p. 045007, Apr. 2015.

[64] A. Bolens and N. Nagaosa, "Topological states on the breathing kagome lattice," *Phys. Rev. B*, vol. 99, p. 165141, Apr. 2019.

[65] M. Aidelsburger, S. Nascimbene, and N. Goldman, "Artificial gauge fields in materials and engineered systems," *Comptes Rendus. Physique*, vol. 19, p. 394–432, Aug. 2018.

[66] V. Galitski, G. Juzeliūnas, and I. B. Spielman, "Artificial gauge fields with ultracold atoms," *Physics Today*, vol. 72, p. 38–44, Jan. 2019.

[67] T. Ando, Y. Matsumoto, and Y. Uemura, "Theory of Hall Effect in a Two-Dimensional Electron System," *Journal of the Physical Society of Japan*, vol. 39, p. 279–288, Aug. 1975.

[68] J.-i. Wakabayashi and S. Kawaji, "Hall Effect in Silicon MOS Inversion Layers under Strong Magnetic Fields," *Journal of the Physical Society of Japan*, vol. 44, p. 1839–1849, June 1978.

[69] D. J. Thouless, M. Kohmoto, M. P. Nightingale, and M. den Nijs, "Quantized Hall Conductance in a Two-Dimensional Periodic Potential," *Phys. Rev. Lett.*, vol. 49, pp. 405–408, Aug. 1982.

[70] T. Zhang, Y. Jiang, Z. Song, H. Huang, Y. He, Z. Fang, H. Weng, and C. Fang, "Catalogue of topological electronic materials," *Nature*, vol. 566, p. 475–479, Feb. 2019.

[71] N. Nagaosa, "A New State of Quantum Matter," *Science*, vol. 318, p. 758–759, Nov. 2007.

[72] M. G. Vergniory, L. Elcoro, C. Felser, N. Regnault, B. A. Bernevig, and Z. Wang, "A complete catalogue of high-quality topological materials," *Nature*, vol. 566, p. 480–485, Feb. 2019.

[73] J. E. Moore and L. Balents, "Topological invariants of time-reversal-invariant band structures," *Phys. Rev. B*, vol. 75, p. 121306, Mar. 2007.

[74] L. Fu, C. L. Kane, and E. J. Mele, "Topological Insulators in Three Dimensions," *Phys. Rev. Lett.*, vol. 98, p. 106803, Mar. 2007.

[75] B. K. Stuhl, H.-I. Lu, L. M. Aycock, D. Genkina, and I. B. Spielman, "Visualizing edge states with an atomic Bose gas in the quantum Hall regime," *Science*, vol. 349, p. 1514–1518, Sept. 2015.

[76] T. Chalopin, T. Satoor, A. Evrard, V. Makhalov, J. Dalibard, R. Lopes, and S. Nascimbene, "Probing chiral edge dynamics and bulk topology of a synthetic Hall system," *Nature Physics*, vol. 16, p. 1017–1021, June 2020.

[77] B. Sundar, M. Thibodeau, Z. Wang, B. Gadway, and K. R. A. Hazzard, "Strings of ultracold molecules in a synthetic dimension," *Phys. Rev. A*, vol. 99, p. 013624, Jan. 2019.

[78] C. Feng, H. Manetsch, V. G. Rousseau, K. R. A. Hazzard, and R. Scalettar, "Quantum membrane phases in synthetic lattices of cold molecules or Rydberg atoms," *Phys. Rev. A*, vol. 105, p. 063320, June 2022.

[79] E. J. Meier, F. A. An, and B. Gadway, "Observation of the topological soliton state in the Su–Schrieffer–Heeger model," *Nature Communications*, vol. 7, Dec. 2016.

[80] E. J. Meier, F. A. An, A. Dauphin, M. Maffei, P. Massignan, T. L. Hughes, and B. Gadway, "Observation of the topological Anderson insulator in disordered atomic wires," *Science*, vol. 362, p. 929–933, Nov. 2018.

[81] D. Xie, W. Gou, T. Xiao, B. Gadway, and B. Yan, "Topological characterizations of an extended Su–Schrieffer–Heeger model," *Npj Quantum Inf.*, vol. 5, May 2019.

[82] J. Alicea, Y. Oreg, G. Refael, F. von Oppen, and M. P. A. Fisher, "Non-Abelian statistics and topological quantum information processing in 1D wire networks," *Nature Physics*, vol. 7, p. 412–417, Feb. 2011.

[83] I. Timoshuk, K. Tikhonov, and Y. Makhlin, "Quantum computation at the edge of a disordered Kitaev honeycomb lattice," *Scientific Reports*, vol. 13, Sept. 2023.

[84] V. Lahtinen and J. Pachos, "A Short Introduction to Topological Quantum Computation," *SciPost Physics*, vol. 3, Sept. 2017.

[85] M. A. Bandres, S. Wittek, G. Harari, M. Parto, J. Ren, M. Segev, D. N. Christodoulides, and M. Khajavikhan, "Topological insulator laser: Experiments," *Science*, vol. 359, Mar. 2018.

[86] C. J. Flower, M. Jalali Mehrabad, L. Xu, G. Moille, D. G. Suarez-Forero, O. Örsel, G. Bahl, Y. Chembo, K. Srinivasan, S. Mittal, and M. Hafezi, "Observation of topological frequency combs," *Science*, vol. 384, p. 1356–1361, June 2024.

[87] S. Mittal, E. A. Goldschmidt, and M. Hafezi, "A topological source of quantum light," *Nature*, vol. 561, p. 502–506, Sept. 2018.

[88] T. Ozawa and H. M. Price, "Topological quantum matter in synthetic dimensions," *Nature Reviews Physics*, vol. 1, p. 349–357, Apr. 2019.

[89] M. Trautmann, I. Sodemann Villadiego, and J. Deiglmayr, "Realization of topological Thouless pumping in a synthetic Rydberg dimension," *Phys. Rev. A*, vol. 110, p. L040601, Oct. 2024.

[90] Y. Lu, C. Wang, S. K. Kanungo, F. B. Dunning, and T. C. Killian, "Probing the topological phase transition in the Su-Schrieffer-Heeger Hamiltonian using Rydberg-atom synthetic dimensions," *Phys. Rev. A*, vol. 110, p. 023318, Aug. 2024.

[91] T. Chen, C. Huang, B. Gadway, and J. P. Covey, "Quantum Walks and Correlated Dynamics in an Interacting Synthetic Rydberg Lattice," *Phys. Rev. Lett.*, vol. 133, p. 120604, Sept. 2024.

[92] T. Chen, C. Huang, I. Velkovsky, K. R. A. Hazzard, J. P. Covey, and B. Gadway, "Strongly interacting Rydberg atoms in synthetic dimensions with a magnetic flux," *Nat. Commun.*, vol. 15, p. 2675, Mar. 2024.

[93] S. Stellmer, M. K. Tey, B. Huang, R. Grimm, and F. Schreck, "Bose-Einstein Condensation of Strontium," *Phys. Rev. Lett.*, vol. 103, p. 200401, Nov. 2009.

[94] Y. N. M. de Escobar, P. G. Mickelson, M. Yan, B. J. DeSalvo, S. B. Nagel, and T. C. Killian, "Bose-Einstein Condensation of ^{84}Sr," *Phys. Rev. Lett.*, vol. 103, p. 200402, Nov. 2009.

[95] P. G. Mickelson, Y. N. Martinez de Escobar, M. Yan, B. J. DeSalvo, and T. C. Killian, "Bose-Einstein condensation of ^{88}Sr through sympathetic cooling with ^{87}Sr," *Phys. Rev. A*, vol. 81, p. 051601, May 2010.

[96] B. J. DeSalvo, M. Yan, P. G. Mickelson, Y. N. Martinez de Escobar, and T. C.

Killian, "Degenerate Fermi Gas of ^{87}Sr," *Phys. Rev. Lett.*, vol. 105, p. 030402, July 2010.

[97] M. K. Tey, S. Stellmer, R. Grimm, and F. Schreck, "Double-degenerate Bose-Fermi mixture of strontium," *Phys. Rev. A*, vol. 82, p. 011608, July 2010.

[98] S. B. Nagel, P. G. Mickelson, A. D. Saenz, Y. N. Martinez, Y. C. Chen, T. C. Killian, P. Pellegrini, and R. Côté, "Photoassociative Spectroscopy at Long Range in Ultracold Strontium," *Phys. Rev. Lett.*, vol. 94, p. 083004, Mar. 2005.

[99] P. G. Mickelson, Y. N. Martinez, A. D. Saenz, S. B. Nagel, Y. C. Chen, T. C. Killian, P. Pellegrini, and R. Côté, "Spectroscopic Determination of the s-Wave Scattering Lengths of ^{86}Sr and ^{88}Sr," *Phys. Rev. Lett.*, vol. 95, p. 223002, Nov. 2005.

[100] C. Wang, Y. Lu, S. K. Kanungo, F. B. Dunning, T. C. Killian, and S. Yoshida, "Elucidating the roles of collision energy and photon momentum transfer in the formation of ultralong-range Rydberg molecules," *Phys. Rev. A*, vol. 110, p. 032803, Sept. 2024.

[101] T. H. Loftus, T. Ido, M. M. Boyd, A. D. Ludlow, and J. Ye, "Narrow line cooling and momentum-space crystals," *Physical Review A*, vol. 70, Dec. 2004.

[102] S. K. Kanungo, J. D. Whalen, Y. Lu, T. C. Killian, F. B. Dunning, S. Yoshida, and J. Burgdörfer, "Loss rates for high-$n, 49 \lesssim n \lesssim 150, 5sns$ ($^3S_1$) Rydberg atoms excited in an ^{84}Sr Bose-Einstein condensate," *Phys. Rev. A*, vol. 102, p. 063317, Dec. 2020.

[103] W. Y. Kon, J. A. Aman, J. C. Hill, T. C. Killian, and K. R. A. Hazzard, "High-intensity two-frequency photoassociation spectroscopy of a weakly bound

molecular state: Theory and experiment," *Phys. Rev. A*, vol. 100, p. 013408, July 2019.

[104] Y. N. Martinez de Escobar, P. G. Mickelson, P. Pellegrini, S. B. Nagel, A. Traverso, M. Yan, R. Côté, and T. C. Killian, "Two-photon photoassociative spectroscopy of ultracold ^{88}Sr," *Phys. Rev. A*, vol. 78, p. 062708, Dec. 2008.

[105] B. J. DeSalvo, J. A. Aman, F. B. Dunning, T. C. Killian, H. R. Sadeghpour, S. Yoshida, and J. Burgdörfer, "Ultra-long-range Rydberg molecules in a divalent atomic system," *Phys. Rev. A*, vol. 92, p. 031403, Sept. 2015.

[106] R. Neuhaus, "Diode laser locking and linewidth narrowing," *Retrieved online from http://www. toptica. com*, 2009.

[107] R. Drever, J. Hall, F. Kowalski, J. Hough, G. Ford, A. Munley, and H. Ward, "Laser phase and frequency stabilization using an optical resonator," *Applied Physics B*, vol. 31, pp. 97–105, 1983.

[108] E. D. Black, "An introduction to Pound–Drever–Hall laser frequency stabilization," *American Journal of Physics*, vol. 69, p. 79–87, Jan. 2001.

[109] G. R. Fowles, *Introduction to modern optics*. Dover Books on Physics, Mineola, NY: Dover Publications, June 1989.

[110] R. A. Brienza, *Spectroscopic studies of the quantum defects for high-n singlet strontium Rydberg states*. PhD thesis, Rice University, Nov. 2023.

[111] C. L. Vaillant, M. P. A. Jones, and R. M. Potvliege, "Multichannel quantum defect theory of strontium bound Rydberg states," *J. Phys. B At. Mol. Opt.*

Phys., vol. 47, p. 155001, Aug. 2014.

[112] S. H. Autler and C. H. Townes, "Stark Effect in Rapidly Varying Fields," *Phys. Rev.*, vol. 100, pp. 703–722, Oct. 1955.

[113] N. F. Ramsey, "A Molecular Beam Resonance Method with Separated Oscillating Fields," *Phys. Rev.*, vol. 78, pp. 695–699, June 1950.

[114] W. P. Su, J. R. Schrieffer, and A. J. Heeger, "Solitons in Polyacetylene," *Phys. Rev. Lett.*, vol. 42, pp. 1698–1701, June 1979.

[115] S. Etemad and A. J. Heeger, "Polyacetylene, (CH)x: The Prototype Conducting Polymer," *Annual Review of Physical Chemistry*, vol. 33, p. 443–469, Oct. 1982.

[116] A. J. Heeger, S. Kivelson, J. R. Schrieffer, and W. P. Su, "Solitons in conducting polymers," *Reviews of Modern Physics*, vol. 60, p. 781–850, July 1988.

[117] C.-K. Chiu, J. C. Y. Teo, A. P. Schnyder, and S. Ryu, "Classification of topological quantum matter with symmetries," *Rev. Mod. Phys.*, vol. 88, p. 035005, Aug. 2016.

[118] N. Batra and G. Sheet, "Understanding Basic Concepts of Topological Insulators Through Su-Schrieffer-Heeger (SSH) Model," 2019.

[119] J. Brown and R. Churchill, *Complex Variables and Applications*. Boston, MA: McGraw-Hill Higher Education, 9th ed., 2009.

[120] M. V. Berry, "Quantal phase factors accompanying adiabatic changes," *Proceedings of the Royal Society of London. A. Mathematical and Physical Sciences*, vol. 392, p. 45–57, Mar. 1984.

[121] Y. Aharonov and D. Bohm, "Significance of Electromagnetic Potentials in the Quantum Theory," *Phys. Rev.*, vol. 115, pp. 485–491, Aug. 1959.

[122] J. Zak, "Berry's phase for energy bands in solids," *Phys. Rev. Lett.*, vol. 62, pp. 2747–2750, June 1989.

[123] M. Atala, M. Aidelsburger, J. T. Barreiro, D. Abanin, T. Kitagawa, E. Demler, and I. Bloch, "Direct measurement of the Zak phase in topological Bloch bands," *Nature Physics*, vol. 9, p. 795–800, Nov. 2013.

[124] F. Cardano, A. D'Errico, A. Dauphin, M. Maffei, B. Piccirillo, C. de Lisio, G. De Filippis, V. Cataudella, E. Santamato, L. Marrucci, M. Lewenstein, and P. Massignan, "Detection of Zak phases and topological invariants in a chiral quantum walk of twisted photons," *Nature Communications*, vol. 8, June 2017.

[125] M. Maffei, A. Dauphin, F. Cardano, M. Lewenstein, and P. Massignan, "Topological characterization of chiral models through their long time dynamics," *New Journal of Physics*, vol. 20, p. 013023, Jan. 2018.

[126] M. Atala, M. Aidelsburger, J. T. Barreiro, D. Abanin, T. Kitagawa, E. Demler, and I. Bloch, "Direct measurement of the Zak phase in topological Bloch bands," *Nature Physics*, vol. 9, p. 795–800, Nov. 2013.

[127] H. Kogelnik and T. Li, "Laser Beams and Resonators," *Applied Optics*, vol. 5, p. 1550, Oct. 1966.

[128] N. C. Wong and J. L. Hall, "Servo control of amplitude modulation in frequency-modulation spectroscopy: demonstration of shot-noise-limited detection," *J. Opt. Soc. Am. B*, vol. 2, pp. 1527–1533, Sept. 1985.